Primary Blast Injury of the Head: Numerical Prediction and Evaluation of Protection

By

Philip A. Lockhart

A thesis
presented to the University of Waterloo
in fulfillment of the
thesis requirement for the degree of

Master of Applied Science

in

Mechanical Engineering

Waterloo, Ontario, Canada, 2010

AUTHOR'S DECLARATION

I hereby declare that I am the sole author of this thesis. This is a true copy of the thesis, including any required final revisions, as accepted by my examiners.

I understand that my thesis may be made electronically available to the public.

ABSTRACT

The prevalence of injuries sustained from blast have been increasing over the past few decades due to the increasing use of Improvised Explosive Devices in areas where peacekeepers are deployed, as well as terrorist bombing incidents. The scope of this project was to evaluate the potential for head injury from primary effects in blast environments and to investigate protective aspects of protective equipment and new potential protective designs to mitigate or reduce the likelihood of Traumatic Brain Injury (TBI).

In order to meet these goals, methods of blast loading as well as the kinematic response of the head when subjected to blast loading were investigated numerically and validated against experimental data. This was done for both low and mid heights of burst at varying standoff distances. The methods of loading considered were the basic spherical air burst formulation of the CONventional WEaPons algorithm (CONWEP), an advanced version of the algorithm that included ground reflection and mach stem formation, and a hemispherical surface burst which included ground reflection. The method that produced the most consistent results compared to the experiments was the enhanced version of CONWEP for mid level heights of burst; however, for low heights of burst, a novel "mirrored charge" setup provided the most accurate predictions.

The kinematic response of the GEBOD numerical human body model, a rigid body representation of a 50^{th} percentile male, was validated against experimental tests conducted by Defense Research and Development Canada (DRDC) for a range of standoff distances and Heights of Burst. It was found the response of the GEBOD was in good agreement with the DRDC experiments for peak acceleration, impulse and the Head Injury Criterion.

The kinematic response of the head was investigated for various charge locations to study the effects of height of burst, lateral distance and standoff distance to the charge using the GEBOD numerical human body model. It was found that the standoff and height of burst had the largest influence on the acceleration experienced by the head. The height of burst study showed a large jump in the HIC_{15} injury criterion and head acceleration values when the charge was detonated within the region where a mach stem would form. As would be expected for the standoff distance from the charge, the closer the charge was to the body, the higher the accelerations experienced.

A quasi two dimensional model of the human head at the mid-sagittal plane was developed in order to evaluate response at the tissue level, and the effect of protection. The sagittal head model was used to examine wave interactions in the fluid flow around the head during a blast event. This was achieved by utilizing an Arbitrary Langrangian-Eulerian formulation to model the blast loading. This model was also validated against experimental data such that it demonstrated the same kinematic response as the experimental tests under identical blast loading conditions.

A helmet model was coupled to the sagittal head model using a layer of foam, and a statistical study was performed to determine the main effects and any interaction effects for the parameters of the numerical foam model. By analyzing these parameters and combining the best values for the effects, an optimum foam model was determined. This foam model was compared to actual foam materials and aluminum foam was found to have the closest properties to the idealized model. The aluminum

foam material model was placed into the existing sagittal model and was found to have decreased the acceleration seen by the head under all the different loading cases considered. The maximum principal strain in the brain and the maximum intracranial pressure were also examined and compared to proposed injury criterion. For implementation in a helmet, an additional layer of comfort foam or some other soft material would have to be added between the head and the aluminum foam to prevent it from cutting or injuring the person. Some of the polymeric foams investigated could be used instead of aluminum foam; however, more data is required to properly define the material response at high strain rate loading.

This study has shown that blast loading to the head can result in significant accelerations which could result in injury. By using common materials in the existing form of head protection, this potential for injury can be reduced.

TABLE OF CONTENTS

LIST OF FIGURES

LIST OF TABLES

ABBREVIATIONS

ACH	Advanced Combat Helmet
ALE	Arbitrary Langrangian Eulerian
ATD	Anthropomorphic Test Dummy
CAD	Computer Aided Drafting
CF	Canadian Forces
CFD	Computational Fluid Dynamics
CG	Center of Gravity
CONWEP	Conventional Weapons Algorithm
CSF	Cerebrospinal Fluid
DAI	Diffuse Axonal Injury
DRDC	Defense Research and Development Canada
FFT	Fast Fourier Transform
GCI	Grid Convergence Index
GEBOD	Generator of Body Data
HIC	Head Injury Criterion
HIII	Hybrid III
HIP	Head Impact Power
HOB	Height of Burst
IED	Improvised Explosive Device
PASGT	Personnel Armor System for Ground Troops
PBI	Primary Blast Injury
TBI	Traumatic Brain Injury
TNT	Trinitrotoluene

1 INTRODUCTION

The occurrence of blast injury has been widely recognized and documented for many years [1], particularly for traditional injuries to the air containing organs and fragmentation injuries. As early as World War I, it was noted that close proximity to explosions could result in injuries to the brain even if no external injuries were noted. This phenomenon became known as "shell shock" and is now referred to as Traumatic Brain Injury (TBI) amongst the modern medical community. The symptoms of TBI include retrograde and anterograde amnesia, severe headache, tinnitus, hypersensitivity to noise, tremors, dizziness and difficulty with decision making [2][3]. In some cases it has been found that the ventricles within the brain have become enlarged and there is minor bleeding [3].

For the United States Armed Forces, from October 2001 to August 2007, Improvised Explosive Devices (IEDs) were responsible for many of the 3000 combat deaths in Iraq and 240 combat deaths in Afghanistan [4]. It was found that 88% of soldiers treated at an Echelon II military medical unit in Iraq had been injured by IEDs or mortars [3]. For the Canadian Forces, 97 of the 142 casualties in Operation Enduring Freedom (OEF) have been a result of IEDs and suicide bombs over the course of the conflict [5]. While penetration and/or fragmentation injuries still remain responsible for the greatest number of battlefield deaths, the more prominent use of IEDs in the various conflict regions around the globe (including Operation Iraqi Freedom and Operation Enduring Freedom) and improvements in body armour design have shown a shift in the injury patterns to an increase in primary blast neurotrauma [6].

Blast injury is also becoming more common amongst the civilian population as incidences of terrorist bombings have increased over the past 4 decades. In Israel alone, 71 suicide bombings were carried out between November 2000 and May 2003 [7]. Analysis performed on 14 published terrorist bombing incidents from 1969 to 1983 showed that the highest mortality rates occurred in those who suffered an injury to the head [8]. The other prominent injury to unarmoured civilians is blast lung injury which can result in even higher mortality rates if the explosive detonation and victim are located within an enclosed space (such as a bus or building) [7].

The mechanisms of primary blast injury are not well known and this is compounded for Primary TBI as it is difficult to separate the psychological from the physiological effects. It has become widely accepted in the last decade that exposure to blast waves can cause subtle injury to the brain which later manifests itself as TBI. However, there currently exists no criteria by which the extent of these injuries can be predicted, mostly because head response and the potential injury resulting from blast loading is difficult to evaluate due to very high accelerations of the head over a very short time period, as well as the complex nature of blast loading and interaction with the human body.

This lack of understanding for what causes TBI makes it difficult to design protection to prevent its occurrence. The design of new equipment relies heavily on experimental validation; however, the current mechanical surrogates used for validation were designed for automobile safety and may have little relevance to a blast-injury scenario depending on the injury mechanism. This also applies to the Head Injury Criteria (HIC) which is commonly used to predict head injury in blast

but was created and validated for car crash scenarios [9]. In order to design effective protection, a biofedelic surrogate and valid injury criteria for blast must be developed to relate measurable mechanical response to injury.

It was recognized in 2001 that a large number of weapon systems used during the 1990s appeared to utilize blast as their main damage mechanism. These devices (Thermobaric, Fuel-Air, Metallized, and Reactive Surround) alter the typical blast wave profile shape to impart more energy to the target by adding more impulse and duration for an equivalent peak pressure. The increase in the use of these weapon systems will increase the likelihood of their use by terrorists and it has been predicted that coalition forces will have to face more of these types of weapons in future conflicts [10].

The scope of this project was to investigate protective aspects of current armour and investigate new potential protective designs to mitigate or reduce the likelihood of TBI. In order to meet these goals, the numerical implementation and methods of blast loading as well as the kinematic response of the head when subjected to blast loading were validated against experimental data. Subsequently, a numerical model of the human head was developed that had the same kinematic response as the actual head to be used as a base for the protective equipment to be studied.

2 PHYSICS OF BLAST LOADING ON STRUCTURES AND BLAST MODELLING

For this study, characterization of the blast wave and pressure field was investigated as opposed to the source of the blast wave. It should be noted that different explosives will produce different pressure profiles for the same TNT weight equivalent making the number of possible loading scenarios significant. However, the effect in terms of interaction with the blast wave will be similar and was investigated in this study.

2.1 FUNDAMENTAL BLAST PHYSICS

Chemical explosives involve the rapid oxidation of fuel in the explosive compound. When the explosive is reacted, it decomposes producing heat and gas. Unlike low explosives, such as gunpowder, which react relatively slowly, high explosives such as TNT or C4 detonate very quickly and form high-pressure gases that rapidly expand compressing the surrounding medium. High explosives are defined as those that can readily detonate without being confined, leading to a supersonic pressure shock wave [11]. This shock wave, or discontinuity in pressure, interacts with surrounding structures, including the human body, and is what leads to primary blast injuries.

There is another class of explosives in addition to the standard high- and low-explosives that are characterized by a very different pressure profile. Volumetric-type blasts refer to thermobaric munitions, fuel-air explosives or enhanced blast munitions designed to cause damage by means of blast overpressure, rather than fragmentation. These munitions have been designed to modify

the pressure that is produced to impart the most impulse or very sharp accelerations to the target [10]. Although not considered in this study, the modeling techniques developed could be applied to these scenarios.

Considering high explosives, when detonation is initiated, the explosive undergoes a chemical reaction and is converted from a solid explosive to a high pressure, high temperature gas. As the blast wave and the corresponding gases move outwards from the detonation point, the gases expand and the pressure falls to atmospheric. However, since the gases have mass, the momentum of the wave front takes longer to attenuate. This extra time spent travelling over-expands the gases and causes the pressure behind the blast wave to become less than atmospheric causing the flow to reverse and flow towards the source. This under-pressure is also known as the negative phase and will eventually return to equilibrium at atmospheric pressure [11]. The ideal form of the pressure distribution over time for a blast wave can be shown by the Friedlander Curve (Figure 1). This curve is based on Friedlander's work for the UK Home Office during the Second World War and can be described with the following function (Equation 2.1) for the positive and negative pressure phases.

$$p = p_0 \left(1 - {}^{t}/_{t_0}\right) e^{-kt/t_0} \qquad \textbf{(Equation 2.1)}$$

In the above equation p is the pressure at any time t, and the value for k is selected based on experimental data and is known as the waveform parameter; p_0 is the ambient pressure and t_0 is the time at which the positive duration begins. The waveform parameter determines the decay characteristics of the blast wave; curves with very quick decay rates are typical of nuclear

explosions and have a high k value while slower rates are attributed to explosions with large volumes of product gases [12].

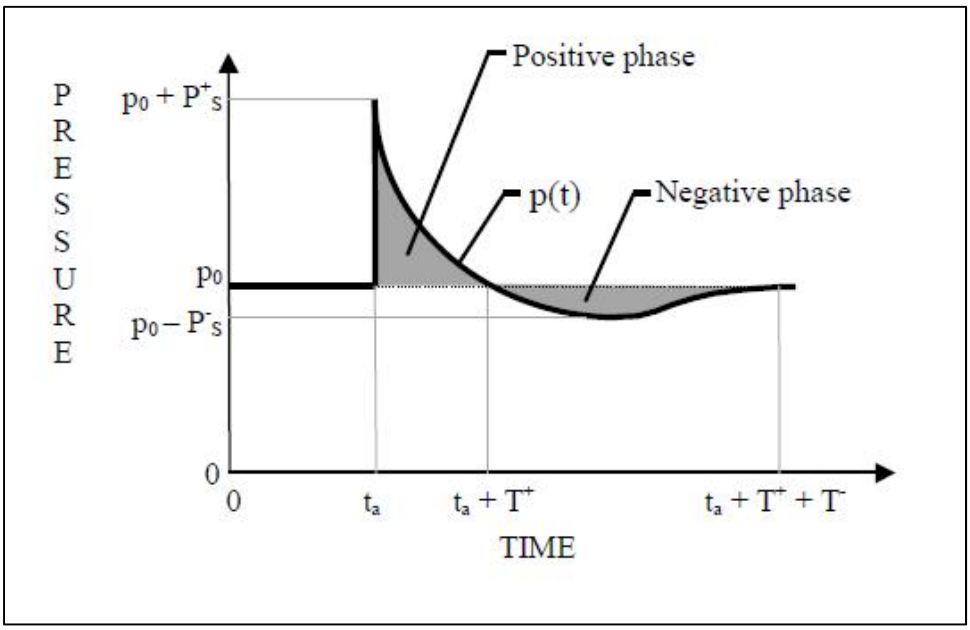

Figure 1: Friedlander Curve [13]

The blast overpressure can be defined as the sharp instantaneous rise in ambient atmospheric pressure resulting from explosive detonation. This overpressure generally takes the form of the positive phase of the Friedlander Curve and its interaction with a structure is generally expressed in terms of the peak acceleration seen by the structure. For conventional explosives, the typical blast overpressure duration is quite short, 5-100 ms, while the positive duration for a nuclear blast is much longer, 3-10 seconds [12]. Blast waves created by nuclear detonations require different equations and have slightly different behavior than blast waves from smaller conventional explosives and are generally not considered when dealing with blast protection for individuals due to the complex nature of the waveform [12].

In an enclosure, the blast wave can interact with walls and other structures creating a complex waveform. The waves reflect off of walls and other structures and can add or superimpose on to one another, increasing the amplitude of the overpressure via wave superposition. These complex blast waves show the major overpressure peak but are also followed by one or several smaller overpressure peaks (Figure 2) that can add to the total overpressure force. Because of this, complex blast waves are usually expressed by their impulse (area under the acceleration-time curve) instead of their maximum peak overpressure value [14]. Complex blast waves can be generated by explosions inside enclosures or by the jets from shaped-charge warheads penetrating into armoured vehicles or naval vessels [15] and have the potential to cause much higher injury than free-air detonations that resemble Friedlander waves.

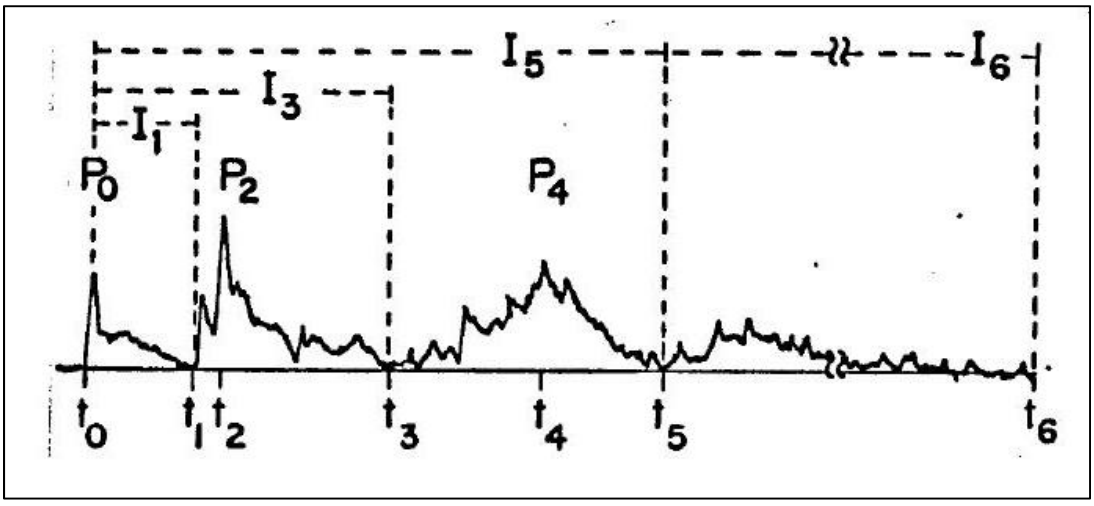

Figure 2: Complex blast wave from inside an armoured vehicle [15]

The ignition and growth of the detonation products can be simulated by using the JWL equation of state [16] (Equation 2.2) which relates energy, pressure and density,

$$p = A\left(1 - \frac{\omega}{R_1 V}\right)e^{(-R_1 V)} + B\left(1 - \frac{\omega}{R_2 V}\right)e^{(-R_2 V)} + \frac{\omega}{V}E \qquad \textbf{(Equation 2.2)}$$

Pressure can also be related to temperature and density/specific volume by using the Rankine-Hugoniot relations for air (Equation 2.3) (Equation 2.4) [17].

$$specific\ volume = \frac{v}{v_0} = \frac{7 + \frac{\Delta P}{P_0}}{7 + 6\frac{\Delta P}{P_0}} \qquad \textbf{(Equation 2.3)}$$

$$temperature = T = T_0\left(\frac{7 + \frac{\Delta P}{P_0}}{7 + 6\frac{\Delta P}{P_0}}\right)\left(1 + \frac{\Delta P}{P_0}\right) \qquad \textbf{(Equation 2.4)}$$

Where ΔP is the incident overpressure, P_0 is the atmospheric pressure, T_0 is the initial temperature and v_0 is the initial volume.

2.2 BLAST INTERACTION WITH STRUCTURES AND RESPONSE

Blast load interaction with structures is complex due to the high pressures and short durations of the blast wave, combined with the shape dependent flow of the loaded object. Some of the important characteristics of the blast wave are the arrival time, the positive phase duration and the peak reflected pressure [12].

The static or "side-on" pressure can be thought of as the pressure that a particle travelling within the flow would sense and is widely used as a reference in experimental testing and injury criteria. This is typically measured using a pressure transducer device with a knife edge aligned parallel

to the direction of the blast flow known as a lollipop gauge (Figure 3). Dynamic pressure, or blast wind, is caused by the movement of air displaced by the explosive products. Total pressure is the summation of the static and dynamic pressures, and can be measured by placing a specially designed sensor, such as a pitot tube, perpendicular to the blast flow. When a fluid flow is forced to stop at a stagnation point (the gauge or a bluff body), the kinetic energy converts to pressure resulting in the total pressure. This resultant build up of pressure in front of a wall or the body can significantly affect trauma outcome, and is dependent on the properties and shape of the surface.

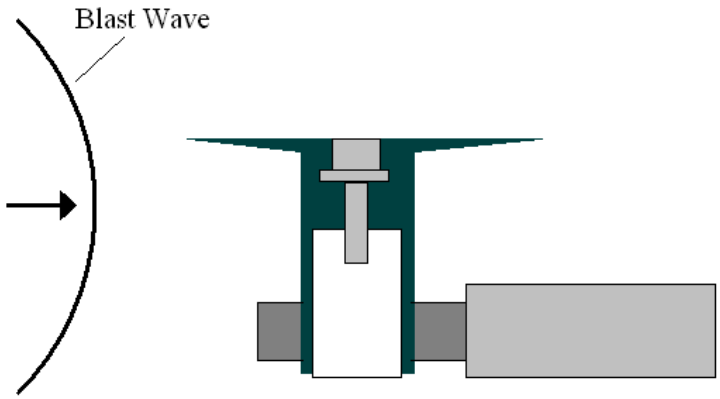

Figure 3: Lollipop Gauge

While the pitot tube and lollipop gauge sensors work well with stable, lower speed flows, there are some issues with measuring rapidly changing pressure waves and pressure waves that exceed the local speed of sound. One issue that can complicate pressure measurements is the invasive nature of the device in the flow field. If the flow around the sensor exceeds the speed of sound, a shock wave can form around the sensor making it difficult to interpret exactly what the sensor is measuring.

Reflected pressure is defined as the maximum pressure measured at a wall, or rigid interface placed normal to the blast flow [12]. Dynamic and reflected pressure both build quickly as the higher pressure blast wave displaces great amounts of air. The shock velocity increases with increasing pressure, allowing for a large pressure differential to drive a shock wave exceeding the sound speed at ambient pressure. The peak overpressure at the flat surface, p_r, is related to the peak incident overpressure, p_0, by (Equation 2.5).

$$p_r/p_0 = 2(7p_a + 4p_0)/(7p_a + p_0) \quad \textbf{(Equation 2.5)}$$

When the blast wave strikes a surface, the pressure level at that surface will rise suddenly then fall. The transient stress is transmitted through the material as a compressive stress wave, which will reflect once it hits the rear face of the material. The reflected wave will be in tension and will add itself to the trailing edge of the incoming compressive wave. This results in the material experiencing a stress that is equal to the sum of both waves at this point at that instant in time [11].

The compressive stress wave may change shape and characteristics as it travels across the material depending on the stress at the impact site and the material properties. If the stress at the impact site is greater than the yield strength of the material, an elastic stress wave as well as a plastic stress wave will be generated. Plastic waves move much slower than elastic waves and will eventually disperse into an elastic wave as energy is lost due to plastic deformation of the material. This dispersion happens over a relatively short distance [18], thus making plastic waves difficult to observe.

If the compressive wave strikes an interface between two dissimilar materials, such as in a layered composite, or at a change in cross-sectional area, part of the wave will be transmitted through the second material, while the remaining part of the wave will be reflected in the original material. For materials with equal cross-sectional areas but different material properties, the fraction of the wave that is transmitted is solely a function of the sonic impedance, ρC, for the two layers (Equation 2.6) (Equation 2.7) [18]; where σ_I, σ_R, and σ_T are the amplitudes of the incident, reflected and transmitted waves respectively, A is the cross-sectional area, and the wave is assumed to be moving from material 1 to material 2. This wave transmission characteristic has a very large importance in blast loading of humans due to the large number of different tissue interfaces within the human body.

$$\frac{\sigma_T}{\sigma_I} = \frac{2A_2\rho_2C_2}{A_2\rho_2C_2 + A_1\rho_1C_1} \quad \textbf{(Equation 2.6)}$$

$$\frac{\sigma_R}{\sigma_I} = \frac{A_2\rho_2C_2 - A_1\rho_1C_1}{A_2\rho_2C_2 + A_1\rho_1C_1} \quad \textbf{(Equation 2.7)}$$

When ρ_2C_2 is greater than ρ_1C_1, a pulse of the same sign as the incident wave is reflected, when ρ_2C_2 is less than ρ_1C_1, a pulse of opposite sign is reflected [18].

Aside from the stress waves generated within the body loaded by the blast wave, the body itself will also be accelerated by the pressure force applied. This acceleration can cause displacement and rotation of the body depending on the location of the charge and the angle of incidence of the blast wave on the body. The sudden acceleration of the body as well as any resulting impact with surrounding objects or structures are considered the primary factors in causing injury.

The pressure wave will be altered by contact with the structure should the wavefront be wider or taller than the contacted structure. If the structure is fully immersed in the blast wave flow field then the wave will "wrap" itself around the structure. This allows the blast wave to load all parts of the structure including loading the rear of the structure long after the initial loading, unlike a direct impact scenario which would just load the structure at the point of contact. When the waves that are enveloping the structure meet at the opposite point from the initial contact there is a pressure enhancement as the flow is effectively stagnated [19] which can result in higher loading on the rear of the structure than on the front. This is of high importance for blast loading to the head since it is generally completely immersed in the blast flow field.

2.3 GROUND REFLECTION

For explosions with low heights of burst (HOB), the blast waves are reflected by the ground. In the case of oblique reflection, the incident shock wave impinges upon a surface with a small angle of incidence and a shock wave is reflected back into the flow. Unlike a sound wave the angle of reflection does not equal the angle of incidence. A shock front impinging on a surface near grazing incidence does not reflect directly, instead it exhibits mach reflection and is deflected so that it propagates along the surface. When the reflected wave overtakes the incident wave it creates what is known as a "triple point" and the fronts merge into a single outward travelling front called the Mach stem (Figure 4). The Mach stem is usually assumed to be a straight vertical line and is initiated when the pressure wave angle of incidence exceeds 40° for air [11]. Other fluids will have different angles of incidence for initiating the Mach stem.

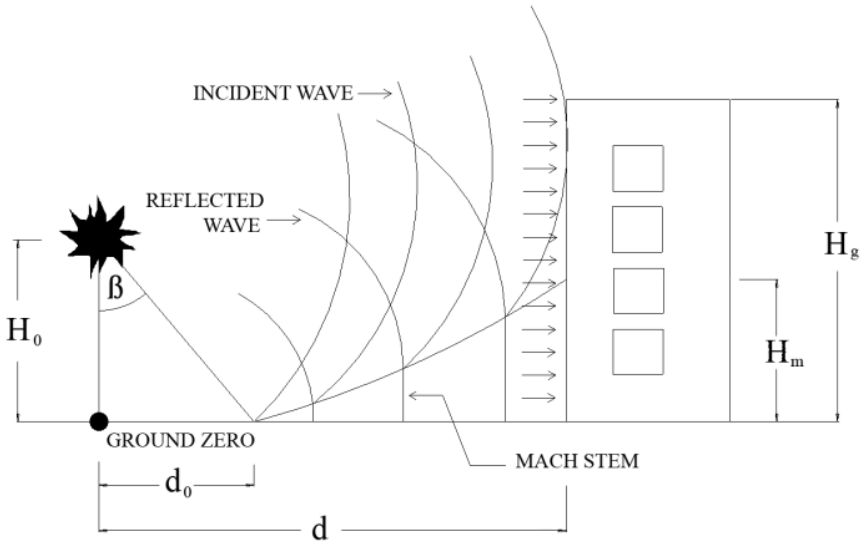

Figure 4: Mach stem formation: reproduced from [20]

Mach reflection is important for blast loading in scenarios where the height of burst for detonations is generally within the range for mach stem formation. Mach stems also occur when a device is detonated inside a structure where the angles of incidence can vary over a wide range [11]. The blast overpressure decreases with distance from the explosive with an inverse cubic relationship. In an ideal air burst, this indicates that the level of injury sustained will be greatly decreased by slightly increasing the distance from the charge. However, the mach stem formation will increase the over pressure at larger standoff distances [11] making it more likely that a higher level of injury would be sustained in the medium and far field than predicted by the ideal equations. The scaled height of the mach stem, H_m, can be estimated using the scaled height of burst, H_b, the ground zero distance, d, and the limiting distance, d_0 (Equation 2.8).

$$H_m = 0.07 H_b \left[\left(\frac{d}{d_0}\right) - 1\right]^2 \qquad \textbf{(Equation 2.8)}$$

This equation has been found to give a good estimate of the mach stem height for values of d greater than 1 meter [20].

2.4 SIMPLIFIED BLAST LOADING ON STRUCTURES

The finite element code LS-Dyna has a built in routine to apply blast loading to structures using the *LOAD_BLAST keyword. The blast loading is applied to the structure as a pressure distribution [16] based on the CONWEP equations developed from empirical data by Kingery and Bulmarsh [21]. The CONWEP blast load requires the input of the charge weight and the location of the charge center in terms of x, y, and z coordinates, and applies the positive phase reflected pressure load to a defined segment surface based on the distance to the charge and charge size [16]. Two types of blast loads are available in LS-Dyna release 971, surface and air burst. The air burst calculates a spherical blast wave in the form of an ideal Friedlander curve and does not consider ground interaction and reflection. The surface burst assumes the charge is located directly on the surface and creates a hemispherical wave that does include ground reflections [16]. The *LOAD_BLAST keyword allows for numerical modeling of blast loading without the use of separate Computational Fluid Dynamics (CFD) programs or Arbitrary Lagrangian Eulerian (ALE) formulation (see section 2.5), common methods of numerically simulating a blast pressure wave [22].

A recent development in LS-Dyna has been the implementation of an enhanced blast loading formulation which incorporates the formation of the mach stem and reflected wave interaction when computing the loading. However, this enhanced blast function is only valid for a certain

burst height range (0.136 ft/lbm$^{1/3}$ to 100 ft/lbm$^{1/3}$) based on the scaled HOB [23]. In addition, both the original and enhanced blast formulations of CONWEP cannot predict structural interaction in the near field, defined as inside the fireball radius for the explosion. For charges outside of this range, such as those with low heights of burst, the surface burst function can be considered; however, the surface burst places the charge directly on the ground which will affect the reflected wave response.

2.5 ALE FORMULATION

Modeling detonation and expansion of an explosive is complicated but can be numerically modeled in a simplified manner by treating the explosion as an expansion of high pressure gas that generates a shockwave in the surrounding medium. The shockwave is treated as a discontinuity in which the pressure, temperature and density jump to a higher value over a very short time frame. This has implications in numerical models since the mesh size must be fine enough to reasonably approximate the shock front which is normally "smeared" over a small number of elements [24]. Explosions are often modeled using Eulerian formulations to account for the large deformations in the air surrounding the explosive. The LS-Dyna finite element code [25] has been widely used to model explosive detonation, expansion and interaction with structures including the human body [24] through use of the ALE formulation.

The ALE formulation is an algorithm that performs rezoning of the mesh when it becomes too distorted. A Lagrangian time step is followed by an advection (remapping) step. The advection step moves the nodes by a small fraction of the characteristic lengths of the surrounding elements to remove the mesh distortion [25] (Figure 5). It is important to note that the advection step does

not move the material, it merely redraws the mesh. The Langrangian step can be considered to be a control mass problem in which the element distorts over time but the mass and density remain constant.

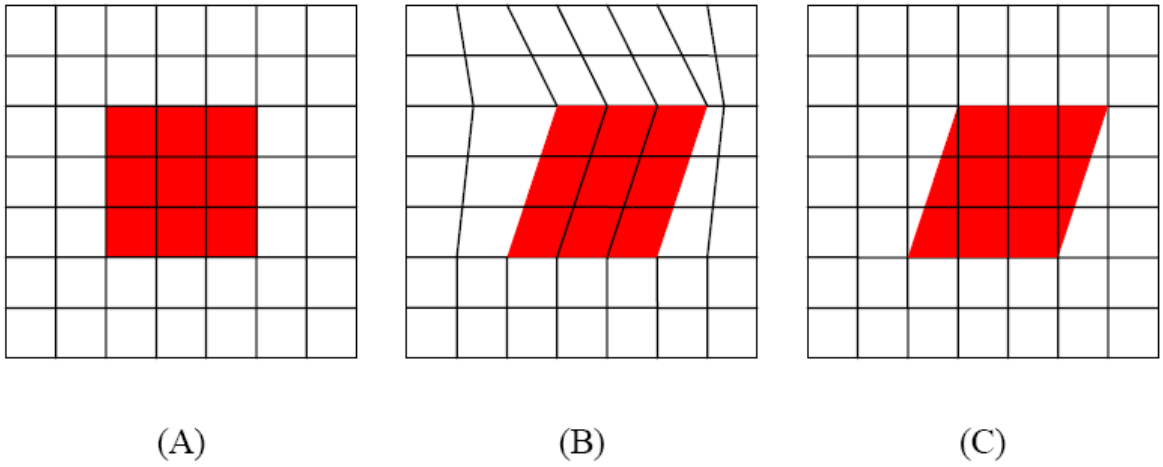

Figure 5: ALE Steps - (A) Original, (B) After Lagrangian Step, and (C) Advection [26]

The problem with Langrangian formulations in terms of blast loading is their inability to handle large deformations which will cause instability. To account for this, an Eulerian formulation is used which considers the problem in terms of a constant volume. Material is allowed to flow through the mesh and thus free surfaces can be created and multiple materials can exist in the same element. To avoid numerical errors, the ALE element size should be very close to, or smaller than, that of the embedded Lagrangian object to allow for proper interaction between the ALE and the object.

All non-enhanced blast loading numerical simulations were performed using the d971_1224 version of the LS-Dyna solver since the ALE formulation requires this version to correctly create

the shock front with the ambient element formulation. All simulations utilizing enhanced blast loading used the d971_R4_2_1 version of the LS-Dyna solver.

Mesh refinement directly influences the accuracy and reliability of a simulation as well as the accuracy of the overall model behavior [27]. To determine if the mesh results had converged to within an acceptable limit, a Richardson extrapolation was used to calculate the Grid Convergence Index (GCI) which has been proposed as a standard to quantify the level of convergence in a numerical model. The GCI relates the error of the response of a mesh to the error that would be expected from a grid convergence study of the same problem using a grid doubling with a second-order method to produce an error "band" [28].

In order to perform Richardson extrapolation, the order of the convergence, p, must be known.

$$p = \ln\left(\frac{f_3 - f_2}{f_2 - f_1}\right) / \ln\,(r) \qquad \textbf{(Equation 2.9)}$$

Where f_3, f_2, and f_1 are the results for the coarse, medium and fine meshes respectively and r is the grid refinement ratio which relates two mesh sizes ($r=h_2/h_1$). Once r and p are known, the GCI between the fine and medium meshes (GCI_{12}) and the medium and coarse meshes (GCI_{23}) can be calculated.

$$GCI_{12} = F_s\left(\frac{f_2 - f_1}{f_1}\right) / (r^p - 1) \qquad \textbf{(Equation 2.10)}$$

$$GCI_{23} = F_s\left(\frac{f_3 - f_2}{f_2}\right) / (r^p - 1) \qquad \textbf{(Equation 2.11)}$$

In the above equations, F_S is the "safety factor" for the Richardson Error Estimator. For convergence studies using a minimum of three meshes, this value is 1.25; however, for two-mesh convergence studies this value should be 3 [28]. This value can also be thought of as representing a 95% confidence bound on the estimated relative error.

Richardson extrapolation, and hence the GCI, are based on the assumption that the Taylor series expansion is valid asymptotically and that that two meshes being considered are within the asymptotic range. This range can be considered to be achieved when the following equation is fulfilled [28].

$$GCI_{23} \approx r^p GCI_{12} \quad \textbf{(Equation 2.12)}$$

2.6 HUMAN SURROGATES FOR BLAST LOADING

Due to the potential for injury associated with blast injury, the use of live human subjects in testing is not possible. In situations where human body response during extreme impact loading is required, Anthropomorphic Test Dummies (ATDs) are often used as biofidelic surrogates. These mechanical dummies mimic relevant human characteristics such as mass, size and energy absorption and dissipation and can measure accelerations, displacements, forces and loads which can then be used with the relevant injury criteria [29]. ATDs are classified according to their size, age, sex and loading. The Hybrid III (HIII) dummy family consists of a 5th percentile female, a 50th percentile male, and a 95th percentile male (Figure 6) as well as a 3-year-old and 6-year-old child dummy. It is important to note that a dummy is only valid for the loading type for

which it was designed. A frontal crash dummy response is not biofidelic when used in a side or rear collision. This has large implications for measuring blast loading response since no dummy currently exists which can accurately mimic the human response to primary blast loading, although some are currently under development such as the Mannequin for the Assessment of Blast Incapacitation and Lethality (MABIL) dummy being developed by Defense Research and Development Canada (DRDC) [30].

The most common ATD for automotive testing is the HIII which has been used in many studies of blast loading response [6][31]. These dummies can be used in frontal collision evaluations since their necks mimic the human bending response in flexion and extension. The head of the HIII is composed of an aluminum shell covered by a vinyl skin of constant thickness. The neck is made of axisymmetric rubber segments bonded to aluminum disks with a braided wire cable passing through the centre. To simulate the atalanto-occipital joint of the human, the top end plate of the neck is attached to the head with a single pivot joint.

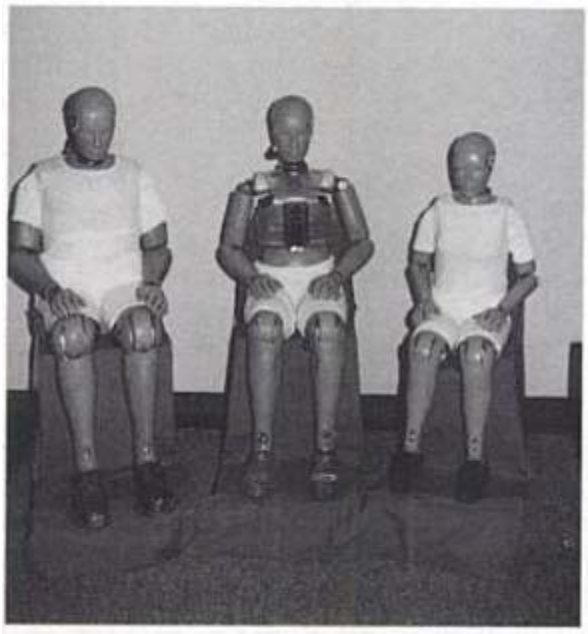

Figure 6: Hybrid III Adult Dummies [29]

Two models of ATDs are available in LS-Dyna; the GEBOD (GEnerator of BOdy Data) and the HIII. The GEBOD uses regression equations from anthropometric surveys to generate data sets of mass and geometric properties for the various body segments [32]. This virtual dummy consists of 17 rigid bodies in the form of ellipsoids connected by fully articulated joints that have properties and locations based on the same anthropometric data sets used for the rigid bodies. The locations of the joints as well as the segment properties are based on the weight and height for the selected percentile dummy. The height and mass values are in the internal LS-Dyna database which is based on the GEBOD Database. The GEBOD motion within the LS-Dyna simulation is controlled by equations integrated into LS-Dyna that are separate from the finite element model [16].

There are three sizes of HIII available in LS-Dyna; 5^{th}, 50^{th}, and 95^{th} percentile adults. As with the GEBOD, the motion of the dummy is governed by equations separate from the model. Unlike

the GEBOD, the HIII model can have deformable components which are assigned constitutive material models by the finite element code. The abdomen and jacket are assigned a low density foam constitutive model while the headskin is given a simple viscoelastic constitutive model [16].

2.7 EXPERIMENTAL BLAST TEST DATA

Experiments were conducted by DRDC Valcartier (Table 1) [33] using a HIII dummy with 5kg cylindrical charges (aspect ratio of 1/1) of C4 at various standoff distances and heights of burst. This data set was used to validate the response of the developed models.

Table 1: Test matrix for DRDC experiments

Test No.	Charge	Charge Height	HEAD 1 and HEAD 2 (R1)	Burn Gauge (R2)	TORSO1 / TORSO 2 / BTD (R3)	UofWaterloo Rig 1 and Rig 2 (R4)	Hybrid III (R5)
1-6	5kg C4	1.5 m	5 m	7.5 m	4 m	5	4 m
7-11	5kg C4	0.2 m	5 m	7.5 m	4 m	5	4 m
12-17	5kg C4	1.5 m	5 m	5 m	3.5 m	4	3.5 m
18-22	5kg C4	0.2 m	5 m	5 m	3.5 m	4	3.5 m
23-28	5kg C4	1.5 m	5 m	4 m	3 m	3	3 m

The HIII used in the experiments was aligned such that the chest faced the blast and was supported by a frame with an electromagnetic release that activated just prior to detonation so that the dummy was unsupported when struck by the blast wave. This was done to eliminate possible bias in the acceleration data caused by the weight of the mannequin on the support frame.

The HIII dummy used for the experiments was modified with extra sensors to measure linear and rotational accelerations of the head, as well as chest deflection and neck loads. In addition, lollipop pressure gauges were placed at one meter intervals outwards from the point of detonation starting at two meters from the charge centre. A Pitot tube was also placed at the same distance as the target as well as on the ground for reference [33] (Figure 7). These pressure transducers provided the dynamic and static pressure histories for each test.

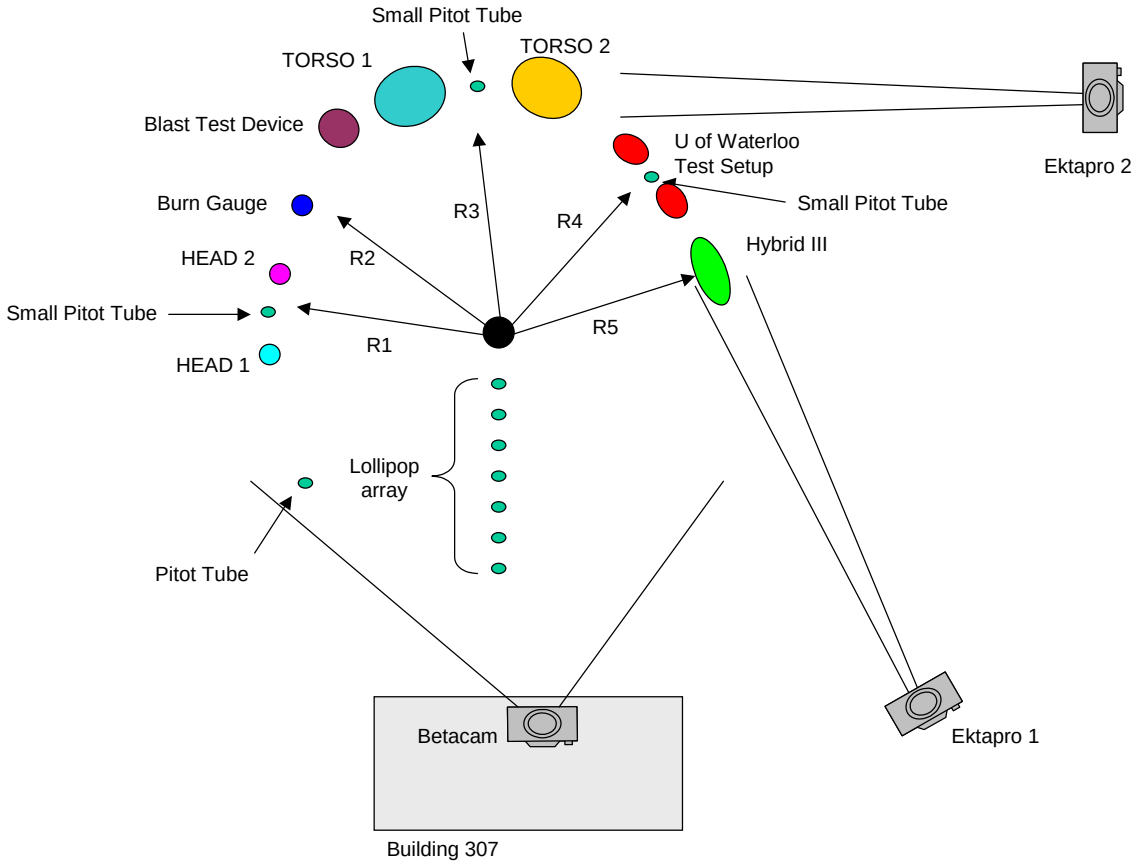

Figure 7: Experimental Test Setup [33]

To prevent debris from interfering with the high-speed imagery equipment, the charges were suspended over the test site with a gantry; previous studies used Sonotubes to support the charge.

The charges were contained within a nylon bag that was attached to the gantry with a wire. Ionization pins were placed in contact with the detonator for each charge to provide reference times for the detonations.

The recorded data were saved in ASCII format with one file per channel of data. All data were taken at a sampling rate of 500 K/sec with an anti-aliasing filter applied with a frequency of 40 kHz.

3 ANATOMY OF THE HUMAN HEAD

The human head consists of several parts, including the skull, face, scalp, teeth, brain, cranial nerves, meninges, special sense organs, and other structures such as blood vessels, lymphatics and fat [34]. The interactions between the brain and skull as well as the interior components of the brain are of particular importance when discussing brain injury for non-penetrating wounds such as those in a blast scenario.

3.1 ANATOMICAL TERMINOLOGY

Anatomical directions are used to describe the relative positions of various structures of the human body with respect to the anatomic position (Figure 8). In the anatomic position, the person is standing upright with feet parallel and flat on the floor; the head is level and the eyes look forward. The arms are at either side of the body with the palms facing forward and the thumbs pointing away from the body.

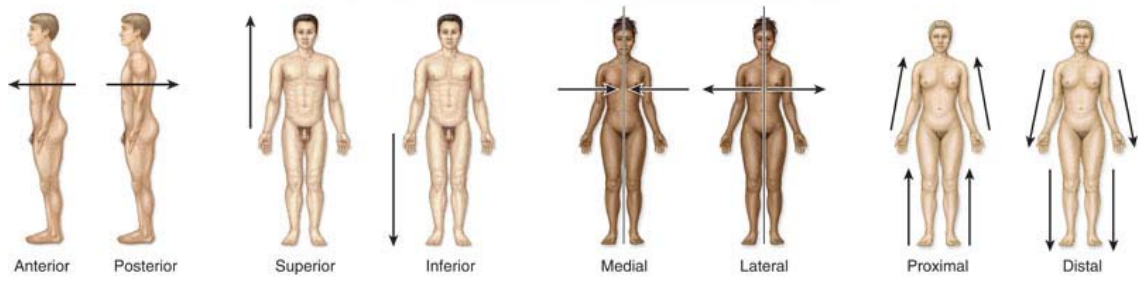

Figure 8: Anatomical Directions [35]

The directions are given with respect to the anatomical planes of the body (Figure 9). These 3 planes all cross at the central longitudinal axis of the body.

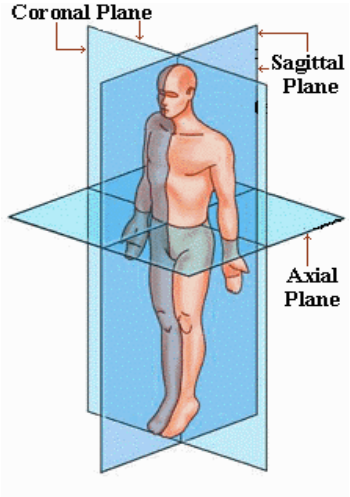

Figure 9: Anatomical Planes [36]

3.2 THE SKULL

The skull is the main protective barrier for the brain. It is composed of both cranial and facial bones, with the cranial bones forming the protective shell around the brain (Figure 10). The eight bones that make up the cranium also provide attachment sites for jaw, head and neck muscles. The cranial cavity, the largest cavity in the skull, has an adult volume of approximately 1300 to 1500 cubic centimeters. The cranial bones are held together by immovable joints called sutures which disappear over time as the adjacent bones fuse together [35]. The size of the skull, specifically the cranial cavity, determines the size of the brain [35].

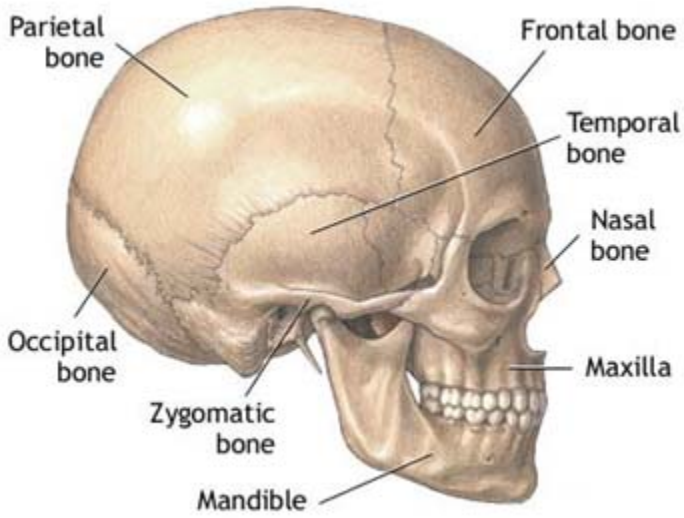

Figure 10: Skull Anatomy [37]

The walls of the cranial cavity vary in thickness with walls in females being usually thinner than those in males. The bone tends to be thinnest in areas that are well covered in muscles, such as the flat (squamous) part of the temporal bone and the area of the base of the skull posterior to the foramen magnum [34] (the opening in the base of the skull for the brainstem). The skull is comprised of an inner and outer cortical bone layer with a thin cancellous bone (diploë) layer sandwiched between them. The cortical bone is compact and extremely dense while the cancellous bone is very porous. Cortical bone can withstand greater stress, has a high stiffness, and fractures and very low strains. In contrast, cancellous bone can withstand greater strain, has a low stiffness and fractures at very high strains. The thickness of the spongy core increases toward the center of the bone away from the cranial sutures [38].

Bone is comprised of 60-70% minerals and collagen and exhibits a viscoelastic response to loading. This type of response results in variable stress-strain properties that are dependent on the strain rate. The mechanical properties of the cranial bones have been found through

experimental tests on human cadavers (Table 2) [39]. It is important to note the anisotropic behavior of the cortical bone material. For the purposes of the experimental study orientation angles were taken with respect to the sagittal suture with 0° corresponding to a vector tangential to the suture and 90° corresponding to a vector normal to the suture. The first two values are for specimens taken from the frontal bone while the last two values are for specimens taken from the parietal bone.

Table 2: Mechanical Properties of Cranial Bone

Orientation	E diploë [MPa]	K [MPa]	G [MPa]	E [MPa]	σ_y [MPa]
0°	65	16900	11660	28300	98.0
45°	130	11700	8073	19656	80.0
90°	65	14460	9954	24000	92.0
45°	130	5080	3450	9740	58.4

3.3 THE BRAIN

The human brain is the largest and most complex part of the nervous system with a volume ranging from 1200 to 1500 cubic centimeters and an average weight of 1.35 to 1.4 kilograms [35]. It is composed of about one hundred billion neurons and innumerable nerve fibers, which allow the neurons to communicate with one another [40]. It controls all functions in the human body including, but not limited to, sensory systems, movement, behavior, emotion, memory and learning. These commands are carried out by neurons which are the functional unit of the nervous system that are specialized for rapid communication. A neuron is composed of a cell body, dendrites and an axon which carries impulses away from the cell body (Figure 11). When the brain or spinal cord is damaged, generally the axons don't recover and permanent disability occurs.

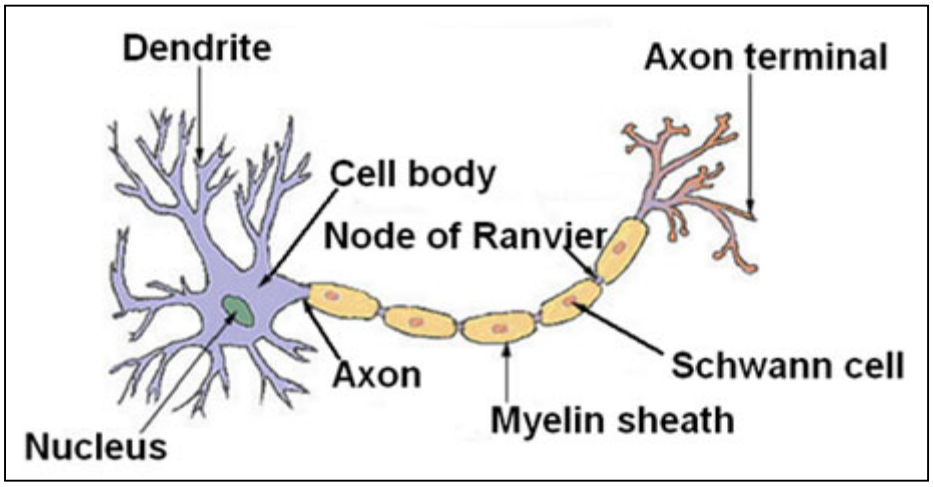

Figure 11: Structure of a Typical Neuron [41]

The cerebrum is the largest part of a mature brain and consists of two large masses called cerebral hemispheres connected by a deep bridge of nerve fibers called the corpus callosum. The cerebrum is further divided into five lobes (Figure 12), each of which is named after the skull bone that it underlies [40].

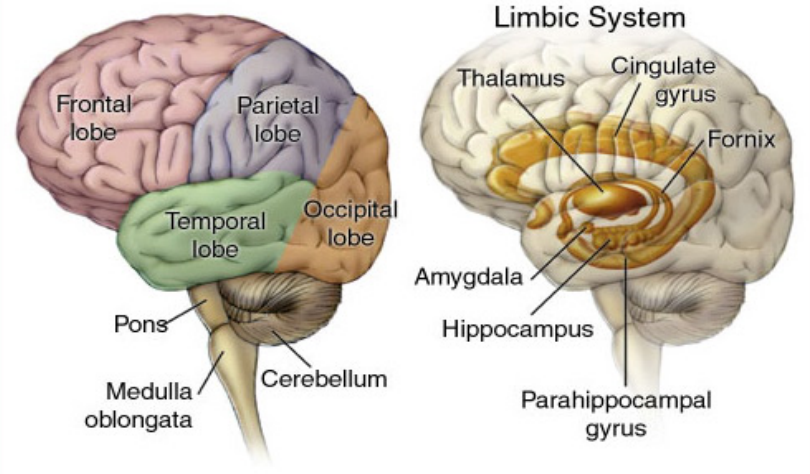

Figure 12: Brain Anatomy [42]

The cerebrum is concerned with the higher brain functions; it contains centers for initiating voluntary muscle movements as well as centers for interpreting sensory impulses from various sense organs. It also stores memory information and utilizes this information in the processes associated with reasoning [40].

The cerebrum can be further divided into two parts; the cerebral cortex and the white matter. The cerebral cortex, or grey matter, covers the surface of the brain. It is a superficial layer of grey matter formed by migrating peripheral neurons and is 2 to 5 millimeters in thickness [40]. The white matter lies beneath the grey matter and is composed primarily of myelinated axons [35] and is the area commonly damaged in cases of diffuse axonal injury [43].

3.4 PROTECTIVE LAYERS OF THE BRAIN

The brain floats within the skull suspended in Cerebro Spinal Fluid (CSF) and is protected by many layers (Figure 13) including the skull. The surface of the brain consists of folds (gyri), grooves (sulci), and fissures which subdivide the brain into hemispheres and smaller areas [34].

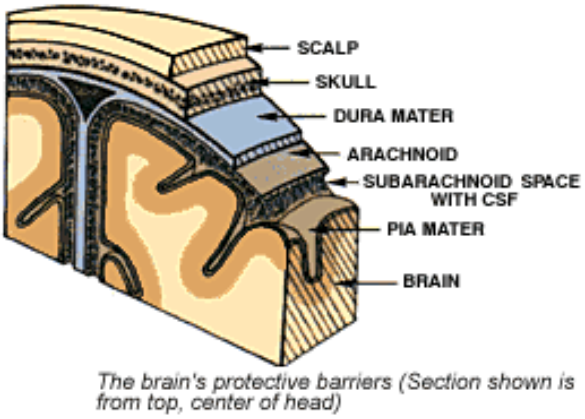

Figure 13: Layers Protecting the Brain [44]

The Dura Mater is a connective tissue composed of two fibrous layers and is the strongest of the three connective tissue layers (cranial meninges). The Dura Mater is itself composed of two layers, which are fused together except in certain areas where blood-filled spaces (dural venous sinuses) are formed. These spaces are normally triangular in cross-section and are primarily used to drain blood from the brain and transport it to the jugular veins. Under trauma, the layers of the Dura Mater can separate and fill with fluid or blood; this is known as epidural hematoma [35].

The Arachnoid is composed of a web of collagen and elastic fibres. The subdural space is a potential space that exists between the Arachnoid and the Dura Mater and should this become an actual space and fill with blood or fluid it is known as a subdural hematoma [35].

Cerebrospinal fluid (CSF) is a clear, colourless liquid that bathes the exposed surfaces of the central nervous system, completely surrounding the brain and spinal cord. The CSF supports the brain (95% of its weight) and prevents it from being crushed under its own weight. CSF also provides a liquid cushion to protect neural structures from sudden movement by impeding the motion of the brain relative to the skull [35]. CSF is a Newtonian fluid with a dynamic viscosity (μ) and density (ρ) similar to plasma ($\mu = 0.01$ and $\rho = 1.0$ g/cm3) [45]. The CSF is secreted and reabsorbed continuously resulting in a relatively constant fluid pressure of about 10 mm Hg (1333 Pa) [40].

4 INJURY

4.1 BLAST INJURY (GENERAL)

Blast injury can be identified by one of four categories; Primary, Secondary, Tertiary or Quaternary. Primary (blast) injury is caused by shock waves entering the body and causing damage to the surrounding tissues of hollow organs, including the lungs, intestines and ears, and subsequent hemorrhage and edema. Secondary injury is due to the impact and penetration of bomb fragments and debris. Tertiary injury is caused by the displacement of the whole body or body parts and their decelerative impact on obstacles. Quaternary injury includes other miscellaneous effects such as burns, gas and dust inhalation, and structure collapse [46].

Primary Blast Injury (PBI) generally occurs in the gas-filled organs such as the lungs or gastrointestinal tract. When a blast wave travelling faster than the speed of sound reaches body a large pressure results in rapid acceleration of the surface which creates a high-frequency stress wave that propagates through the tissue [47].

Injury from a blast is a function of the pressure and duration and the number of waves. At short durations there is an interaction between peak pressure and duration while at durations longer than 20-30 ms (such as those from nuclear blasts) the injury can be related to the overpressure alone [48]. The body position when exposed to the blast also has an impact on the injury threshold. Studies were undertaken to determine injury thresholds for various positions as well as proximity to a reflecting surface such as a wall. Being oriented end-on (lying down with either

head or feet pointed toward the blast) was found to provide the best protection against the blast wave [48].

Due to differences in their physical properties, various parts of the body surface react differently to the initial shock wave. Two general types of response are found; transmission of the pressure wave through the material and the gross deformation of the material as a result of the internally reflected stress wave [49].

4.2 HEAD INJURY IN BLAST

Brain injuries are a common occurrence from blasts but often go undiagnosed and untreated because of the attention focused on more visible injuries [8]. Since the brain is protected by the dura and the skull, it can be considered homogeneous and less susceptible to blast overpressure injury than other organs such as the lungs. However, in one 12-year study of 5600 terrorist bombings, 6% of the total casualties sustained skull and/or brain injury and within 24 hours, the overwhelming majority (91%) of these casualties died as a result of their head injuries [50].

The most common types of TBI for closed head injuries are diffuse axonal injury (DAI), contusion, infarction due to air embolisms and subdural hemorrhage (a loss of blood from a vessel). DAI occurs when shearing, stretching, and/or angular forces pull on axons and small vessels and is associated with 35% of all head injury deaths [51]. The differences in the mass and density of layers within the brain cause a relative motion between the layers. This can result in the axons being stretched, sheared, twisted, or compressed; ions and fluids then flow into the

axon and cause it to swell. The axon separates at the areas of such swellings and the farthest end of the axon from the cell body disintegrates. In the final stage of diffuse axonal injury, the distal end of the axon disintegrates, the remaining portion of the axon dies, and all that is left is a small retraction ball at the base of the cell body of the neuron [52]. Often the patient will be deeply comatose with extensor posturing (involuntary flexing or extending of the arms and legs) and may remain in a comatose or vegetative state. Patients who regain consciousness may suffer from long term deficits [51].

The movement of the brain within the skull can cause concussions and, should the brain impact the skull, contusions. Brain contusion in the absence of skull fracture always occurs at the frontotemporal basal area (where the frontal and temporal lobes meet) regardless of the direction of impact [53]. There are two theories to explain the phenomenon of brain contusion; shear strain theory, which considers cerebral contusion to be caused by high shear strain; and cavitation theory, which argues that negative pressure is the major cause of brain contusion. Accelerations greater than 80 g's are capable of lowering pressure in the brain to a point wherein cavitation occurs on the opposite side from the impact. Collapse of the vapor bubbles can lead to large pressures in excess of 1,000 atm, which can cause considerable local damage [54]. Concussion is defined as a clinical syndrome characterized by immediate transient impairment of neural function such as alteration of consciousness, disturbances of vision, equilibrium, etc. due to mechanical forces [55]. Subdural hemorrhage occurs when the brain moves within the skull enough to tear tributary surface veins that bridge from the brain surface to the dural venous sinus [3].

A direct impact to the head or an indirect impact applied to the head and neck when the torso is stopped or accelerated rapidly can result in head injury [56]. In either case, the head sustains a combined linear and angular acceleration. The type acceleration that governs head injury has generally been considered to be primarily linear. This is demonstrated by the use of only linear acceleration in the predictive injury criteria used for automotive crash testing in the past 30 years [57], the Head Injury Criteria (HIC). It has been found that linear acceleration induced brain motion is very small, on the order of ± 1 mm, while angular acceleration induced brain motion is limited to ± 5 mm, if the magnitude of the acceleration is in excess of 10,000 rad/s^2[56]. It was also found that angular acceleration contributes more than linear acceleration to the generation of concussive injuries, diffuse axonal injuries, and subdural hematomas (a pooling of blood outside of a vessel) [56].

Given the short duration of blast loading and the inertial properties of the head, the head is typically loaded and unloaded by the blast prior to significant motion being induced [58]. It has been found that the accelerations of the head induced by hitting the ground following the blast can be much higher than the accelerations from the initial blast wave loading [24]. This tertiary injury can make it difficult to isolate the injury caused by just the blast overpressure. It is also difficult to separate the physiological from the psychological injuries that are inflicted by blast which can mask more serious symptoms [59].

4.3 INJURY CRITERIA

A valid injury criterion has been defined as "a biomechanical index of exposure severity which, by its magnitude, indicates the potential for impact induced injury" [60]. Relating measurable parameters or response to injury is a significant challenge, particularly for head injury, since physical symptoms may be very difficult to identify, and psychological symptoms may not become apparent for some time after the injury [61]. These challenges are further compounded by being unable to apply injurious levels of loading in experimental testing using live human subjects. Injury criteria for blast loading are currently under development by many researchers since the low duration and high accelerations induced by blast waves may not be appropriate for existing criteria.

The most commonly used criteria for predicting head injury in automotive crash scenarios is the HIC which uses the resultant linear acceleration of the head to calculate a value which is then related to a tolerance value (Equation 4.1) [55]. There are two different tolerance levels depending on the duration of the "window" used for calculating the HIC; HIC_{15}=700 (15 ms window) and HIC_{36}=1000 (36 ms window). A HIC_{36} value of 1000 and a HIC_{15} value of 700 are associated with an 18% probability of life-threatening brain injury [57]. The HIC was developed from the Wayne State Tolerance Curves and the Gadd Severity Index [24] and has been used in previous injury studies for blast protection against Anti-Personnel mines [62], [63].

$$\mathrm{HIC} = \left[\frac{1}{(t_2 - t_1)} \int_{t_1}^{t_2} a(t)dt\right]^{2.5} (t_2 - t_1) \qquad \textbf{(Equation 4.1)}$$

A limitation in the HIC is primarily the lack of correlation between the HIC values and an AIS injury severity level [64]. The assumed time dependence of the tolerable average acceleration leads to predictions that short-duration, high acceleration events and long-duration, low acceleration events yield equal risks of closed head injury [57]. The HIC is also not injury specific and does not account for variation in brain mass or include a description of the kinematics associated with the head injury [65].

Various criteria have been proposed to address this issue by providing tolerance curves for different forms of head injury or making a correlation to the injury scale. Previously proposed criteria include tolerance curves and limits for DAI [65], intracranial pressure [66], and the stress and strain within the brain tissue [67][68][56]. The theory behind using acceleration as an injury criterion is based on Newton's second law which relates acceleration to the force applied to a rigid body. Because the brain is viscoelastic in nature, its impact response is more complex than a rigid body [69].

A proposed criterion for diffuse brain injury uses rotational velocity and rotational acceleration as measures for injury. Tolerance curves were created for various injury levels which were then related to the AIS scale [70]. Literature was used to create estimates for injury thresholds for categories ranging from mild Classic Concussion (mCC) to severe Diffuse Axonal Injury (sDAI) [70] (Figure 14). The typical duration of the acceleration pulse for this criterion is 25 ms, which is much larger than the typical pulse duration of less than 1ms for blast loading.

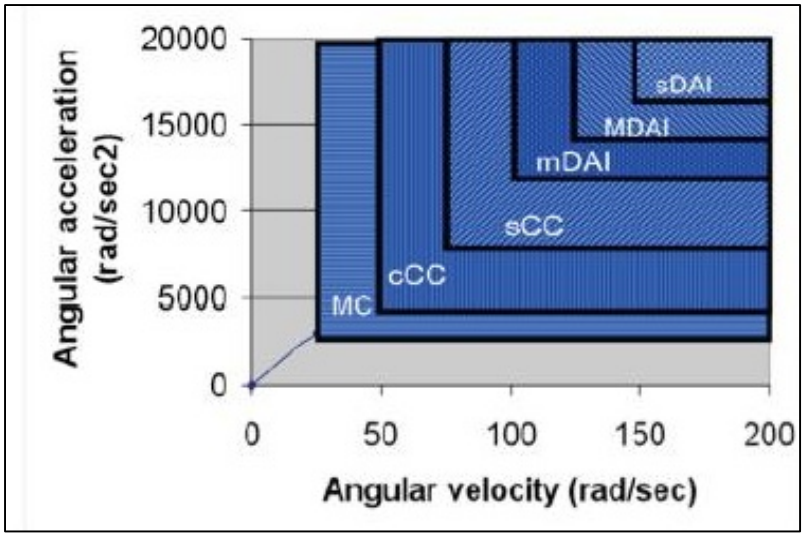

Figure 14: Angular Tolerances for Diffuse Brain Injury [70]

Another recently proposed criterion, the Head Impact Power (HIP) criterion, is based on the rate of change of translational and rotational kinetic energy and states that a certain level or probability of injury will occur to a viscous organ if the product of compression and rate of compression exceeds some limiting value [71]. This criterion was developed using NFL football TBI cases and is a combination of HIC and the Angular Tolerances for Diffuse Brain Injury in the sense that it considers all six degrees of motion to predict injury [64].

The equation for HIP (Equation 4.3) is derived by setting the coefficients for the general expression for the rate of change of translational and rotational kinetic energy for a rigid object (Equation 4.2) equal to the mass and appropriate mass moments of inertia for the head.

$$\text{Power} = P = \sum m\bar{a} \cdot \bar{v} + \sum I\,\bar{\alpha} \cdot \bar{\omega} \qquad \textbf{(Equation 4.2)}$$

$$\mathrm{HIP} = 4.50a_x \int a_x dt + 4.50a_y \int a_y\, dt + 4.50a_z \int a_z\, dt + 0.016\alpha_x \int \alpha_x\, dt + 0.024\alpha_y \int \alpha_y\, dt + 0.022\alpha_z \int \alpha_z\, dt \quad \textbf{(Equation 4.3)}$$

Once a HIP value has been calculated, it can be compared to an experimentally derived curve to determine if injury, in this case concussion, will occur (Figure 15).

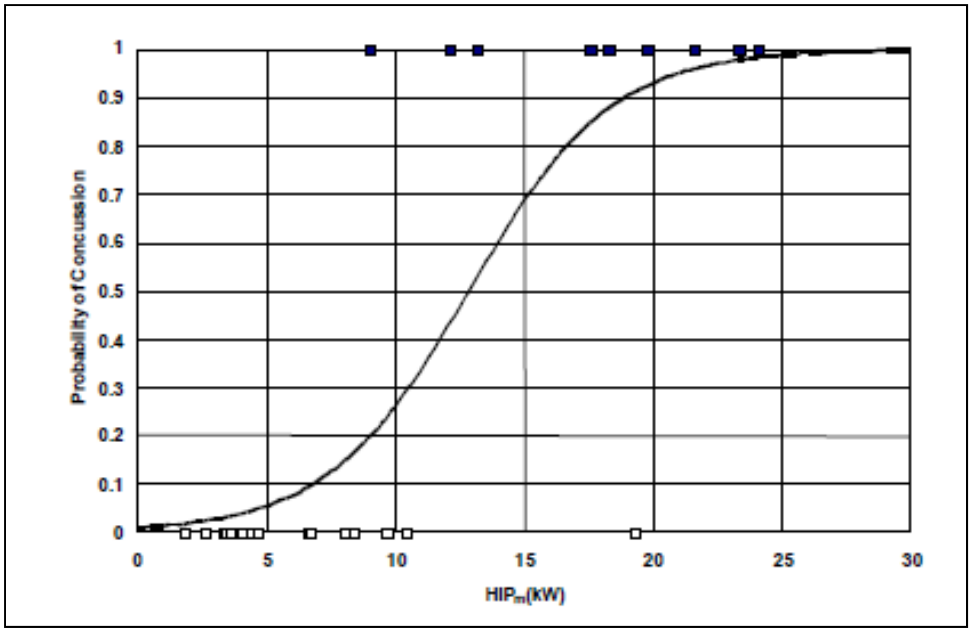

Figure 15: Probability of Concussion based on HIP [64]

Since this criterion was only developed for concussions and is a pass/fail value, it may not have relevance to blast injury prediction. However, rotational accelerations and velocities should not be excluded for blast injury prediction since a low height of burst scenario could make these components higher than their linear counterparts.

For the shear stress within the brain, thresholds for a number of probability values of Mild TBI (MTBI) have been proposed. In one study, the shear stresses that would result in a 25%, 50%, and 80% probability of MTBI were determined as being 6.0, 7.8, and 10.0 kPa respectively [68]. Other researchers have suggested that pressures of 11-16.5 kPa [72] and 8-16 kPa [73] can be regarded as the brain injury limits. The highest shear stresses in previously investigated numerical models have occurred in the brain stem and corpus callosum region where DAI is commonly reported [22].

Principle strain has also been proposed as a brain injury metric. Research performed on rats at Wayne State University has led to the proposing of the Cumulative Strain Damage Percentage Measurement (CSDPM) which accounts for the strain magnitude, percentage and volume ratio of cell loss in the brain. Their results showed that a peak maximum principle strain of 0.121 correlates with TBI [74].

Simulations and tests performed by Ward et al have shown that serious brain injuries occur when the peak intracranial pressure exceeds 34 psi (234.4 kPa). Brain Pressure Tolerance (BPT) curves (Figure 16) were created for various impact scenarios in the form of acceleration pulse shapes and it was found that exceeding the limits resulted in an AIS injury level of 5 or 6 [66]. However, these curves were based on a numerical model of the brain with a very coarse mesh and simplified material properties which could detract from the validity of the results.

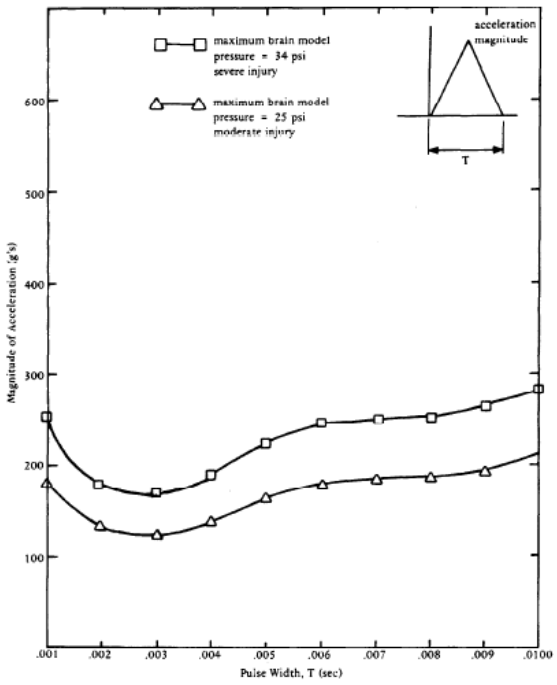

Figure 16: BPT Curve for Triangular Pulse [66]

All of the above criteria consider the acceleration and velocity of the head; however some studies have found that the response of the head is decoupled from the body due to the lack of significant displacement under primary blast loading [69].

5 HEAD PROTECTION

Protection to the head involves a combination of many factors including environmental protection, eye protection, hearing protection, protection from concussive shock, compatibility with equipment such as a mask and communication equipment, and comfort [75].

The first modern standardized military helmet was developed by the French in World War I and helmets based on this design were later used by British, Americans and Germans [75]. Following WWI, the American Military Infantry Board released the following statement in a report that would direct the design of future military helmets:

"The ideal shaped helmet is one with a dome-shaped top following the full contour of the head and supplying uniform headroom for indentation, extending down the front to cover the forehead without impairing vision and down the sides as far as possible to be compatible with the rifle, etc., and down the back as far as possible without pushing the helmet forward when in a prone position, and with a frontal plate flanged forward as a cap-style visor and the sides and rear flanged outward to deflect rain from the collar opening." [76]

One of the most famous helmet designs was the M1 Hadfield (1941) used by the United States military during World War II. It consisted of a steel shell with a modified Riddell football helmet suspension system (Figure 17). The main focus for this helmet was stopping projectiles, specifically, it was designed to resist penetration by a 230-grain, caliber .45 bullet with a velocity of 800 feet per second [75].

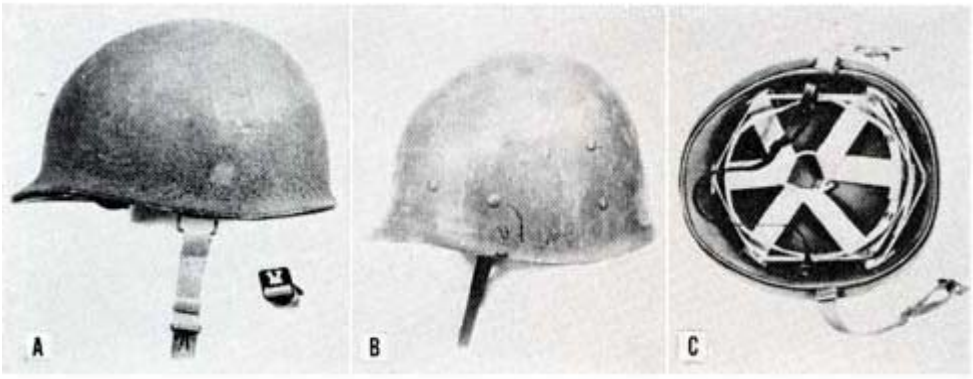

Figure 17: Army M1 Helmet A. Outer Steel Shell. B. Inner Liner. C. Liner with head suspension system [76]

The M1 was replaced in the 1980s with the Personnel Armor System for Ground Troops (PASGT) helmet. This helmet is a one piece structure composed of multiple layers of Kevlar® fibre and phenolic PVB resin [77] with an areal density of approximately 330 oz/yd^2 (2.30 psf) [78]. This helmet had been the standard issue for armed forces in the United States until recently where it is being replaced by the Advanced Combat Helmet (ACH) [79]. The Canadian Forces replaced the M1 with the CG634 combat helmet which closely resembles the ACH. Although they are similar, the CG634 and ACH are too new to allow for public release of their geometry and materials. In this study, the PASGT helmet geometry and properties were used.

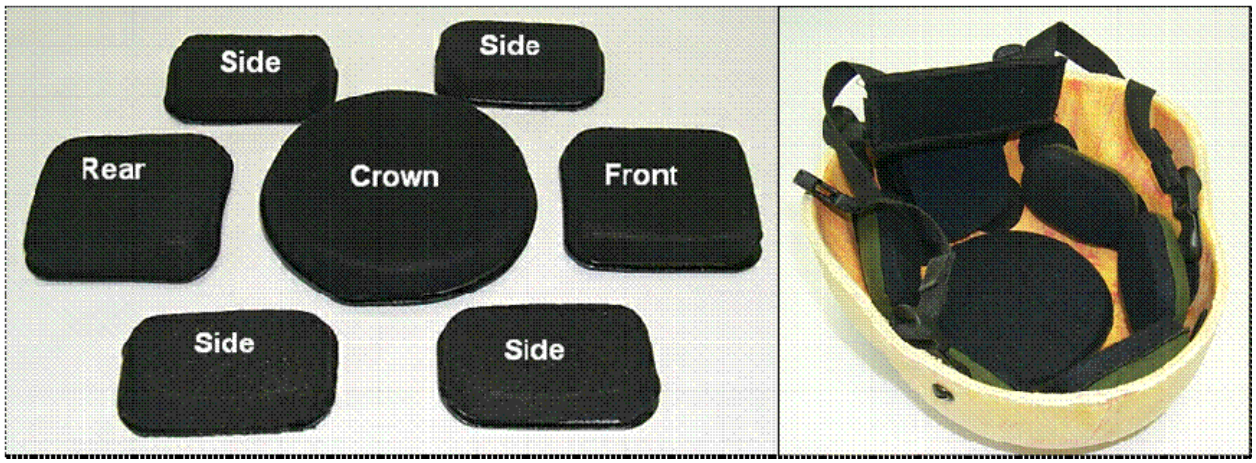

Figure 18: Viscoelastic Foam Pad System for ACH (photo courtesy of Kevin Williams, DRDC Valcartier)

Previously, the Canadian Forces (CF) and US Military have utilized a strap support system underneath their helmets which leaves an air gap between the helmet and the head. Newer model helmets with a system of foam pads are now in service with improved fit and comfort (Figure 18). These foam pads may also provide a measure of protection against blast since it has been found that by placing a relatively heavy rigid material in front of a foam, a shock wave will mostly be reflected by the heavy material and very little will transmit into the foam [80]. The foam will instead act to damp the acceleration of the helmet, thus reducing the acceleration experienced by the head.

5.1 ARAMID FIBER COMPOSITE HELMETS (KEVLAR®)

Aramid fibers are defined by the US Federal Trade Commission as "a manufactured fiber in which the fiber-forming substance is a long chain synthetic polyamide in which at least 85% of the amide linkages are attached directly to two aromatic rings". The most well known name for aramid fiber is the DuPont brand name Kevlar®. This material was first commercialized in 1972

and gained popularity as a protective material due to its high tensile properties, light weight, high impact resistance and damage tolerance, as well as its rapid vibration damping in reinforced composite structures [81].

The PASGT helmet was constructed of composite containing a 1500 denier Kevlar® 29 yarn in a 2x2 basket fabric construction that weighed 14.0 oz/yd2 (475 g/m2). The fabric was impregnated with 16-18% by weight of Polyvinyl Butyral (PVB)-phenolic thermoset resin. The helmets were fabricated by assembling a helmet preform using 19 equivalent layers of prepreg. These layers were then compression molded at constant temperature (between 320 -355 °F) and substantial compression pressures well over 500 psi [78].

Since the helmet composite is comprised of layers of fabric in a matrix, it behaves anisotropically when loaded. Previous studies on ballistic impacts on the PASGT helmet that utilized hydrocodes modeled the Kevlar as layers of solid elements with anisotropic properties [82][83]. The LS-Dyna anisotropic elastic-plastic constitutive model requires the declaration of all the stiffness matrix coefficients for the following constitutive relationship (Equation 5.1).

$$\begin{bmatrix}\sigma_{11}\\ \sigma_{22}\\ \sigma_{33}\\ \sigma_{23}\\ \sigma_{31}\\ \sigma_{12}\end{bmatrix} = \begin{bmatrix}C_{11} & C_{12} & C_{13} & 0 & 0 & 0\\ C_{21} & C_{22} & C_{23} & 0 & 0 & 0\\ C_{31} & C_{32} & C_{33} & 0 & 0 & 0\\ 0 & 0 & 0 & C_{44} & 0 & 0\\ 0 & 0 & 0 & 0 & C_{55} & 0\\ 0 & 0 & 0 & 0 & 0 & C_{66}\end{bmatrix} \begin{bmatrix}\varepsilon_{11}^{d} + \frac{1}{3}\varepsilon_{vol}\\ \varepsilon_{22}^{d} + \frac{1}{3}\varepsilon_{vol}\\ \varepsilon_{33}^{d} + \frac{1}{3}\varepsilon_{vol}\\ \varepsilon_{23}\\ \varepsilon_{31}\\ \varepsilon_{12}\end{bmatrix} \qquad \textbf{(Equation 5.1)}$$

In a study by Gower et al, previously calculated coefficients for the LS-Dyna constitutive model for Kevlar 29 were compared to those found in experiments to validate their numerical model. The values from the literature, experiments and their LS-Dyna model (Table 3) showed significant differences only in the tensile strengths in the warp and weft directions (S_1 and S_2).

Table 3: Comparison of numerical with experimental values for Kevlar 29 composite properties [83]

Property	Values reported in Literature	Initial Numerical Model Values	Experimental Value (Static Testing)
E_1 [GPa]	18.5	18.5	17.86
E_2 [GPa]	18.5	18.5	8.3
E_3 [GPa]	6.0	6.0	
ν_{12}	0.25	0.25	
$\nu_{31,32}$	0.33	0.33	
G_{12} [GPa]	0.77	0.77	0.85
$G_{13,23}$ [GPa]	5.43	2.71	
ρ [g/cm^3]	1.23	1.23	
S_1 [MPa]	1850.0	555.0	444.9
S_2 [MPa]	1850.0	555.0	225.5
CS [MPa]	1200.0	1200.0	~900
S_{12} [MPa]	77.0	77.0	56.7
$S_{13,23}$ [MPa]	543	898.0	
S_n [MPa]	34.5	34.5	
ISS [MPa]	9.0	9.0	
STF_1	0.1	0.03	0.045
STF_2	0.1	0.03	0.050

5.2 FOAM HELMET SUSPENSION SYSTEMS

Man-made foams are used for absorbing energy in impact situations (in packaging and crash protection) and in lightweight structures. The properties of a foam are related to its structure and to the properties of the material of which the cell walls are made [84].

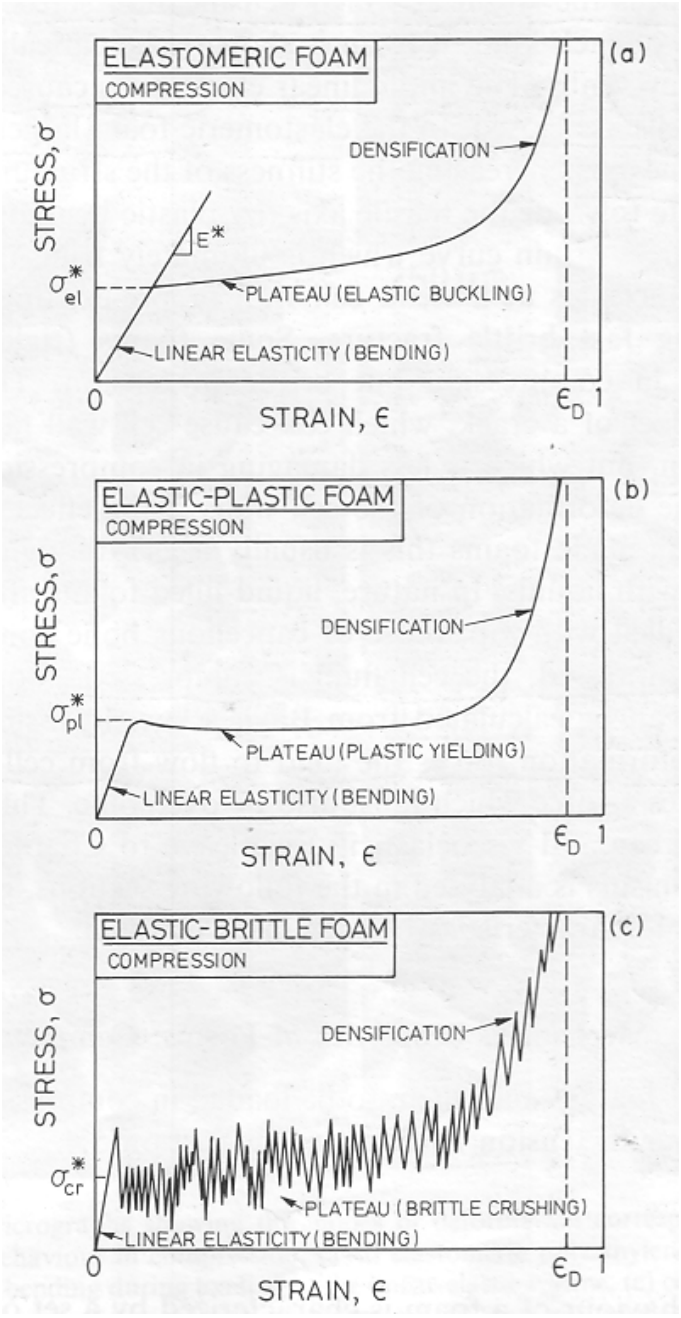

Figure 19: Compressive Stress-Strain Curves for Foams [84]

The above figure shows the compressive stress-strain curves for elastomeric (Figure 19 (a)), elastic-plastic (Figure 19 (b)) and brittle foams (Figure 19 (c)). These show a linear elasticity at low stresses followed by a long collapse plateau, truncated by a regime of densification in which

the stress rises steeply. Increasing the relative density of the foam will increase the Young's Modulus, raise the plateau stress and reduce the strain at which densification starts [84].

The linear elastic response is limited to small strains (typically 5% or less); however, elastomeric foams can be stretched or compressed to much larger strains than this and still have recoverable (elastic) deformation. This recoverable deformation, while elastic, is non-linear [84]. Foams made from materials with a plastic yield point (ie: metals or rigid polymers) will collapse plastically when loaded beyond the linear elastic regime. This collapse will result in a long horizontal plateau in the stress-strain curve, but this strain is not recoverable.

The final phase, densification, occurs when the large compressive strains crush the opposing cell walls together and the cell wall material itself is compressed. This causes a steep rise in the stress-strain curve tending to a slope of E_s (though this is much larger than the Young's Modulus, E^*, so it appears almost vertical) [84].

Metal foams can be superior to polymer foams where, owing to limited space, higher deformation stresses combined with an equal or better energy absorption behavior is required. A result of previous investigations is that a simple piece of foam does not necessarily represent an optimum energy absorber. Foams with closed outer skins (structural foams) or composite structures of profiles and foams can have a deformation behavior which makes them more suitable for such applications [85].

A previous study on the protective aspects of foam in helmets placed 0.25 inch thick foam inserts into the strap support system found in the PASGT helmet in order to reduce head injuries in the US Paratrooper Corps [86]. The foam used in the study, a “Volara” foam, was a closed-cell polyethylene foam [87] that was shown to improve the helmet’s impact absorption capabilities by an average of 23.8% for initial impacts and 13.3% for subsequent impacts. However, this impact absorption could not be directly correlated to a predicted reduction in head injury [86].

6 EVALUATION OF NUMERICAL METHODS OF BLAST LOADING

6.1 ANALYTICAL CALCULATIONS

Equations have been developed that allow for the calculation of the maximum static and dynamic pressures [11]. Scaled distance, Z, is commonly used for blast calculations and relates the charge distance, R, and weight of the charge, W (Equation 6.1). R is the distance from the center of the charge in meters, while W is the weight of the explosive in kg of TNT. The weight of any explosive charge can be converted to the equivalent weight of TNT by multiplying by the conversion factor based on ratio of specific energies between the two explosives. An alternative approach makes use of two conversion factors depending on whether the peak impulse or the peak overpressure is to be matched to the actual explosive [11].

$$Z = \frac{R}{W^{1/3}} \qquad \textbf{(Equation 6.1)}$$

The peak static overpressure, p_s [bar] (Equation 6.2), and the peak dynamic pressure, q_s [kPa] (Equation 6.3), can be found using relationships from Henrych [11]. The variable p_0 is the ambient pressure (101.325 kPa).

$$p_s = \frac{14.072}{Z} + \frac{5.540}{Z^2} - \frac{0.357}{Z^3} + \frac{0.00625}{Z^4} \quad (0.05 \leq Z < 0.3) \qquad \textbf{(Equation 6.2)}$$

$$p_s = \frac{6.194}{Z} - \frac{0.326}{Z^2} + \frac{2.132}{Z^3} \quad (0.3 \leq Z \leq 1)$$

$$p_s = \frac{0.622}{Z} + \frac{4.05}{Z^2} + \frac{3.288}{Z^3} \quad (1 \leq Z \leq 10)$$

$$q_s = \frac{5p_s^2}{2(p_s + 7p_o)}$$ **(Equation 6.3)**

The static and dynamic pressures can be added together to give the reflected pressure, ΔP_R, by using the following Rankine-Hugoniot relation (Equation 6.4) [17].

$$\Delta P_R = 2p_s + (1+\gamma)q_s \qquad \gamma=1.4 \text{ for air}$$ **(Equation 6.4)**

Reflected pressures were calculated for 6.7kg charges of TNT for values of R ranging from 1 to 5 meters; the pressures were then compared to those applied by LS-Dyna (Table 4).

Table 4: Calculated Pressure vs. LS-Dyna

R [m]	Z [m/kg$^{1/3}$]	p_s [kPa]	q_s [kPa]	ΔP_R [kPa]	Dyna [kPa]	% Difference
1.0	0.5305	2600	5120	17488	19895	13.8
1.5	0.7957	1210	1900	6980	7240	3.7
2.0	1.0609	729	923	3673	3726	1.4
2.5	1.3261	439	420	1886	1908	1.2
3.0	1.5913	295	216	1108	1139	2.8
3.5	1.8566	213	122	755	798	5.7
4.0	2.1218	161	74.8	502	534	6.4
4.5	2.3870	127	48.5	370	392	5.9
5.0	2.6522	104	33	287	291	1.4

The larger percent difference in the near field is to be expected since the combustion products and the fireball will affect the pressure profile [11]. The calculations for the mid and far field compare quite well with the pressures that are calculated within LS-Dyna using CONWEP.

6.2 VALIDATING BLAST LOADING

Since the physics of blast are so complex, it is important to ensure that the numerical codes are capturing all important effects to create the most accurate loading possible. The various methods of blast loading available were compared to experimental data for arrival time, positive phase duration and peak pressure.

The numerical implementation of CONWEP requires the input of the weight of the explosive expressed in the universal reference of kilograms of TNT. For C4 the conversion factor is 1.34 [88] which gives a TNT equivalent charge weight of 6.7 kg for a 5 kg C4 charge.

The spherical air burst formulation of CONWEP does not consider ground reflection or interaction, resulting in an important aspect of wave interaction missing for charges with low HOB. A second alternative, a hemispherical ground detonation, does consider ground reflection; however, it assumes that the charge is situated directly on the surface, so the incident wave will not propagate towards the ground when the charge is placed in the air and the resulting pressure will be lower than it should. The enhanced air burst formulation takes ground reflection and mach stem formation into account, but is only valid for a certain range of HOBs, and will result in an error when used outside of it. Since none of the standard methods of blast loading accurately simulated a low HOB detonation, a different approach was taken. To simulate the reflected wave a second charge was set equidistant under the ground, or mirrored, to provide a surrogate ground reflection wave for detonations at low heights of burst (Figure 20).

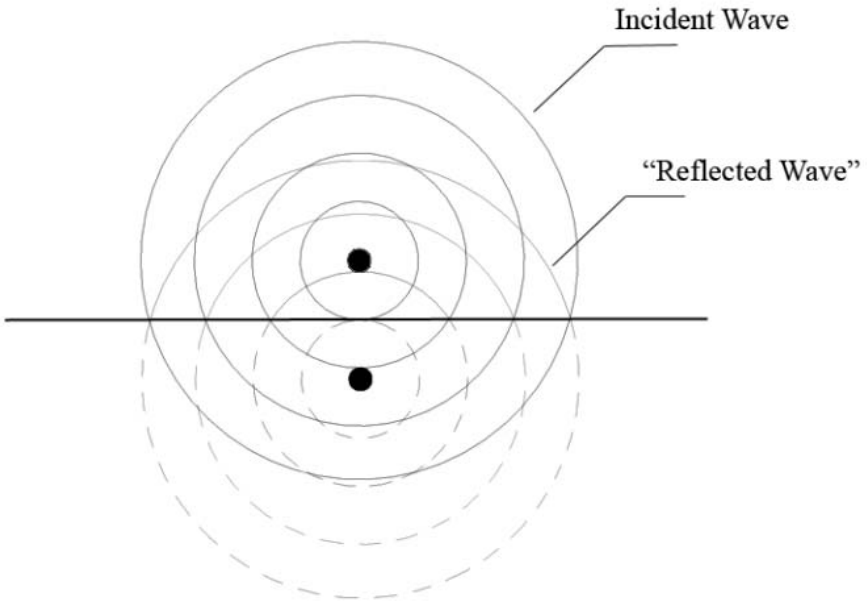

Figure 20: Mirrored Blast Schematic

The pressure-time histories for the numerical blast loading were acquired by applying the blast load to a rigid wall at the given standoff (Figure 21).

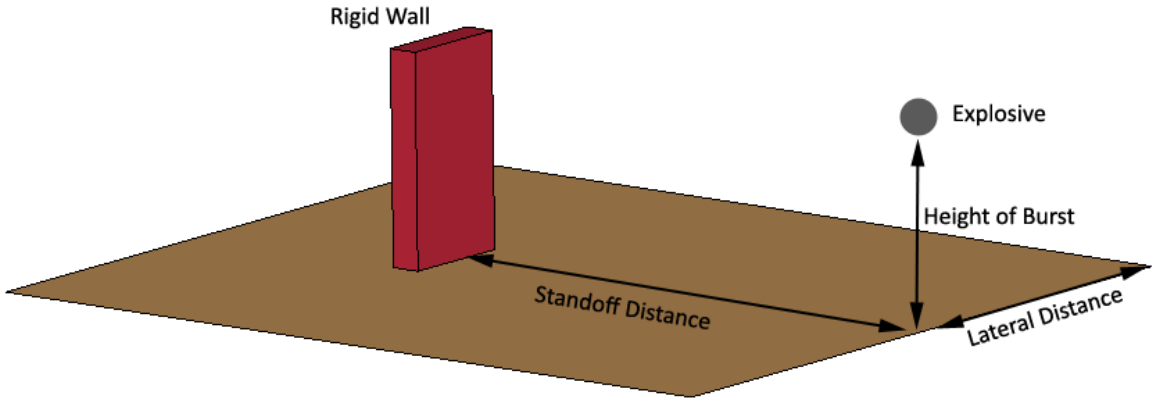

Figure 21: Setup for validation of blast loading

The blast wave parameters as predicted by the CONWEP equations and the LS Dyna implementation of CONWEP were compared to the experimental results. The error bars in the figures correspond to the minimum and maximum values in the experimental data (5 repeat tests for each condition).

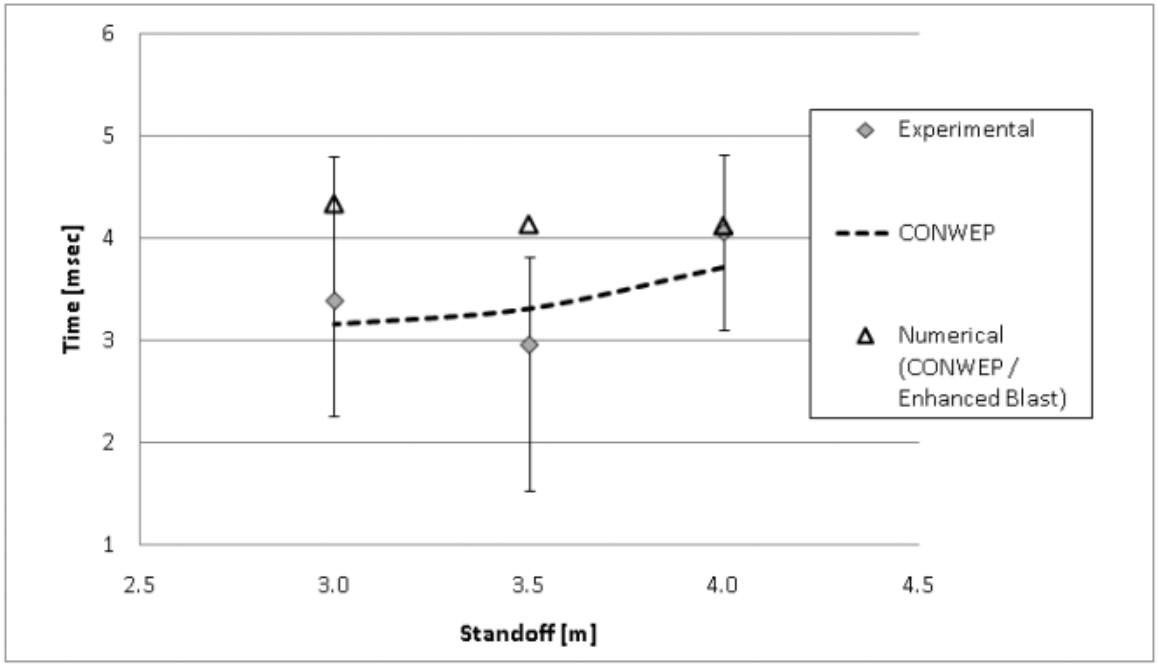

Figure 22: 1.5m HOB – Positive Phase Duration

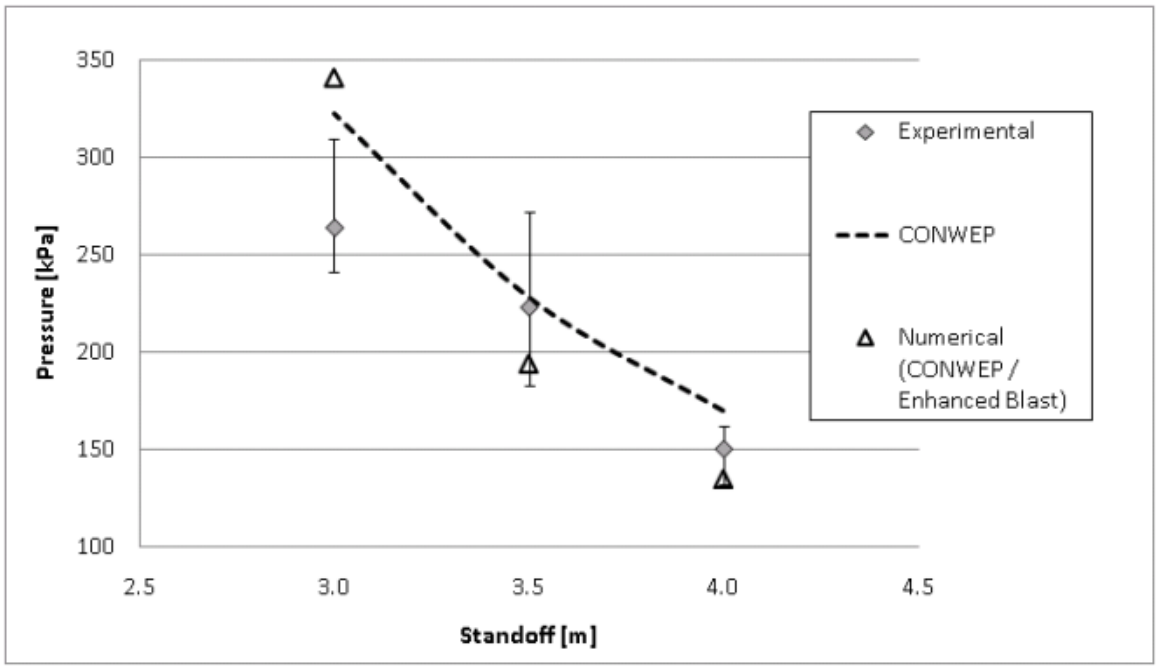

Figure 23: 1.5m HOB - Peak Incident Pressure

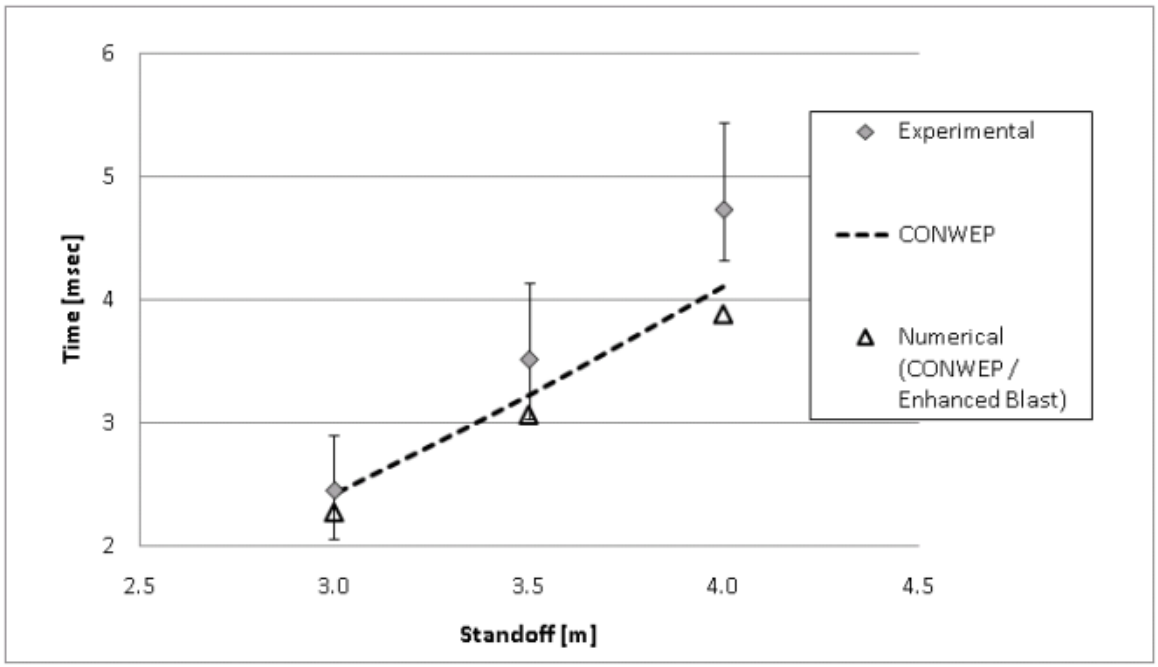

Figure 24: 1.5m HOB – Arrival Time

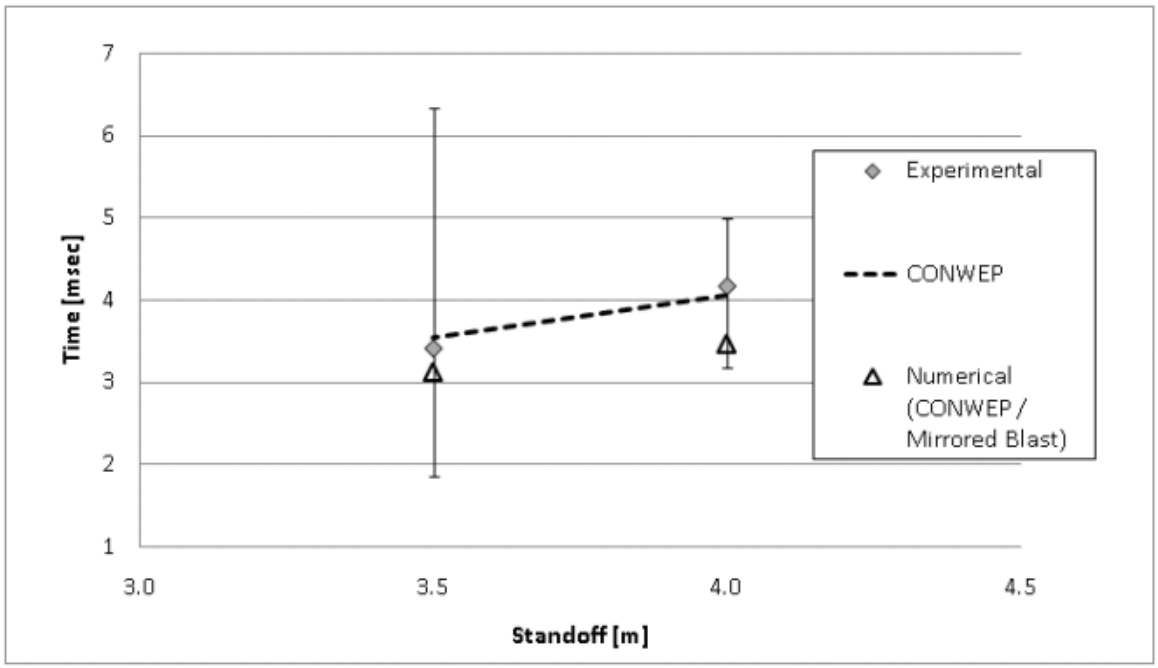

Figure 25: 0.2m HOB - Positive Phase Duration

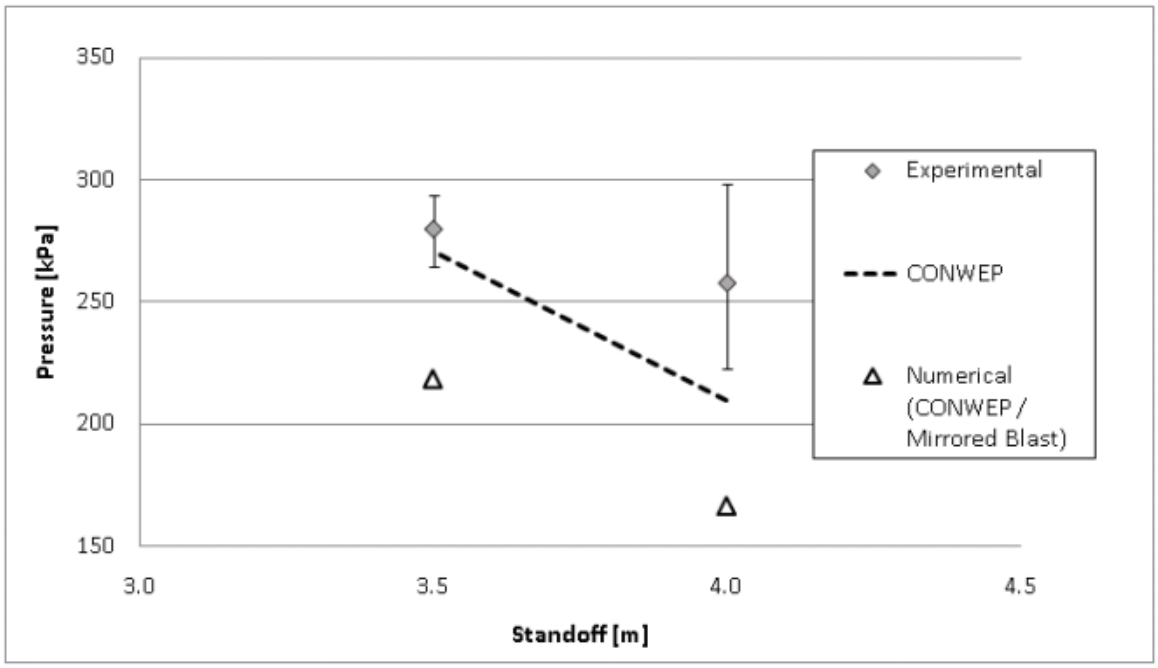

Figure 26: 0.2m HOB - Peak Incident Pressure

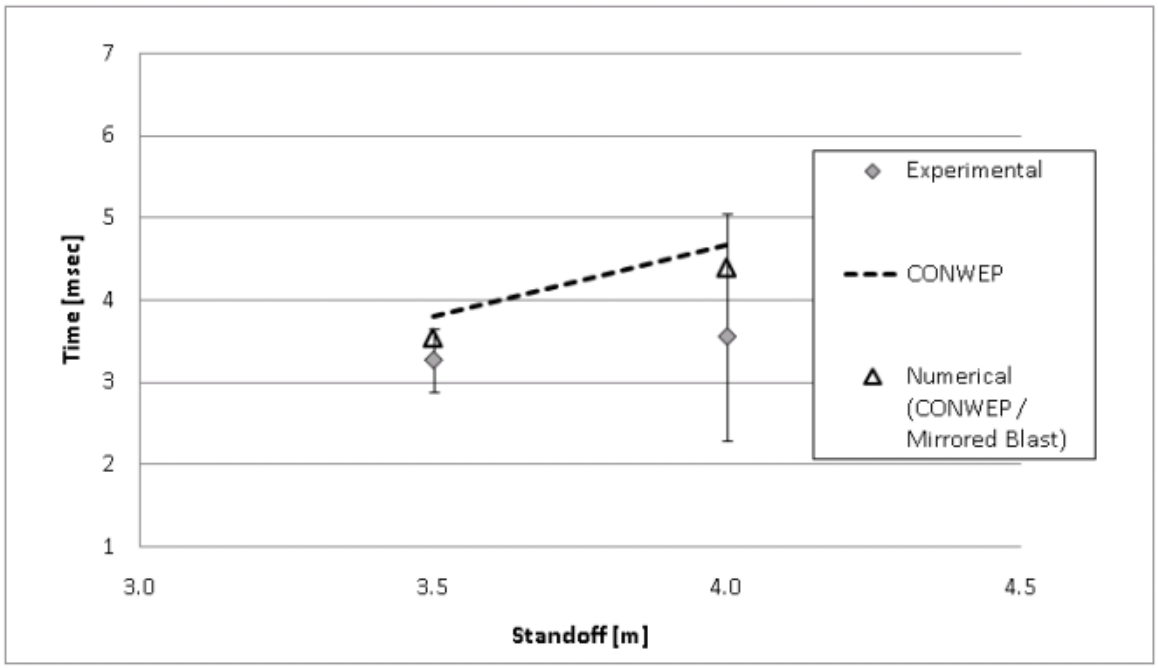

Figure 27: 0.2m HOB - Arrival Time

In general, the CONWEP results (equations and numerical implementation) were in good agreement with the experimentally measured blast data for both the 1.5 meter HOB cases (Figure 22 to Figure 24) and the 0.2 HOB cases (Figure 25 to Figure 27), based on peak static pressure, positive phase duration and blast wave arrival time. Differences in the peak pressures and arrival times for the low HOB can be attributed to using the mirrored blast approach to approximate the ground interactions.

For all future work, the enhanced blast option was used to model scenarios where mach stem formation played a role in the response. The mirrored charge approach was used for scenarios where the scaled HOB was below the lower bound on the range for the enhanced loading option.

6.3 VALIDATION STUDY – HEAD RESPONSE TO BLAST LOADING USING THE GEBOD MODEL

In order to accurately predict the injury due to the loading, the anthropometric values for the head had to be confirmed as being implemented in the numerical model. In this study the GEBOD ATD was used instead of the HIII due to its low computational cost as well as the ease at which one can acquire the acceleration data for use in the HIC_{15} calculation. The GEBOD model used was validated against the DRDC experiments which required the head mass of both surrogates to be the same.

As shown below in Table 5, the mass of the GEBOD head was approximately 300 grams lighter than the HIII head for the 50th percentile male. In order to bring the mass of the GEBOD head up to that of the HIII, an extra layer of shell elements was added and then attached to the existing GEBOD head to bring the total head mass to 4.54 kilograms. The attachment of the extra layer was done by tying coincident nodes together to ensure a rigid contact with no penetration.

Table 5: Anthropometric and ATD Dimensions and Masses

	Body Masses - NHANES 2002 [89]	Body Masses – GEBOD Database Values [90]	50th Male Hybrid III Mass [29];[91]	50th Male Hybrid III Mass [92]	GEBOD – LS-DYNA
Total Body Mass (kg)	86.183	77.3	78.15	78.2	78.61
Height (m)	1.76022	1.775	1.7526		1.774
Head Mass (kg)		4.679 ± 0.316	4.54	4.5	4.207

The predicted response of the GEBOD numerical model (Figure 28) subjected to loading for a 5kg C4 charge at 1.5m and 0.2 m HOB (3m, 3.5m and 4m standoff) was compared to the

experimental test data for the HIII (see section 2.7). The lateral distance was held constant at zero, consistent with the experiments. All acceleration data, including the unfiltered experimental data, was filtered using an SAE 1000 filter with a cutoff frequency of 1650 Hz [31] and was evaluated based on the peak acceleration (Figure 29 and Figure 32), impulse (Figure 30 and Figure 33) and HIC_{15} values (Figure 31 and Figure 34). Unfiltered acceleration data was also investigated and was found to have little impact on the HIC_{15} values except in the region close to the blast which already resulted in HIC_{15} values well above the injury threshold.

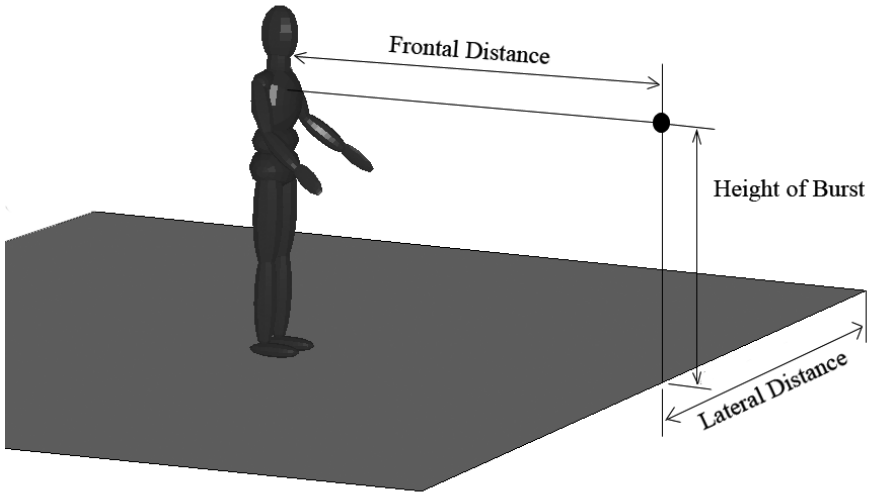

Figure 28: GEBOD Setup for Head Response Study

As with the study involving the validating of blast loading, the error bars in the figures indicate the minimum and maximum values of the experimental data. The head impulse results for the basic implementation of CONWEP are shown in the impulse comparisons (Figure 30 and Figure 33) for reference.

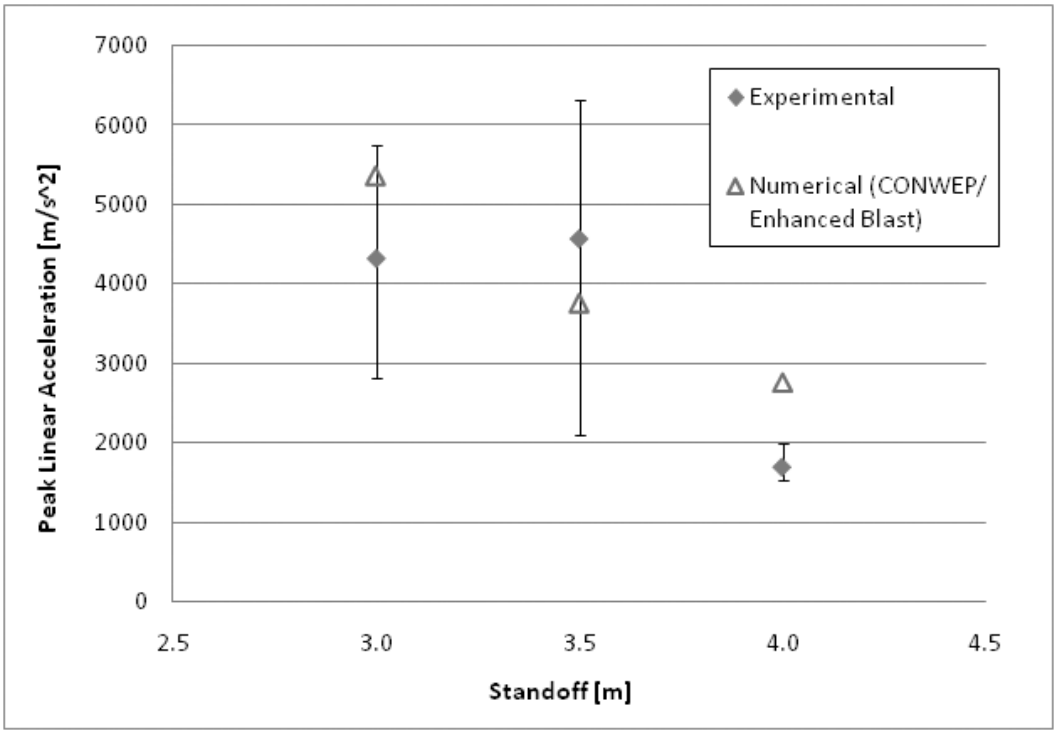

Figure 29: 1.5m HOB - Peak Linear Acceleration of the Head

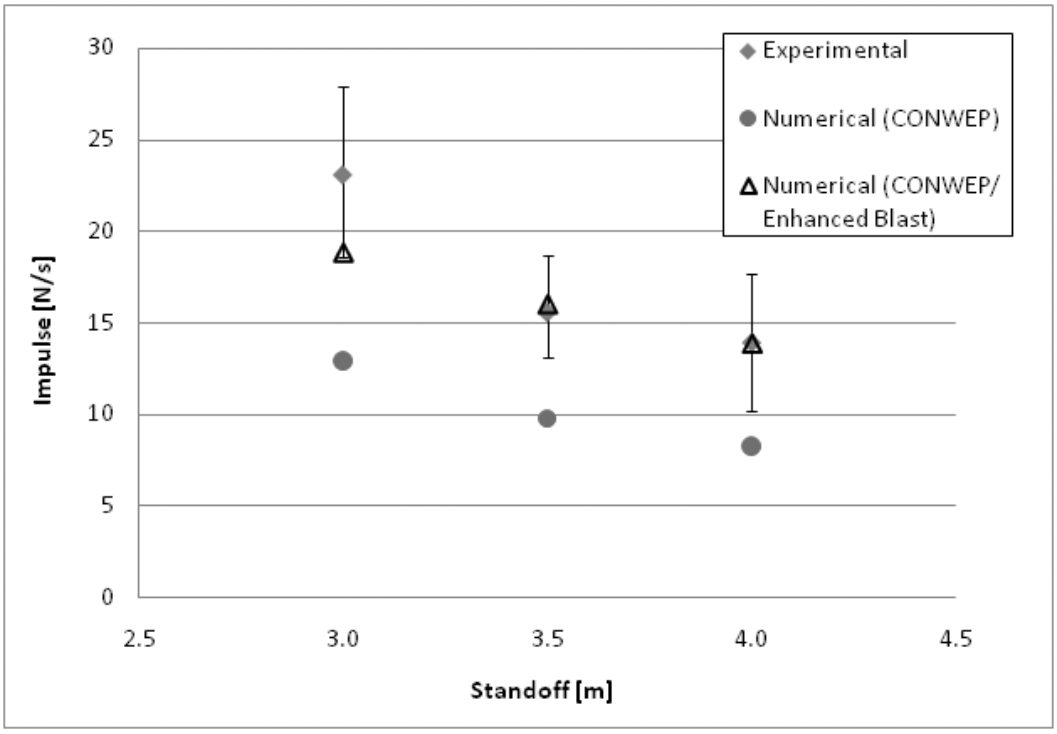

Figure 30: 1.5m HOB - Head Impulse

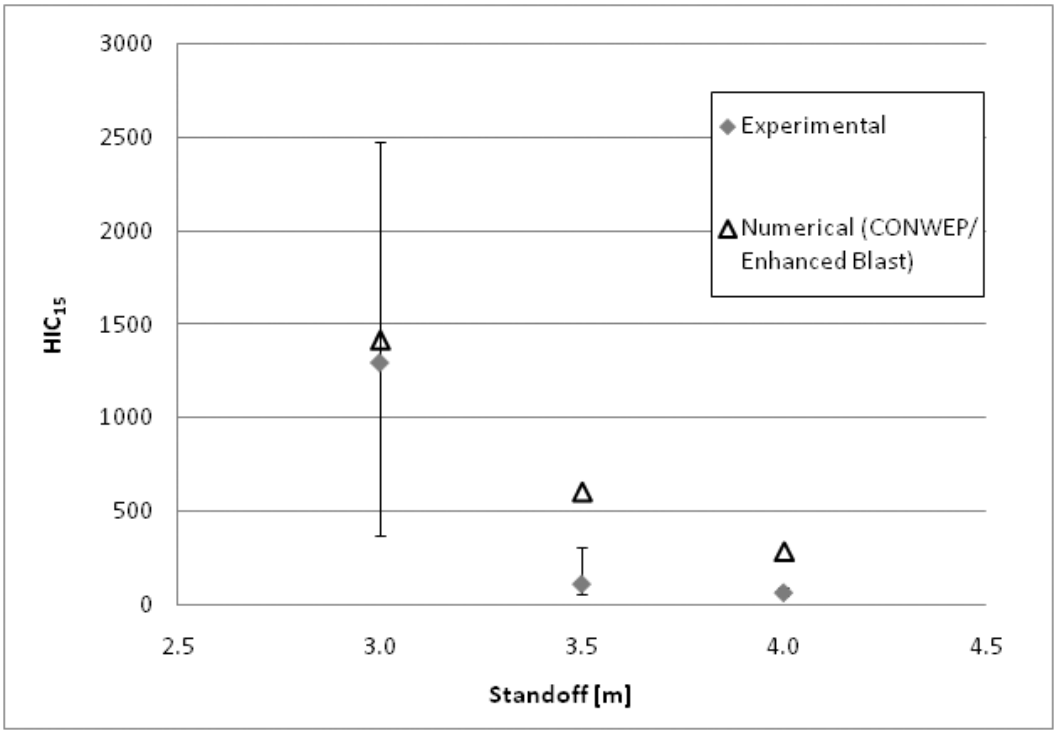

Figure 31: 1.5m HOB - HIC_{15}

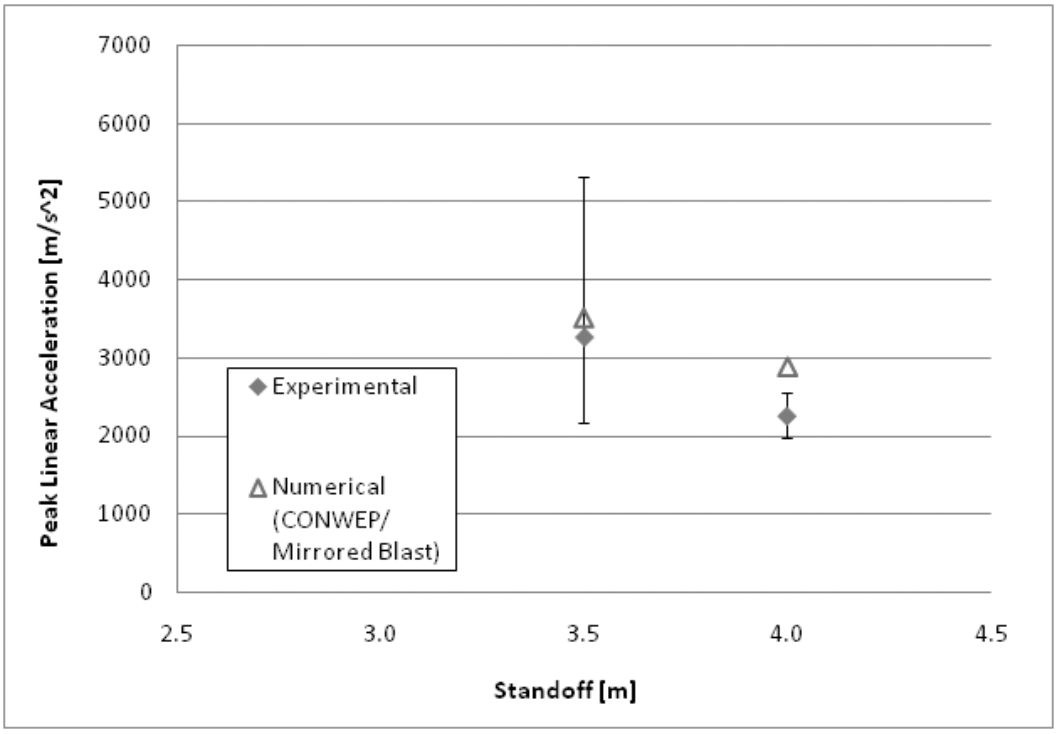

Figure 32: 0.2m HOB - Peak Linear Acceleration of the Head

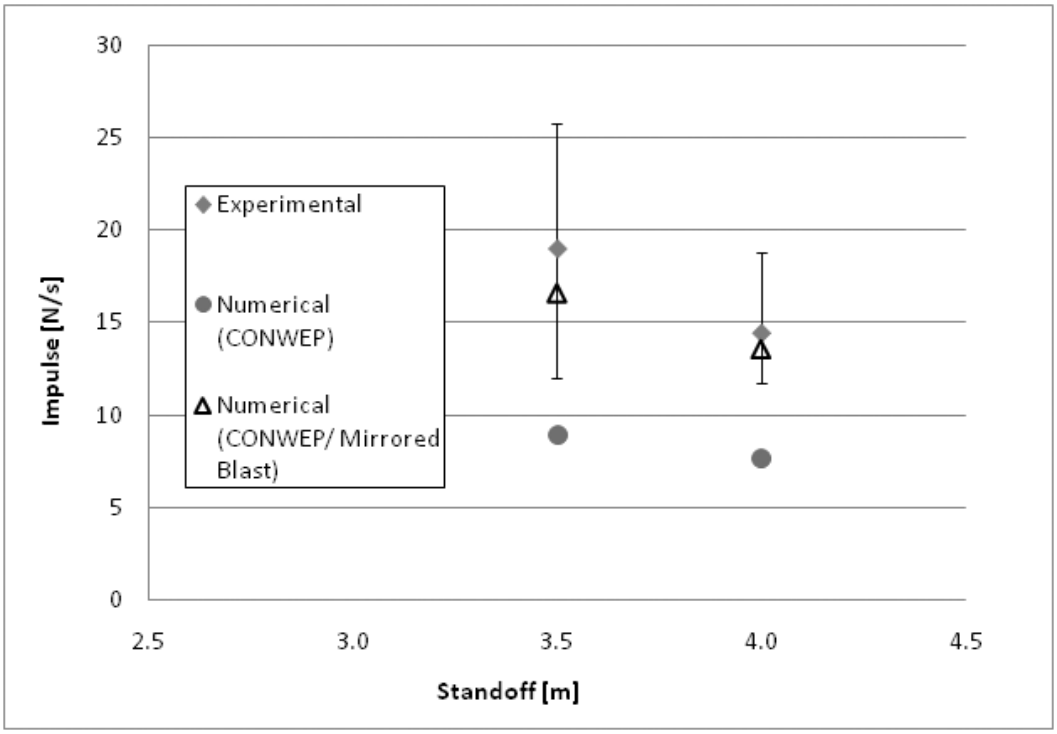

Figure 33: 0.2m HOB - Head Impulse

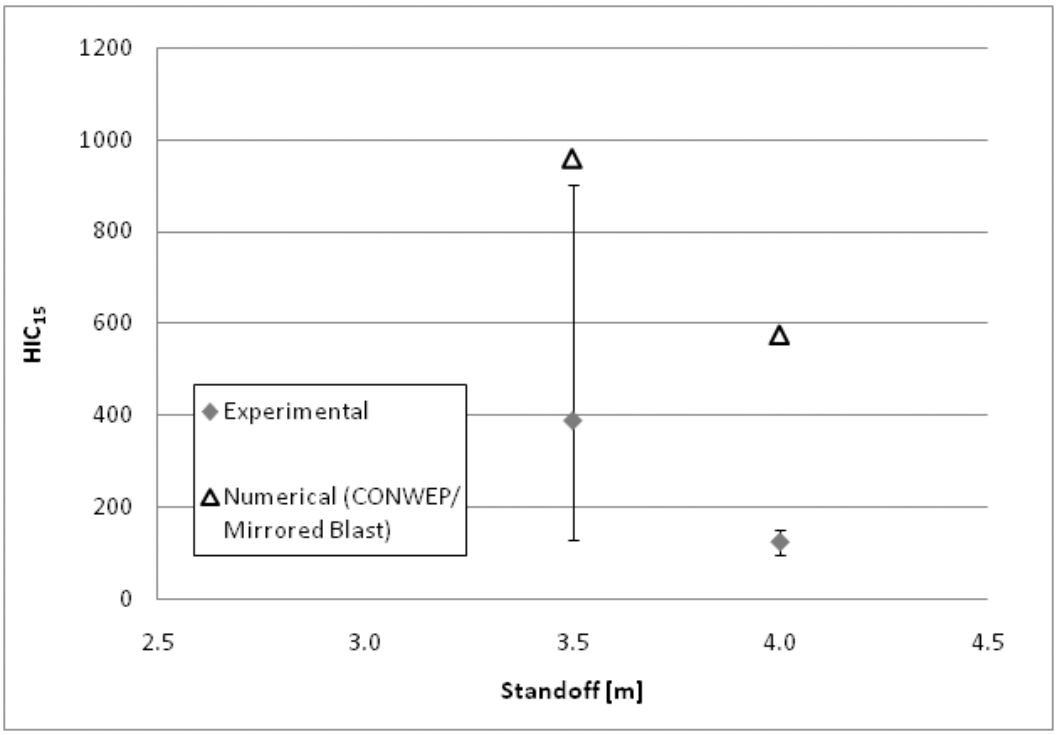

Figure 34: 0.2m HOB - HIC_{15}

The results for the enhanced CONWEP formulation were in good agreement with the experimental data for all three response parameters considered. For the cases using the mirrored blast approach, the results were in good agreement with the experimental data in terms of impulse, but the HIC_{15} values were much higher than those measured experimentally, possibly due to the sensitivity of HIC_{15} to small changes in the initial acceleration peak which was generally overpredicted by this approach (Figure 35). The predicted peak accelerations were in good agreement with the experiments for the 3.5m standoff but deviated for the 4.0m standoff.

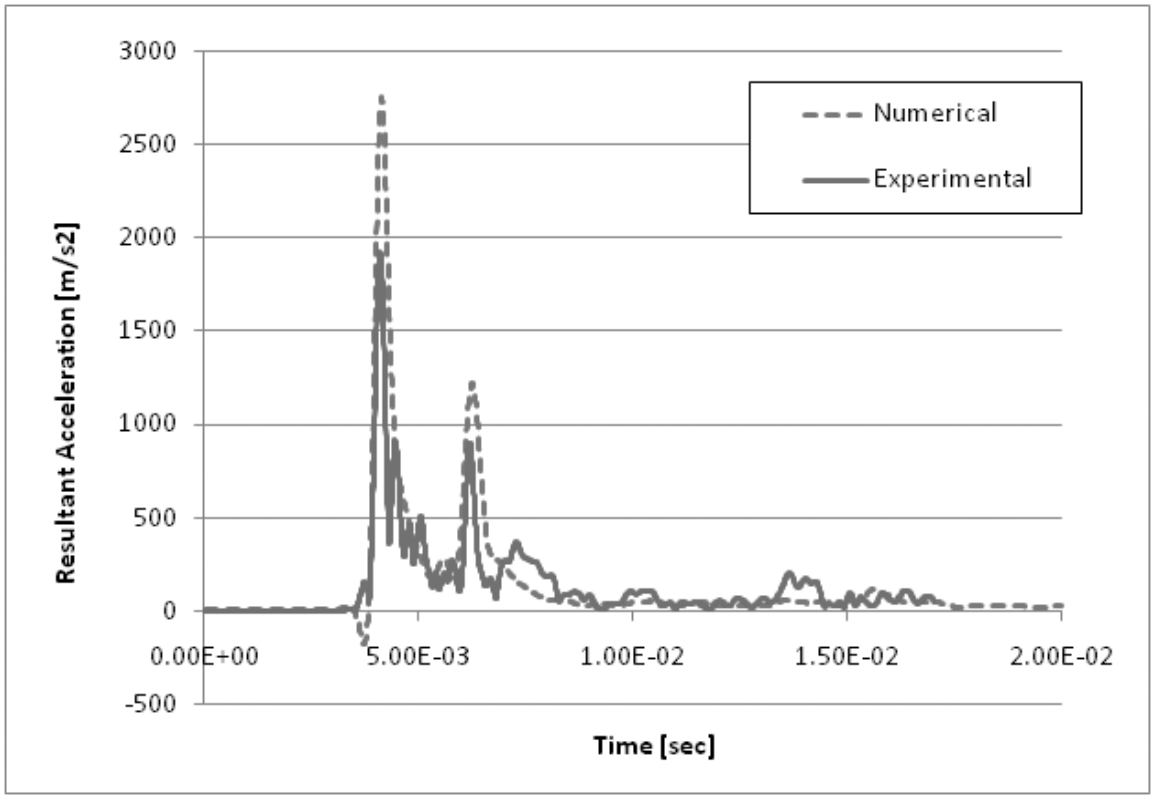

Figure 35: Example of Experimental versus Numerical Linear Acceleration Curves at the CG of the Head

Based on the results of this study, the gross kinematic response of the modified GEBOD model was a valid representation of that of a human under the same blast loading conditions.

6.4 PARAMETRIC STUDY – BLAST LOADING

A parametric study was undertaken using the GEBOD with CONWEP blast loading, with various charge sizes, HOB and standoff distances to investigate the response of the head related to the blast wave using the same setup as the head response study (section 6.3, Figure 28).

The effect of lateral distance was investigated for a 5 kg C4 charge with a constant HOB of 1.4 meters and a standoff distance of 5.4 meters (Figure 36). When compared to frontal distance, the lateral distance did not have a significant effect on the peak acceleration or HIC_{15} values. The increase in peak acceleration and corresponding increase in HIC_{15} was approximately 14 % over the range of lateral distances considered.

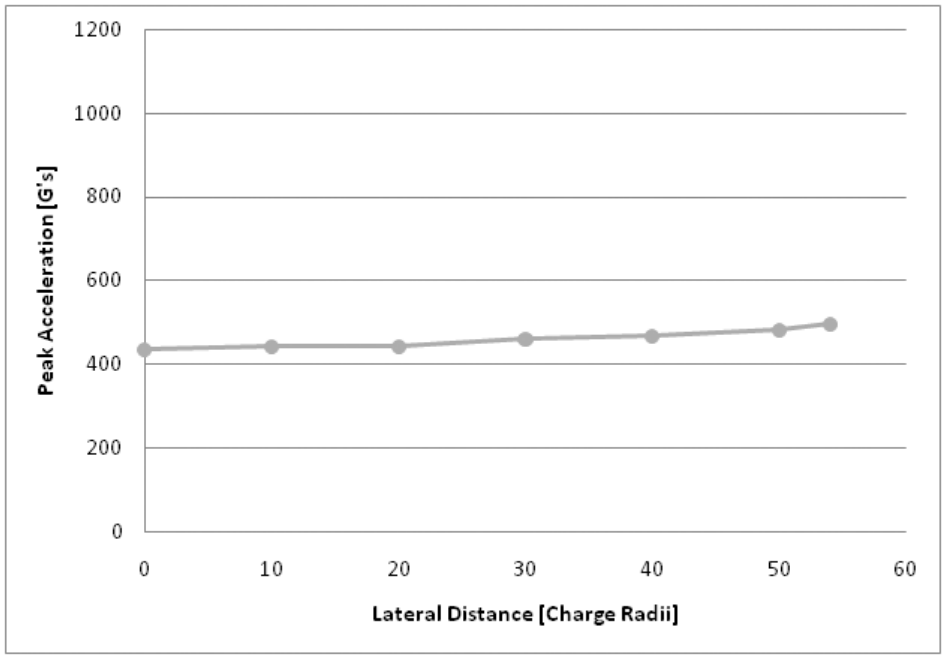

Figure 36: Peak Linear Acceleration of the Head as a Function of Lateral Distance

The effect of standoff distance was investigated by performing simulations with a fixed HOB of 1.4 meters, a lateral distance of 0 m, and a varying standoff distance. The peak linear acceleration (Figure 37) and HIC_{15} (Figure 38) values are plotted as a function of the normalized standoff distance in terms of number of charge radii. The charge radius was calculated to be the radius of a sphere of TNT corresponding to the explosive weight and is shown in brackets in the legend.

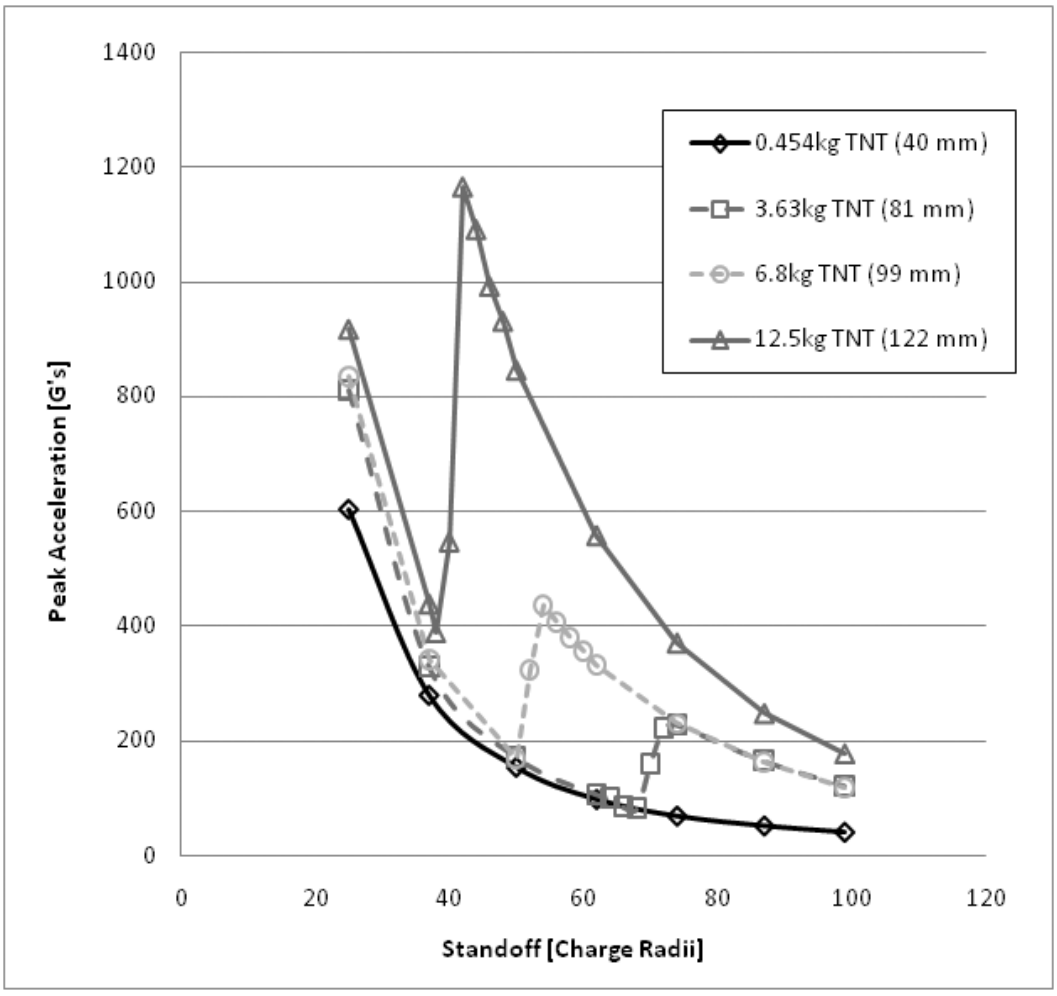

Figure 37: Parametric Study - Peak Linear Acceleration of the Head at 1.4m HOB

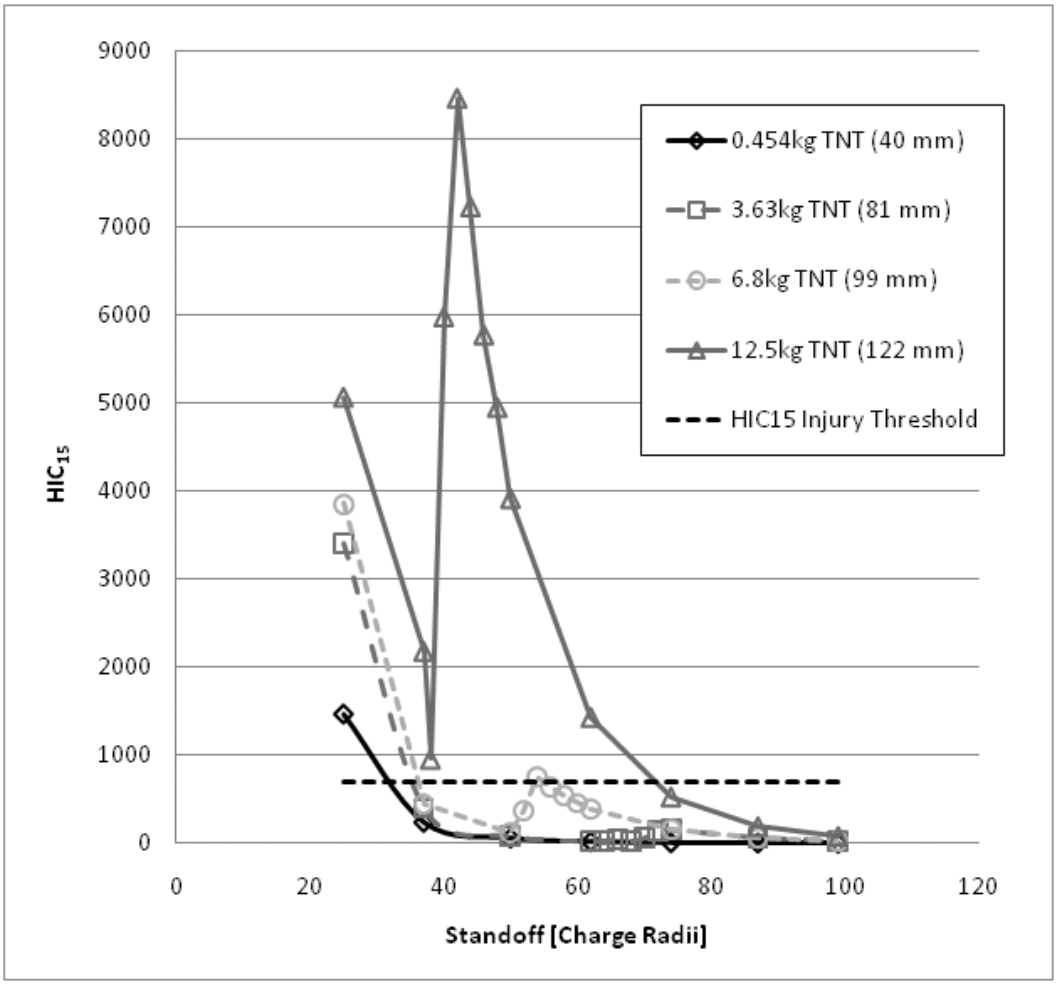

Figure 38: Parametric Study - HIC_{15} at 1.4m HOB

In all cases considered, the HIC_{15} injury criterion was exceeded in close proximity to the explosive (less than 35 charge radii). The HIP injury criterion was also investigated and was found to provide predictions that were consistant with the HIC_{15}.

The influence of the mach stem can be seen in both figures at intermediate distances from the charge (40 to 60 charge radii). For larger explosive weights, the peak acceleration in the mach stem region, below the triple point, can exceed the peak acceleration that occurs when in close proximity to the explosive, as shown in Figure 37.

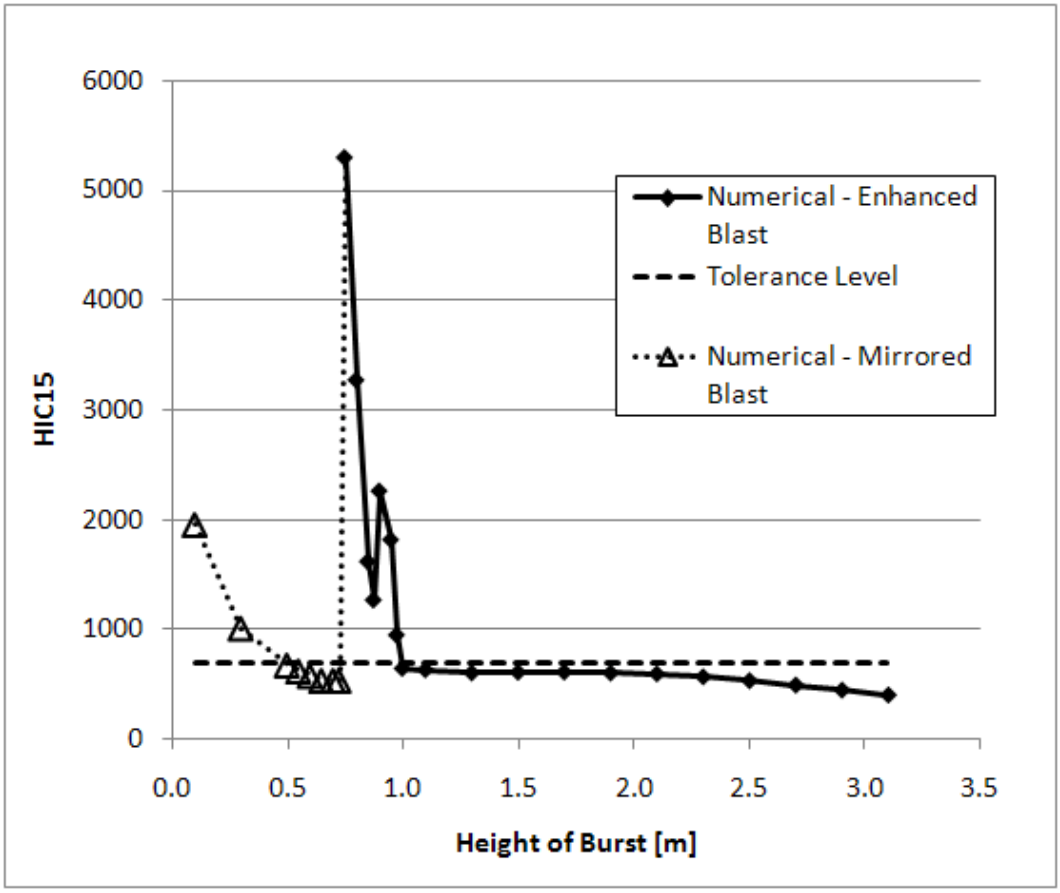

Figure 39: Parametric Study - HIC_{15} for Varying HOB

HOB was investigated by simulating detonation of a 5 kg charge of C4 for HOB ranging from 0.1 meters to 3.1 meters (Figure 39). The lateral distance and standoff distance were held constant at 0 meters and 3.5 meters respectively. The region in which the mach stem is formed is clearly visible and results in a HIC_{15} value that is well above the injury threshold of 700.

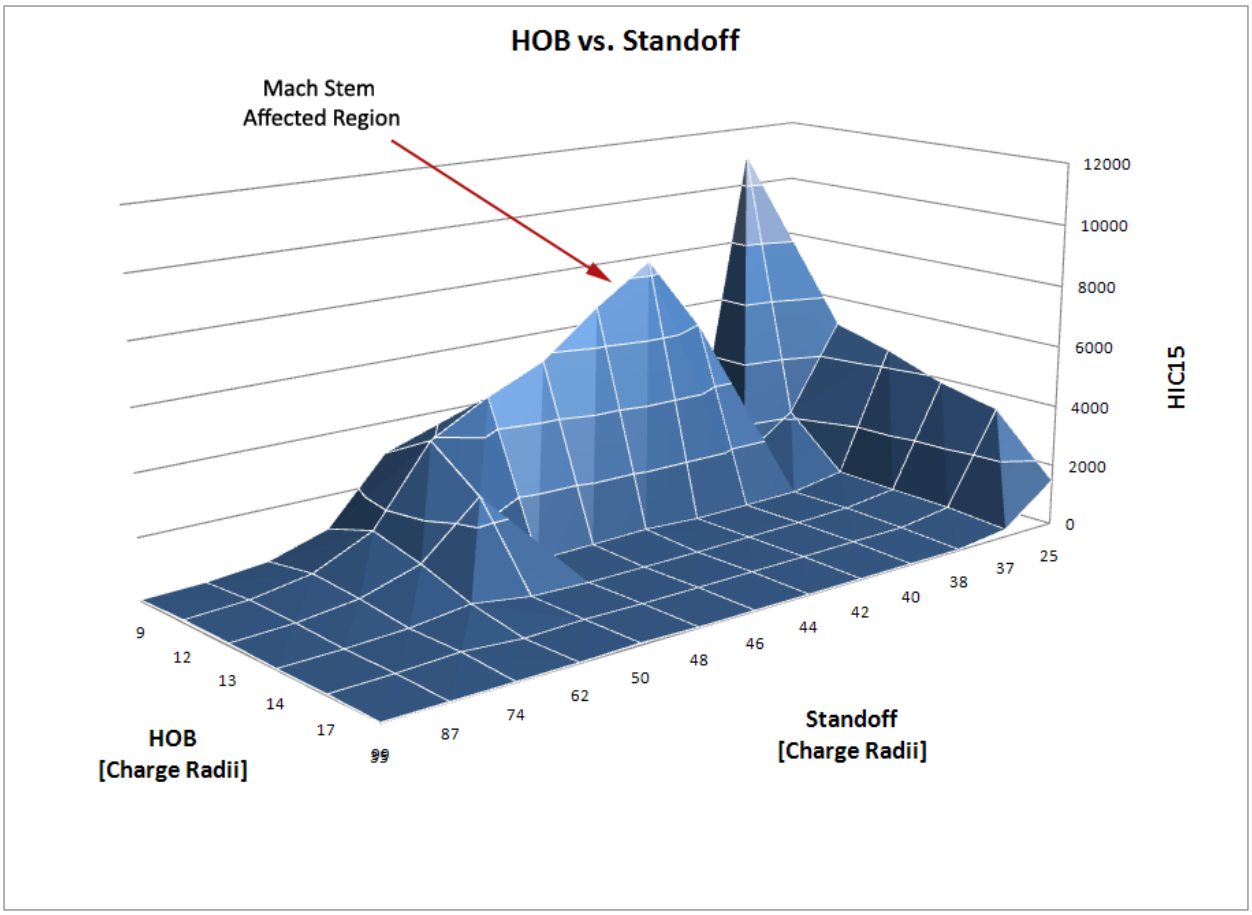

Figure 40: Surface Plot: HOB vs. Standoff

When plotted against one another, the HOB and standoff distance showed a distinct second peak where the mach stem begins to influence the results (Figure 40). The region of mach stem influence for standoff distances between 40 and 60 charge radii could only be seen for HOBs less than 14 charge radii.

7 DETAILED SAGITTAL HEAD MODEL DEVELOPMENT

While the GEBOD can provide kinematic response data for the overall head, it is composed of rigid bodies which do not allow for the prediction of tissue level response. Since some of the proposed criteria for head injury involve strains and rotational displacements of the brain itself, a more detailed head model was required to isolate these phenomena from the gross motion of the entire head. While numerical models of the entire head have been created for car crash scenarios to examine the effects on the brain, these models do not have a high enough mesh resolution to allow for the accurate propagation of the shockwave front for response prediction. The element size for blast loading to human tissue should be on the order of approximately 1 mm or smaller [26]. A 3-D human head model made of elements this small would be very expensive computationally, and simulations would take a very long time to complete.

A less computationally expensive model is a quasi two-dimensional model, which uses a vertical slice of the head that is only a few elements wide at the mid-sagittal plane of the human body. All the elements in the model are constrained from moving laterally outside of this plane. Similar models have been developed in the axial plane for the thorax as well as the head [26][24]. In order to test the protective aspects of the helmet, the sagittal plane was considered to be more ideal since a cross section of the helmet would be able to maintain some structural rigidity and provide a protective barrier over more of the outer surface of the head model.

The main benefit of the two-dimensional model over a full three-dimensional one is that the smaller volume of the two-dimensional model allows for much smaller elements to be used while at the same time allowing for feasible simulation times. The trade-off for this is the loss of any

three dimensional effects such as those that may be encountered in the cerebral spinal fluid, wave interaction effects caused by the wavefront wrapping around the sides of the head, or shaping of the wave due to skull curvature in the transverse plane.

7.1 SAGITTAL HEAD MODEL GEOMETRY

The geometry for the sagittal head model was obtained from the Visible Human Project (VHP) using the AnatQuest Cut-Away Viewer [93] (Figure 41) which provides anatomical geometry for a 50^{th} percentile male. The VHP is a set of 1871 cross-sectional images through the body at 1mm increments along the longitudinal axis. The images were sized so that each pixel represented 0.33 mm x 0.33 mm to allow for accurate translation into numerical or CAD models. The sagittal image used was converted by recording the x-y coordinates of various points on the surface of the geometry of interest and then using that point data in a CAD program to create the geometry.

Figure 41: Visible Human Project geometry at mid-sagittal plane

For the sagittal head model, some of the neck was included in the geometry since it provided some measure of damping to the gross motion of the head and could also act as an anchor point without affecting the head motion.

Surfaces were created using Altair Hypermesh® (Figure 42) and a surface mesh with elements approximately 1 mm x 1 mm was created. To create this mesh the surfaces of each part were subdivided into shapes that were roughly square to make it easier to form a mesh using only

square elements. Triangular elements (or Tetrahedral when extruded into 3D solid elements) were not used since they perform poorly and can cause numerical instabilities in scenarios with plasticity or nearly incompressible materials, such those involving blast loading. These severe locking problems of tetrahedral elements force the use of hexahedral elements for most nonlinear problems [94].

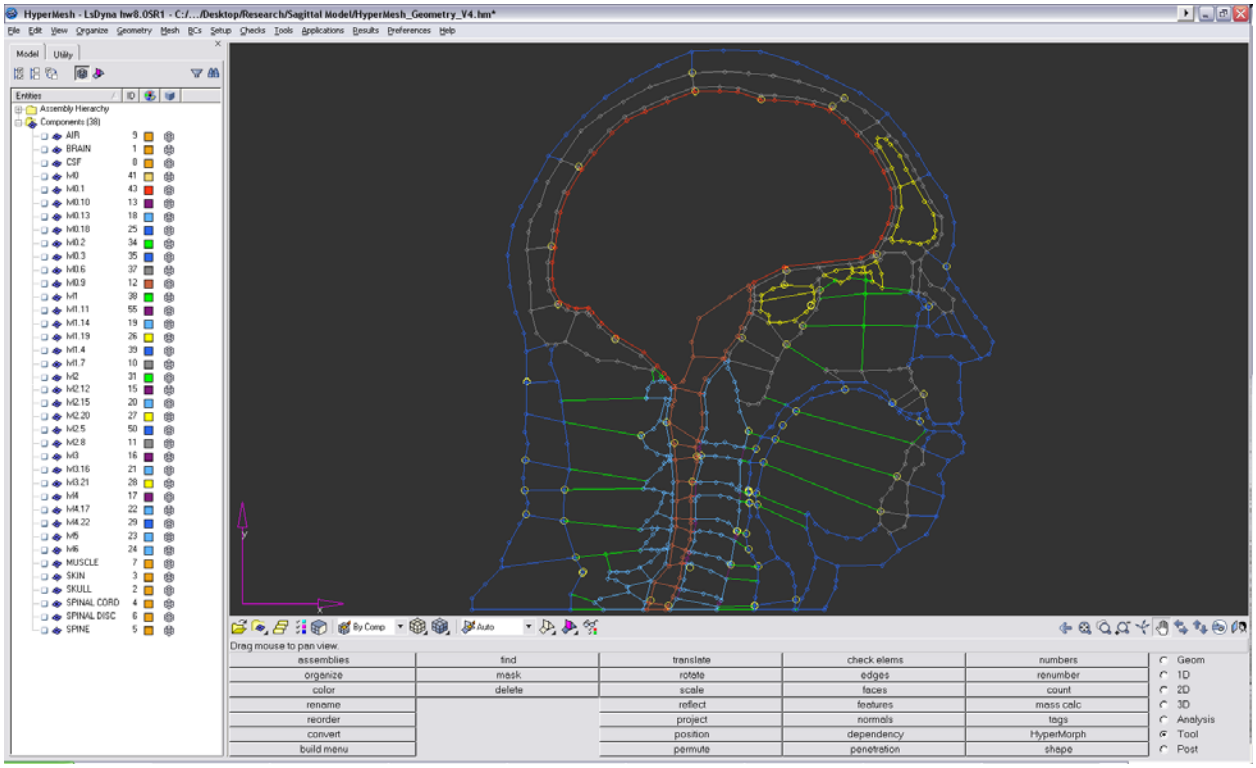

Figure 42: Sagittal Head Model Geometry in Altair Hypermesh®

The two-dimensional mesh was extruded to create a layer of three-dimensional hexahedral solid elements. Since the entire model was constrained to only allow movement within the sagittal plane, only one layer of elements was required. To avoid numerical instabilities due to contact between all of the various components, the final step in the geometry creation was to merge nodes on shared surfaces in the model, essentially joining all the components together and

eliminating the need to define contact. This was also done on a previously developed model of the torso to increase computational efficiency; however, it is only valid if there is little relative motion between parts. It has also been found that the contact algorithms in FE programs are generally poor at accurately transmitting forces when very soft materials contact hard materials with different bulk moduli [26].

The node corresponding to the Centre of Gravity (CG) of the finalized geometry (Figure 43) was found by calculating the spatial coordinates using the relationship of the CG for a 50^{th} percentile male: 11.15 cm from the top of the head and 7.98 cm from the back of the head [95]. The acceleration was output for this node in order to compare the kinematic response of the sagittal head model to that of the GEBOD under the same numerical loading conditions.

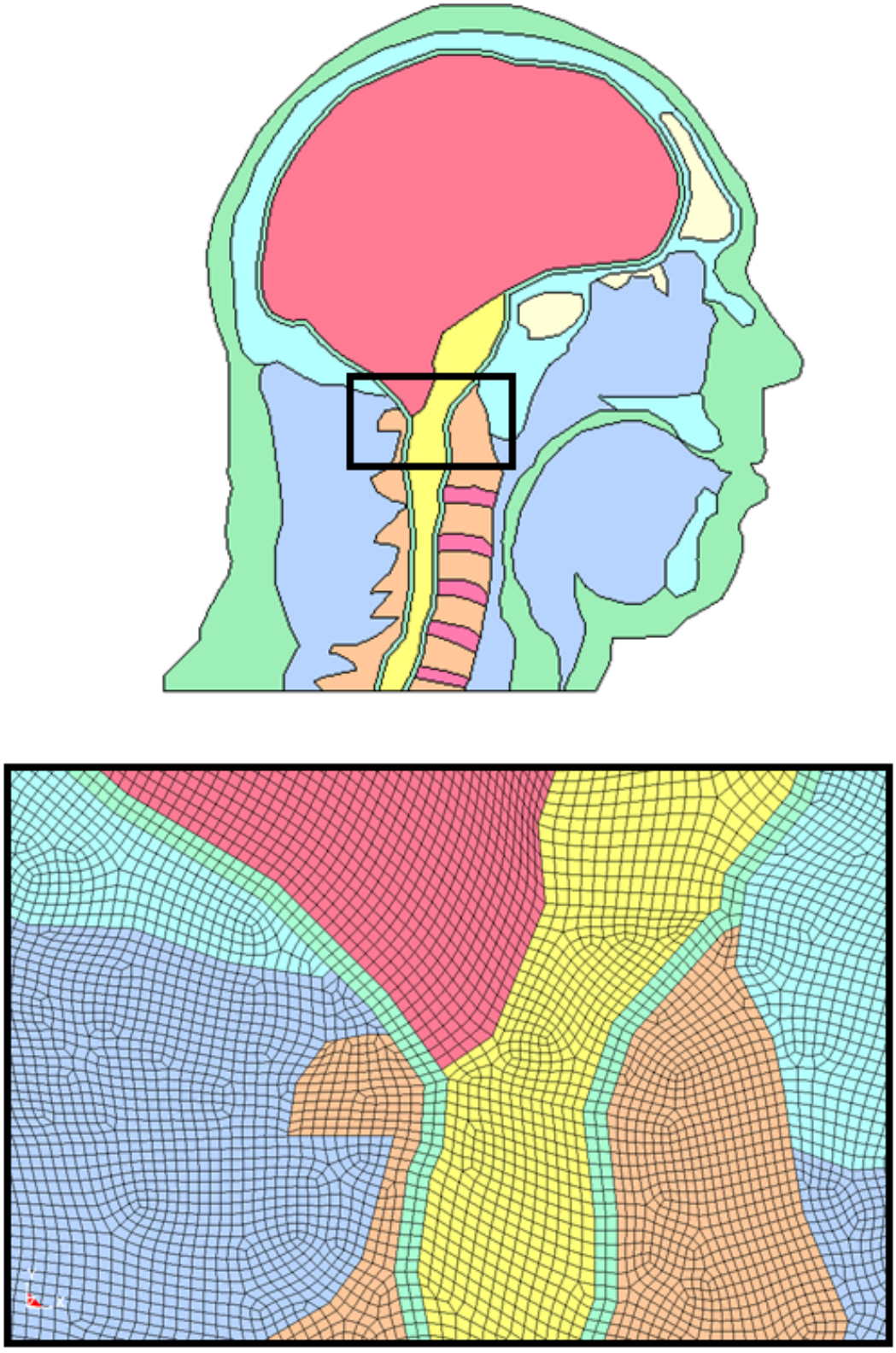

Figure 43: Finalized Numerical Sagittal Head Model Geometry

To determine if the mesh used in the sagittal head model was fine enough to provide accurate response a grid convergence study was conducted using a Richardson extrapolation to calculate the GCI. For this study, meshes sized at 2 mm, 1 mm, and 0.5 mm were subjected to the same loading conditions (Figure 44) and the peak acceleration response of their respective CGs were compared. Since the mesh sizes were halved for each refinement step, r = 2 for all of the calculations. Peak acceleration was used as the response metric since it is highly sensative to small variations and the accleration traces were used to calculate the HIC_{15} values for the protection studies.

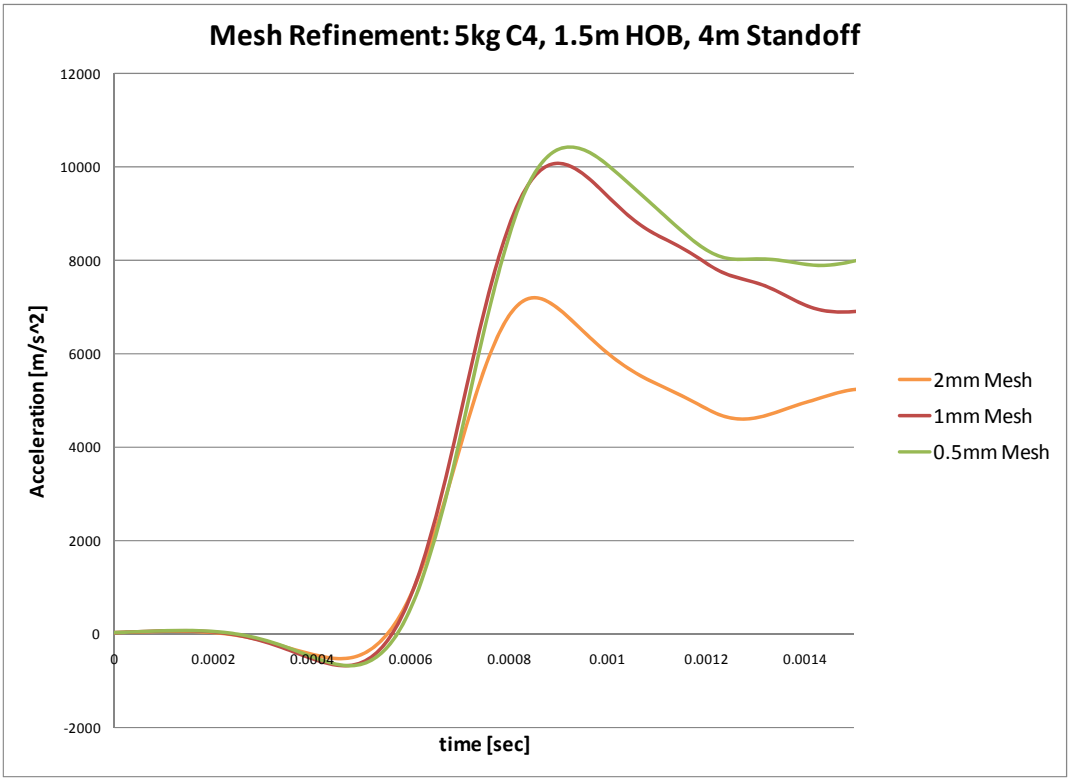

Figure 44: Mesh Refinement Study

The GCI was calculated for 5kg C4 detonations at 3 different standoff distances (Table 6) for a 95% confidence level of the error estimate (F_s = 1.25). The estimated relative error between the

meshes was less than 2%. Using Equation 2.11 (see section 2.5), the values for r^pGCI_{12} and GCI_{23} were approximately equal, thus satisfying the equation and indicating that asymptotic convergence had been achieved. For all future simulations involving the sagittal head model, the 1mm mesh was used.

Table 6: GCI Calculation Results

Mesh	Peak Acceleration		
	3.0m Standoff	3.5m Standoff	4.0m Standoff
2mm	7203.14	4380.26	3097.42
1mm	10071.7	6621.36	4788.54
0.5mm	13719.2	9462.49	6002.11
GCI_{12}	1.22 %	1.40 %	0.64 %
GCI_{23}	1.67 %	2.00 %	0.81 %
r^pGCI_{12}	***1.56%***	***1.80 %***	***0.89 %***

7.2 SAGITTAL HEAD MODEL MATERIAL PROPERTIES

The second major component to a numerical model is the characterization of the component response to loading. This is done by assigning constitutive material models and properties to the various components. These models can range from simple pure elastic response, to complex models such as those for low density foams which incorporate densification and strain rate effects.

The combined tissues of the brain was modeled using a simple viscoelastic material model (Equation 7.1) which had been compared against experimental data and deemed to be suitable for use in modeling the brain as a homogenous continuum (no differentiation was made

between white and grey matter) [96]. The parameters for the model were the same as those used in a full three-dimensional model developed by the University of Strasbourg [97].

$$G(t) = G_\infty + (G_0 - G_\infty)Exp(-\beta t) \quad \textbf{(Equation 7.1)}$$

G_0 = 4.9E-2 MPa

G_∞ = 1.62E-2 MPa

β = 145 sec^{-1}

Material models for the skull, skin, and muscle were taken from the axial model of the torso developed previously at the University of Waterloo [24] which were also used in the axial model of the head. The models and their respective coefficients are shown below (Table 7). To simplify the model, simple elastic material models were used where tissues were not expected to fail or demonstrate significant non-linear behavior (the skull, vertebrae, vertebral discs and skin). While the properties of bone in the skull and vertebrae are different, both were assigned the same constitutive material model. For the sagittal head model the skull is more important to the overall response while the spine only provides some structural support to the model.

Table 7: Coefficients for Constitutive Material Models

PART	Material Model	Density [kg/m^3]	Poisson's Ratio	Young's Modulus [Pa]	Bulk Modulus [Pa]	G_0 [Pa]	G_I [Pa]	β [s^{-1}]
Brain/Spinal Cord	Simple Viscoelastic	1050			$2.2x10^9$	49000	16200	145
Skull/ Vertebrae	Simple Elastic	1561	0.379	$7.92x10^9$				
Skin	Simple Elastic	1200	0.42	$1.7x10^9$				
Vertebral Discs [98]	Simple Elastic	1040	0.40	$3.4x10^6$				
Muscle	Simple Rubber	1050	0.1		$2.2x10^9$			
CSF	Simple Elastic Fluid	1040			$2.2x10^9$			

Simplified material models were used to allow for low computational costs while at the same time providing a reasonable response to loading. Since the sagittal head model was planar, many of the effects seen by using a more complex model would be disregarded by the symmetry condition imposed on the elements.

The air pockets within the head (sinuses and nasal passages) were modeled as an ideal gas using the single material ALE element formulation to allow for large deformation (compression) of the gases. When the ambient air surrounding the head was modeled to study the wave interactions, the air within the head was replaced with the ambient ALE material to prevent numerical errors that occur when multiple ALE element formulations are present in the same model.

A strain-rate dependant, simplified rubber material model was used for the muscle tissue. It is defined by a series of uniaxial stress-strain curves at different strain rates taken from various literature sources [99]. For the other model parameters, the bulk modulus of water, and a density of 1050 kg/m^3 [100] were used. The curves utilized to characterize the soft muscle tissue material response (Figure 45) show different stress-strain response in compression for varying strain rates but not in tension. This is not a large concern, since the blast wave will load the tissues in compression.

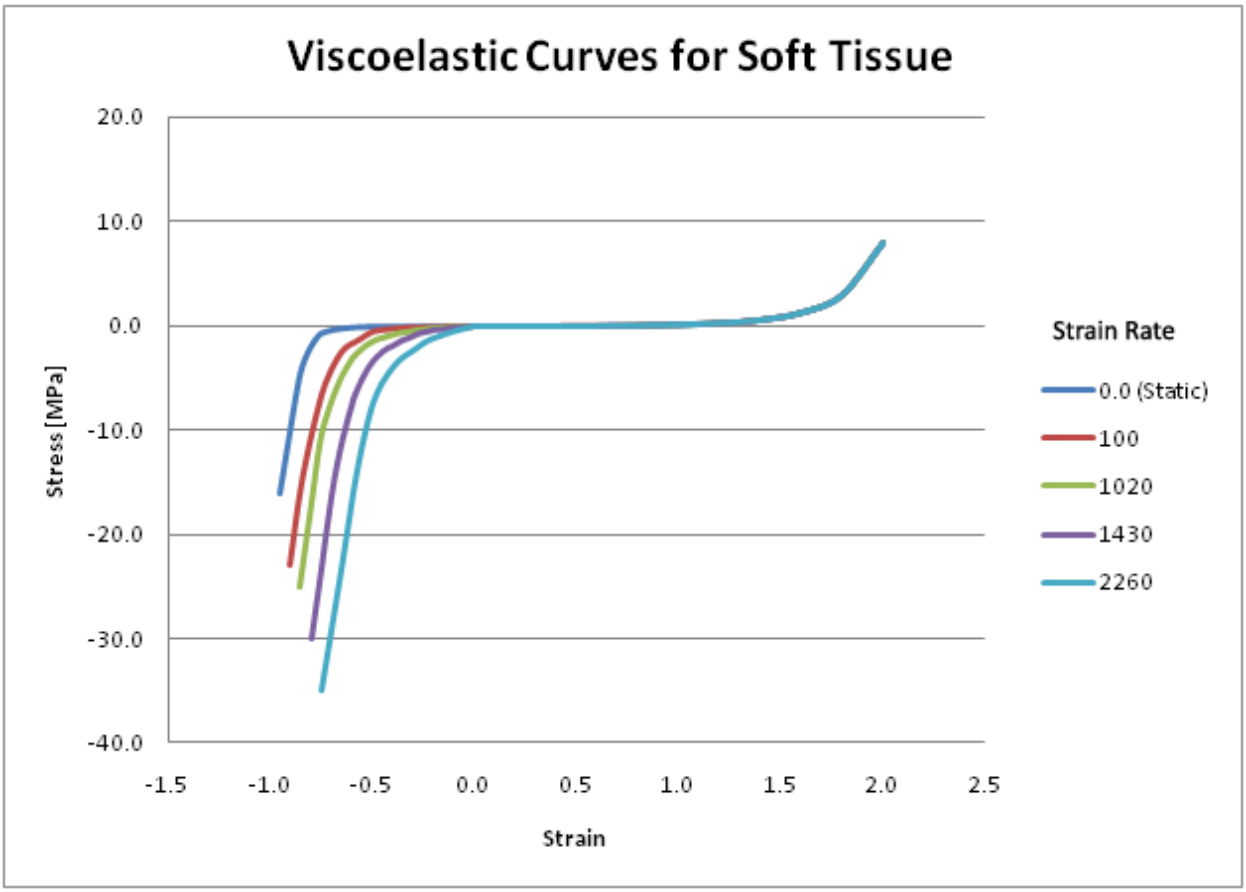

Figure 45: Viscoelastic Curves for Muscle Tissue [26]

7.3 SAGITTAL HEAD MODEL VALIDATION

Validation is the process of determining the degree to which a model is an accurate representation of the real world from the perspective of the intended uses of the model [27]. For the validation of the sagittal head model, the response feature of interest was the resultant acceleration of the centre of gravity of the head. This was directly compared to the GEBOD results and DRDC experiments to determine if the sagittal head model was behaving in an appropriate manner.

The sagittal head model was subjected to the same blast loading conditions as the GEBOD corresponding to the DRDC experimental tests presented in section 2.7. The initial results showed oscillations occurring in the model that were skewing the resulting accelerations higher (Figure 46). These oscillations were a result of the stress waves passing through the model. Rigid bodies, such as those that compose the GEBOD, do not transmit waves [16] and thus would not show these oscillations. In order to compare the sagittal head model response to that of the GEBOD, these oscillations needed to be damped out of the model.

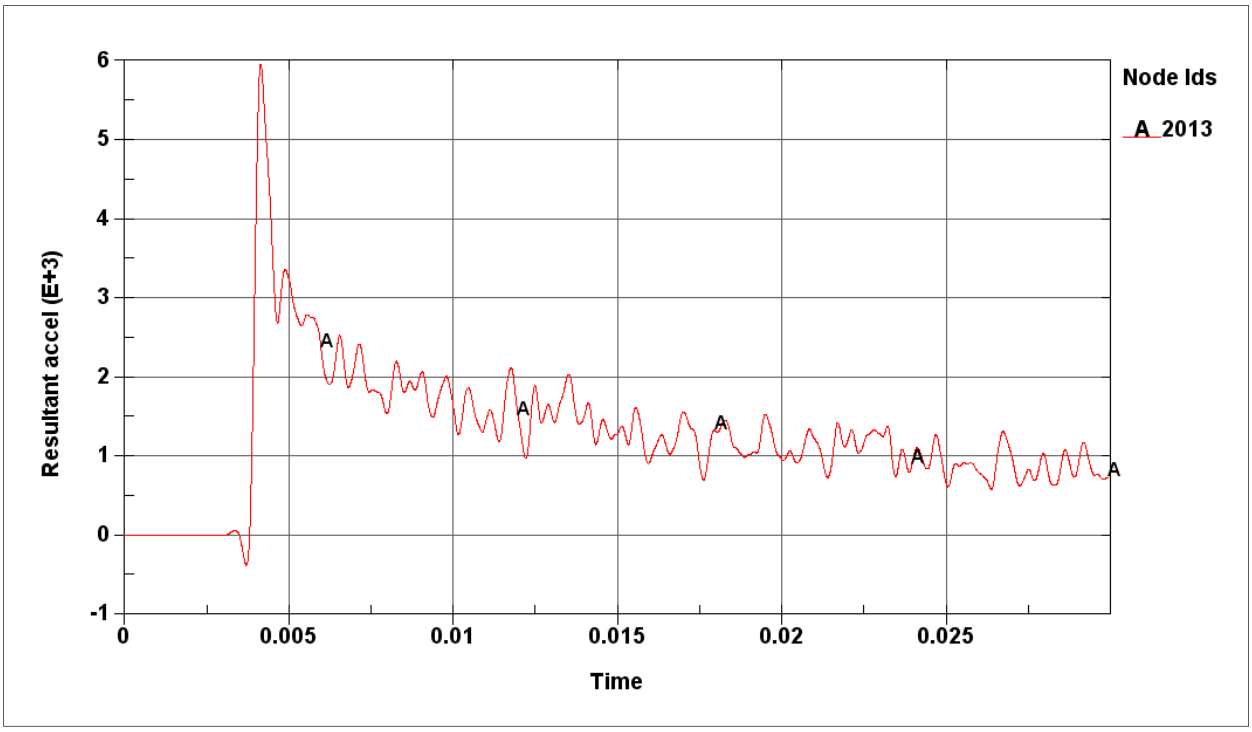

Figure 46: Undamped Sagittal Model Response

To eliminate these oscillations a Fast Fourier Transform (FFT) was performed on the data which transformed the data into components of different frequencies (these components resemble sine functions) which when added together equaled the original data trace. By using this transformation, the critical frequency, ω, was identified and extracted (Figure 47).

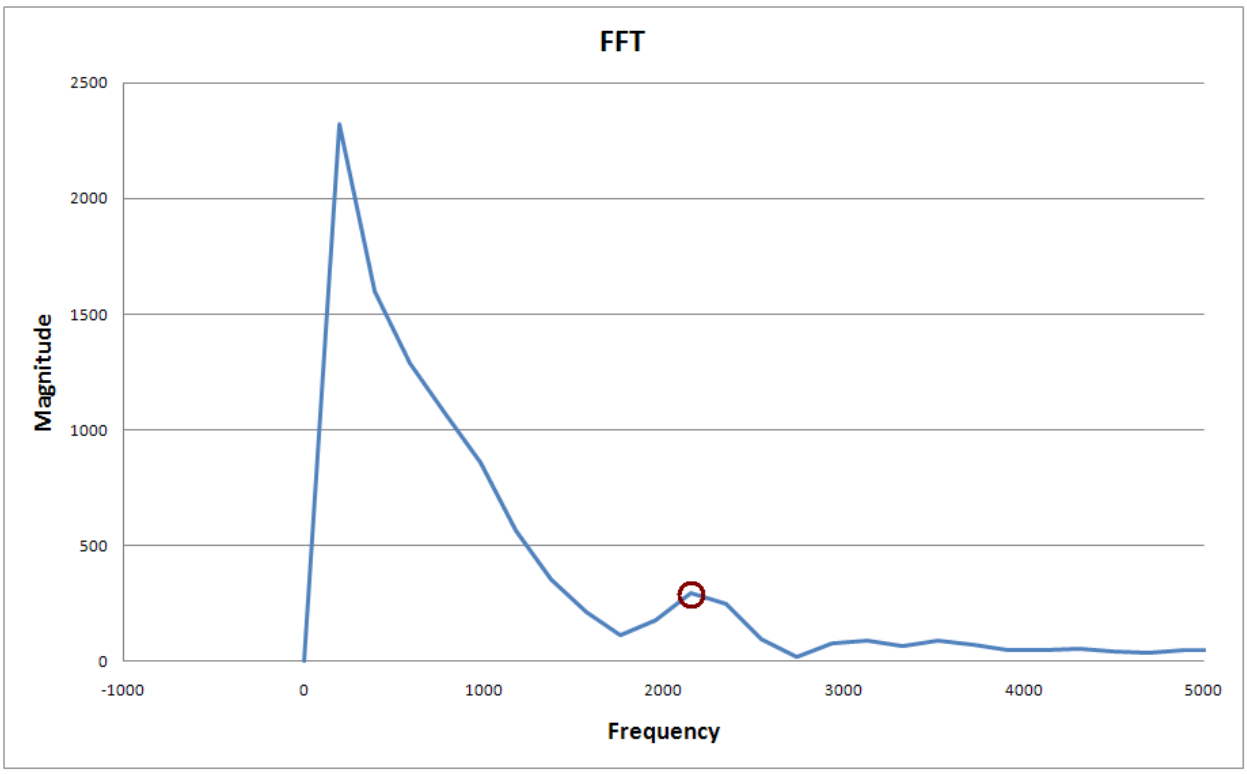

Figure 47: FFT to determine natural frequency

From the FFT plot, the frequency corresponding to the second peak was used to calculate a damping coefficient of 0.36 for the frequency range 0-1650 Hz. When this damping was applied to the model using the *DAMPING_FREQUENCY_RANGE keyword, the oscillations were sufficiently damped and the acceleration traces at the CG of the sagittal head model correlated quite well with those of the GEBOD under the same load conditions (Figure 48).

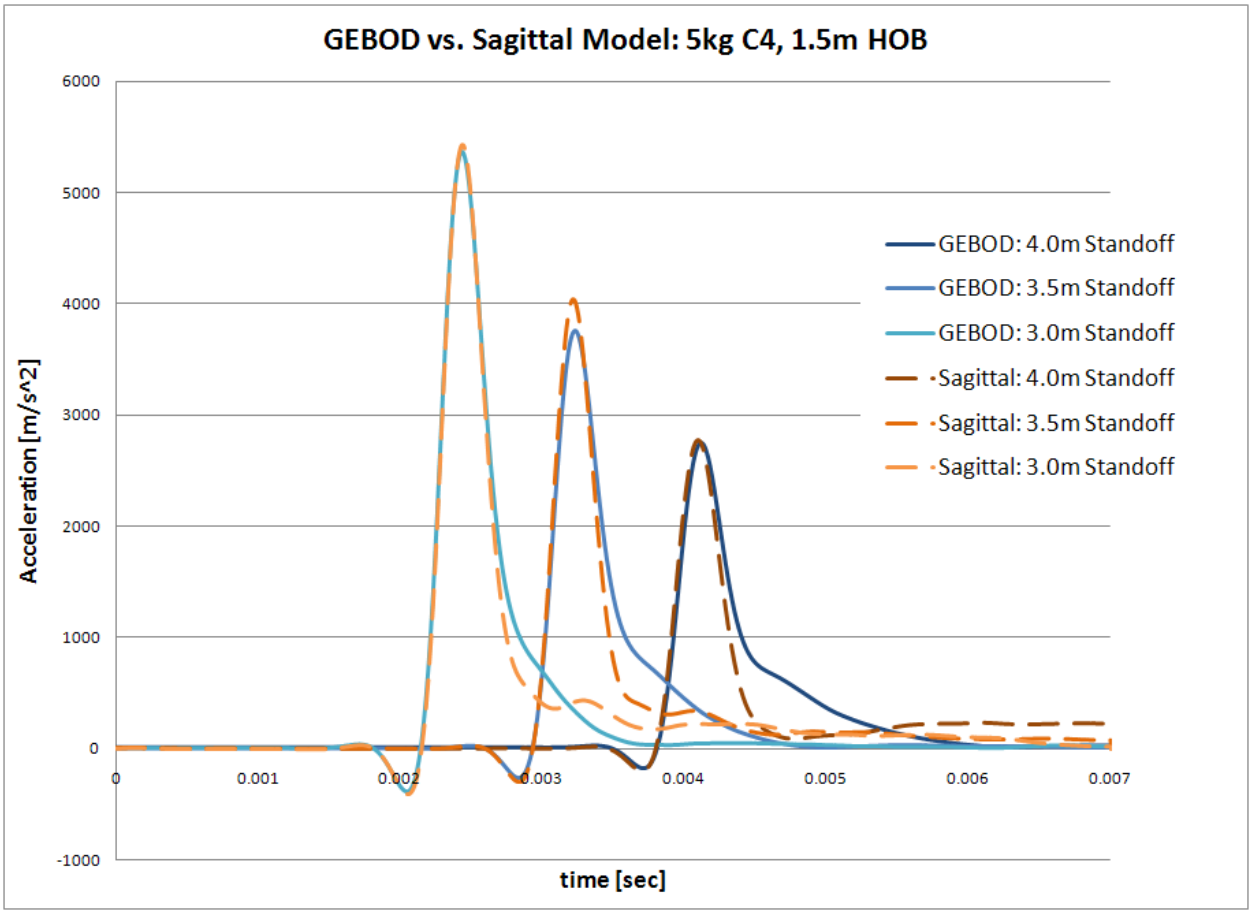

Figure 48: GEBOD vs. Sagittal Model Response

While validation against the kinematic response of the GEBOD and HIII used in the DRDC experiments was sufficient when the numerical implementation of CONWEP was used to apply blast loading, it was not sufficient for assessing the pressure fields produced or wave interactions around the head. In order to model the wave interaction, the ambient air surrounding the head was modeled using an ALE element formulation which allowed a pressure wave to propagate through the air and interact with the sagittal head model (Figure 49).

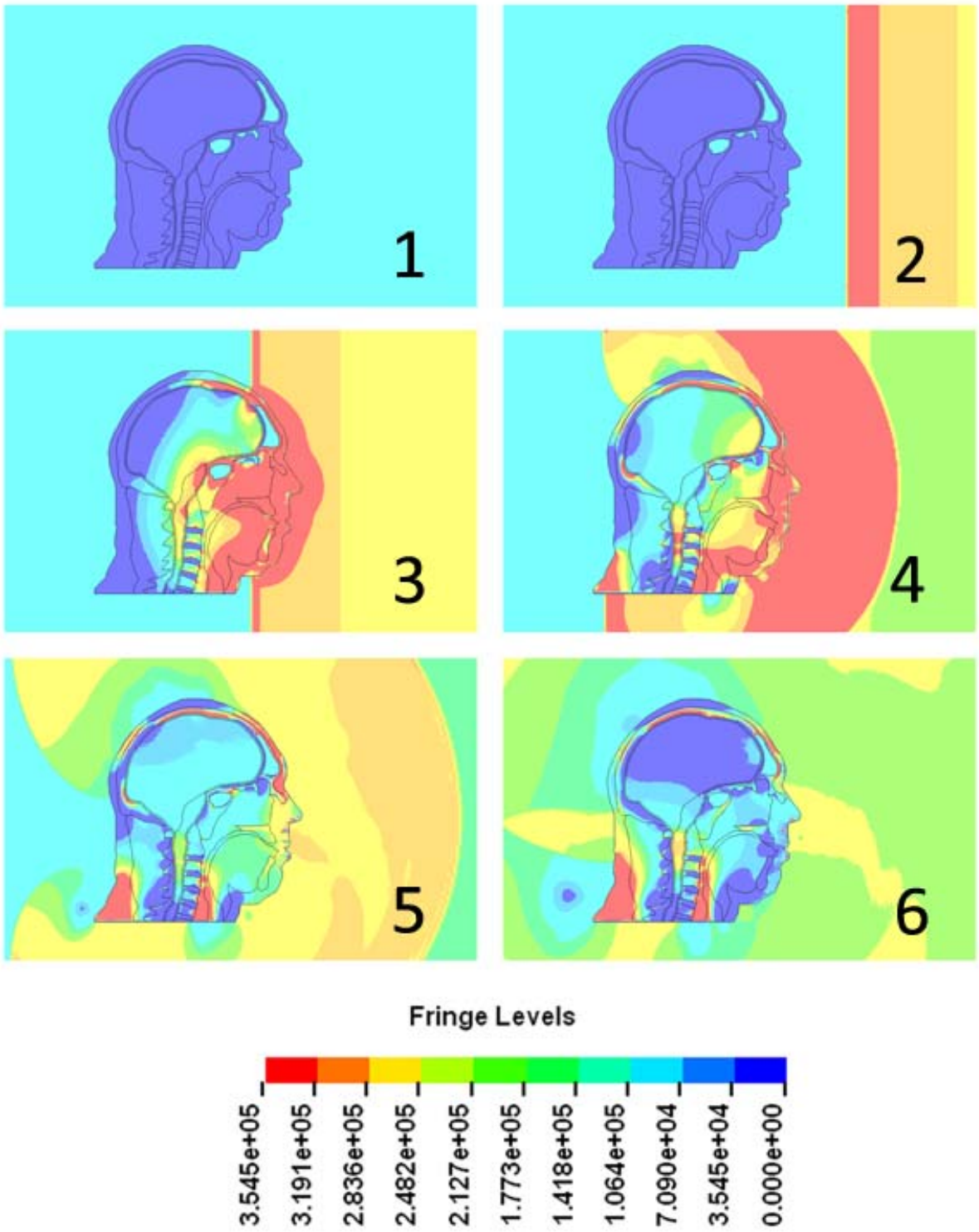

Figure 49: Sagittal ALE Blast Loading

To ensure that no reflections due to boundary conditions on the ambient air elements affected the response during the blast loading, the ALE mesh needed to be much larger than the sagittal head model [26] (Figure 50). Since the outer elements only exist to prevent the reflection of the blast wave from occurring too soon in the simulation, they were made larger to decrease the computational cost of the model.

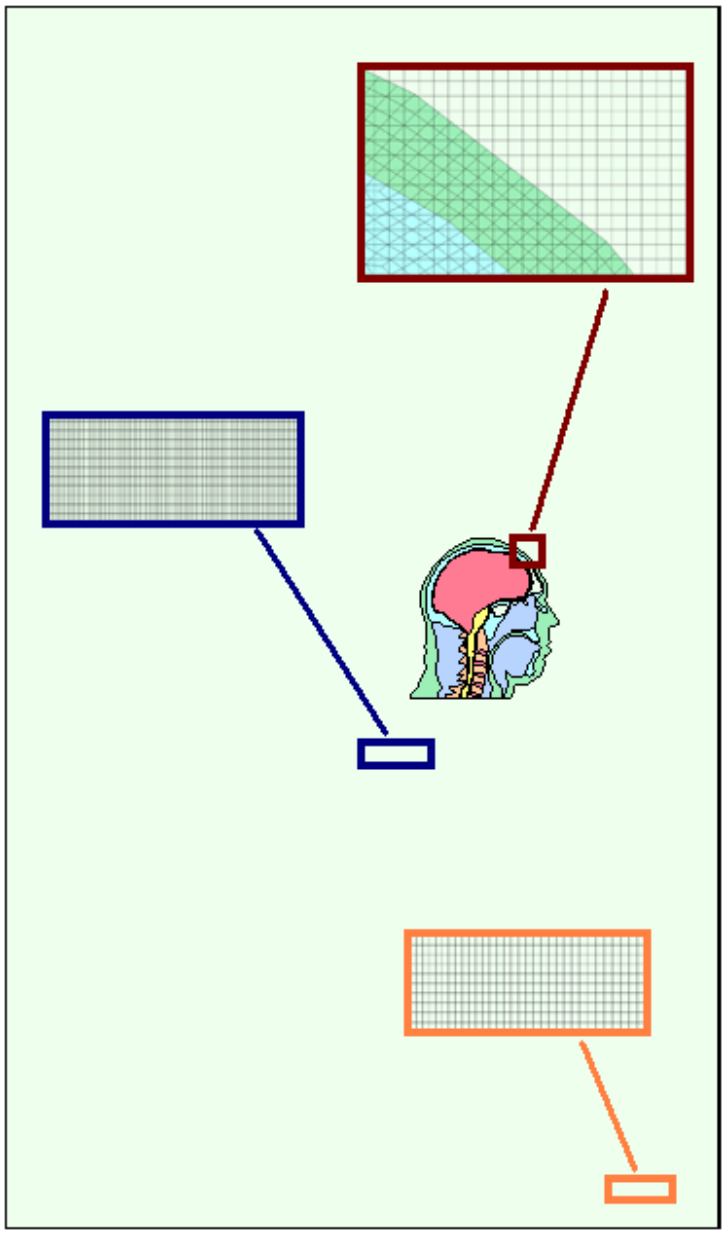

Figure 50: ALE Mesh with embedded sagittal head model

The elements at the centre of the mesh where the sagittal head model was located were on the order of 1mm in size, the same as the sagittal head model, while elements towards the outer edges were on the order of 10mm. This same method of element size bias has been used previously for the torso model [26] as well as many other ALE simulations where large surrounding meshes are required. The width of the ALE mesh was set so that the reflected wave would not affect the results over the simulated time.

To validate the ALE model, the embedded sagittal head model was subjected to the same loading conditions as the DRDC experiments (Figure 51). The acceleration traces of the CG of the sagittal head model in the ALE environment showed two peaks. The first peak in the plots below was a result of the pressure wave moving through the head while the second peak was from the gross motion of the head.

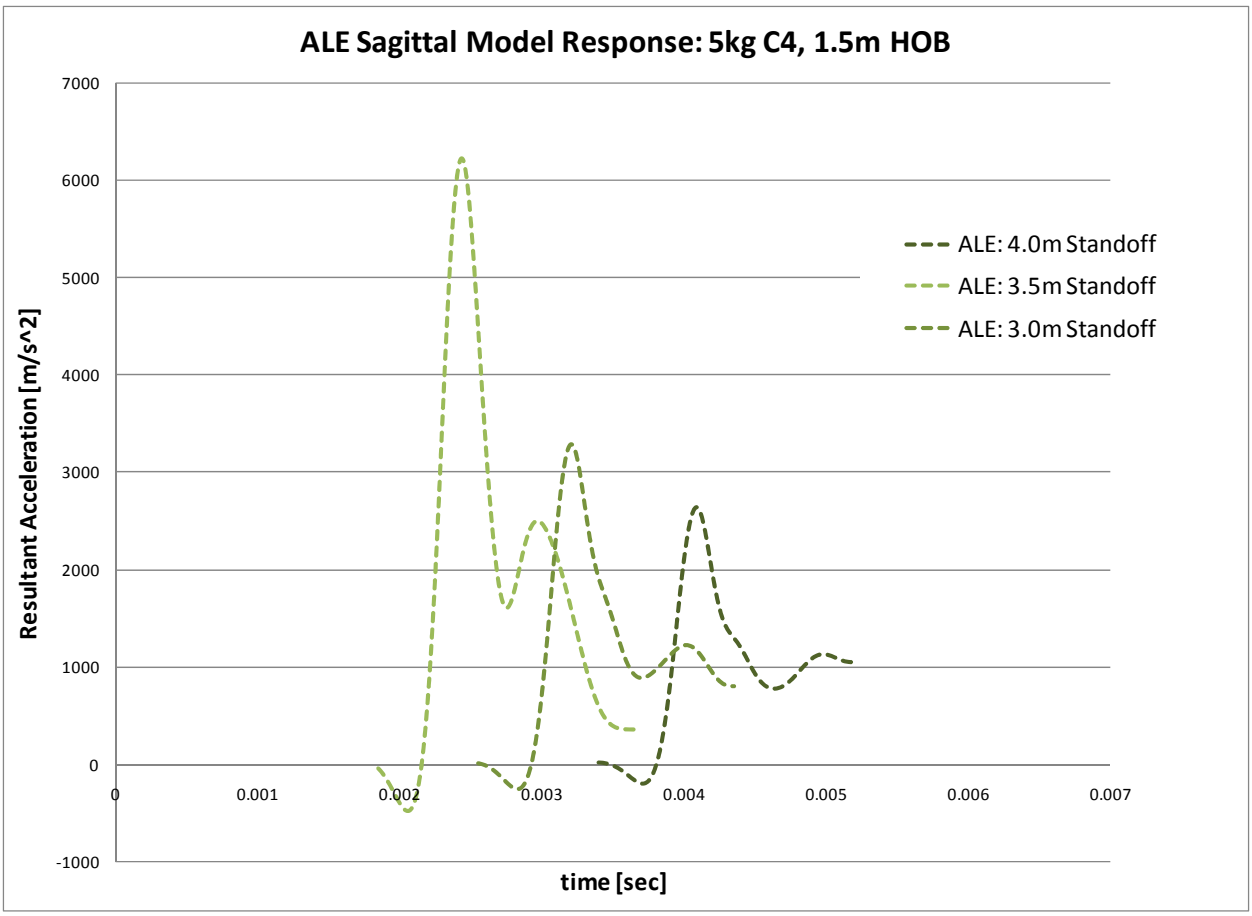

Figure 51: ALE Sagittal Model Response

The peak linear acceleration values of the CG for the ALE model were compared to those of the non-ALE sagittal head model, the GEBOD, and the DRDC experiments (error bars indicate the range of the data) (Figure 52). All of the numerical models correlated well with the DRDC values for the 3 meter and 3.5 meter standoff distances, but all were over-predictive for the 4 meter standoff.

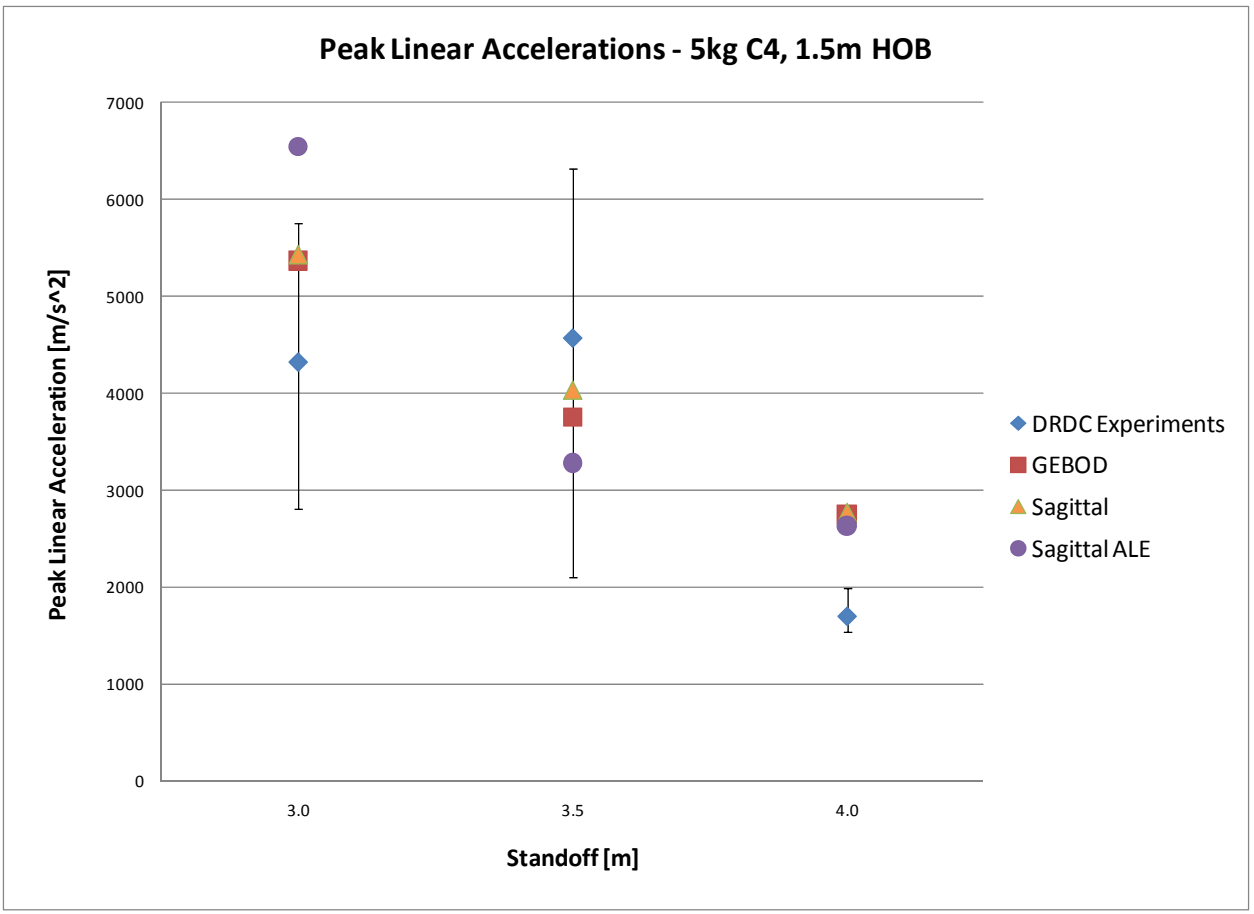

Figure 52: Comparison of Peak Linear Accelerations

All of the numerical models had very similar peak linear acceleration values at the 4m standoff; however, the peak linear acceleration of the ALE sagittal head model was higher than both the GEBOD and the non-ALE sagittal head model at the 3m standoff.

8 HEAD BLAST PROTECTION EVALUATION

People can be protected from blast effects if they are behind rigid walls or within enclosures and insulated from the blast. For example, rigid enclosures have been shown to reduce injury in rabbits exposed to blast waves [101]. Soft materials on their own do not offer much protection from blast and may increase the injury in some cases [80]. The most common form of head protection is a rigid helmet. Historically military helmet design has focused on protecting against ballistic threats and ensuring proper fit via suspension systems. Blast protection has not factored into any helmet design up to and including the PASGT [75]; however, it may be possible to apply blast protection principles from torso armour to helmet design.

8.1 PRELIMINARY PROTECTION INVESTIGATION

Further validation was performed for the addition of a helmet to the sagittal head model in the ALE environment. A model of the PASGT helmet taken at the mid-sagittal plane was added to the model with an air gap left between the helmet and head to simulate the strap suspension system. Simulations were conducted for both a rigidly embedded (constrained in all directions) sagittal head model and a deformable sagittal head model to see how the pressure flow field developed in the air gap. This simulation was then compared to a similar study [102] done with a full 3D head and torso model embedded in a CFD calculated blast flow field at various times during the blast wave interaction (Figure 53). The study used a 1.5kg charge of C4 with a standoff distance of 3 meters. The lateral distance was 0 meters and the HOB was set to that of the center of the head.

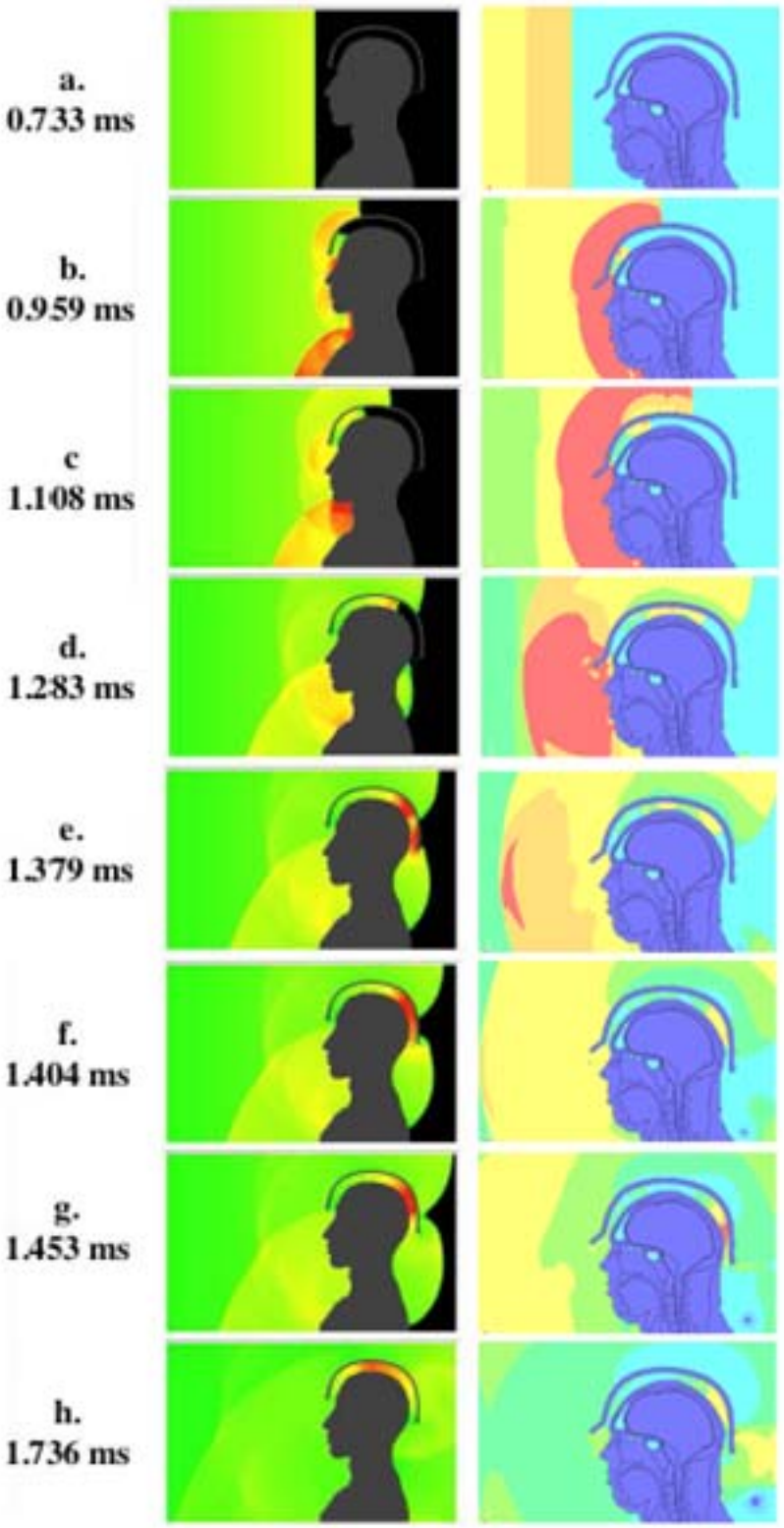

Figure 53: Pressure field beneath helmet - ALE Sagittal Model vs. Mott et al

The pressure fields at the rear of the head were compared (Figure 54) and it was shown that the interaction due to the wave "wrapping" around the side of the head and having a deformable model do have a significant effect on the pressure field and that the fields predicted by the sagittal model were slightly over-predictive.

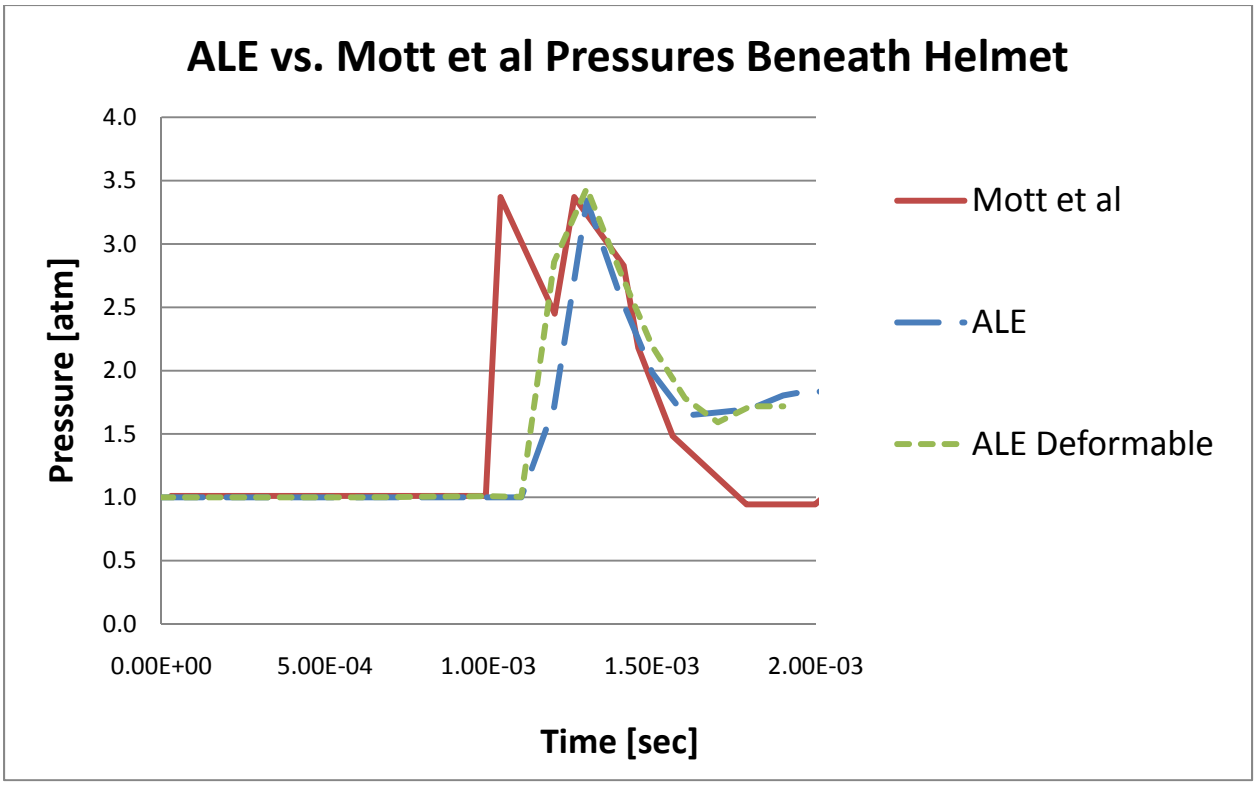

Figure 54: ALE vs. Mott et al Pressure Traces

In order to determine the protective properties of a helmet against blast injury, the model of the PASGT helmet taken at the mid-sagittal plane with a layer of foam padding was added to the sagittal head model (Figure 55) and subjected to the same blast loading. The mesh size for the foam and helmet were matched to the sagittal head model and the contact between the helmet and head was defined using a contact algorithm to allow for the helmet to impact or slide on the head. The foam used in this study was compressible low density foam while the helmet shell was modeled as Kevlar 29 using an anisotropic constitutive material model.

LS-DYNA has many numerical implementations of constitutive material models for compressible foams. Soft, open cell, polyurethane foams lend well to the MAT_LOW_DENSITY_FOAM material model while Expanded Ploystyrene (EPS) foams are more suited for MAT_MODIFIED_CRUSHABLE_FOAM which allows for rate dependency, damage calculations, and also handles the small amount of elastic recovery that would occur with this material [103].

Figure 55: Sagittal Head Model with Helmet

8.2 FOAM PADDING STUDY

A factorial study was undertaken to investigate the properties of a foam insert between the helmet and the head that would reduce the accelerations seen by the head, and therefore reduce injury based on the HIC. This study examined the effect of five individual variables in the foam numerical material model and the interaction effects between them. The variables considered were Young's Modulus, density, hysteretic unloading factor, damping factor and scale factor for the stress-strain curve. This latter parameter defines the plateau stress and densification behavior. The hysteretic unload factor controls the energy dissipation over the course of the foam compression and recovery; the default value of 1 corresponded to no energy dissipation.

The study conducted utilized a fractional factorial experiment design in which high and low values were chosen for each variable (

Table 8) and then simulations were conducted for various combinations (Table 9) and a response variable was measured. Since it was used as the response variable for the GEBOD study, HIC_{15} was used as the response variable in this study. To minimize the number of experiments required, a design generator was used; this generator determines which value (high or low) should be used for a variable based on a combination of the other four and reduces the number of required simulations by half.

Table 8: Levels for Factorial Experiment

	Variable	-	+
A	Density [kg/m^3]	40	960
B	σ-ε Scale Factor	0.1	10
C	Hysteretic Unload Factor	0	1
D	Damping Factor	0	0.9
E	Young's Modulus [Pa]	3.20E+05	3.20E+07

Design Generator: E = ABCD

Table 9: Factorial Experiment Design and Response

Trial	A	B	C	D	E	HIC_{15}	Max ε_1	Max Pressure [Pa]
1	-	-	-	-	+	221.5	0.947	857970
2	+	-	-	-	-	370.8	0.707	865221
3	-	+	-	-	-	128.5	0.637	54751
4	+	+	-	-	+	144.8	0.407	543178
5	-	-	+	-	-	188.9	0.877	817241
6	+	-	+	-	+	287.2	1.087	894290
7	-	+	+	-	+	108.5	1.968	548674
8	+	+	+	-	-	134.2	0.405	552856
9	-	-	-	+	-	102.8	3.477	519154
10	+	-	-	+	+	179.6	4.333	366399
11	-	+	-	+	+	205.6	1.206	758584
12	+	+	-	+	-	303.3	1.324	520748
13	-	-	+	+	+	105.3	0.736	528022
14	+	-	+	+	-	187.5	3.891	367465
15	-	+	+	+	-	204.4	0.941	745427
16	+	+	+	+	+	378.8	1.299	523051

Initially, sixteen simulations were undertaken and the results were evaluated using HIC_{15}. The maximum principal strain and maximum intracranial pressure were also recorded. The main and interaction effects were calculated (Equation 8.1) and plotted on a normal probability plot to determine which of them were significant. Only two factor interactions were considered because the design generator resulted in two factor interactions being confounded with three factor interactions (ie: interaction AB is equal to interaction CDE).

$$Effect = (Average\ HIC_{15}\ for\ "+") - (Average\ HIC_{15}\ for\ "-") \quad \textbf{(Equation 8.1)}$$

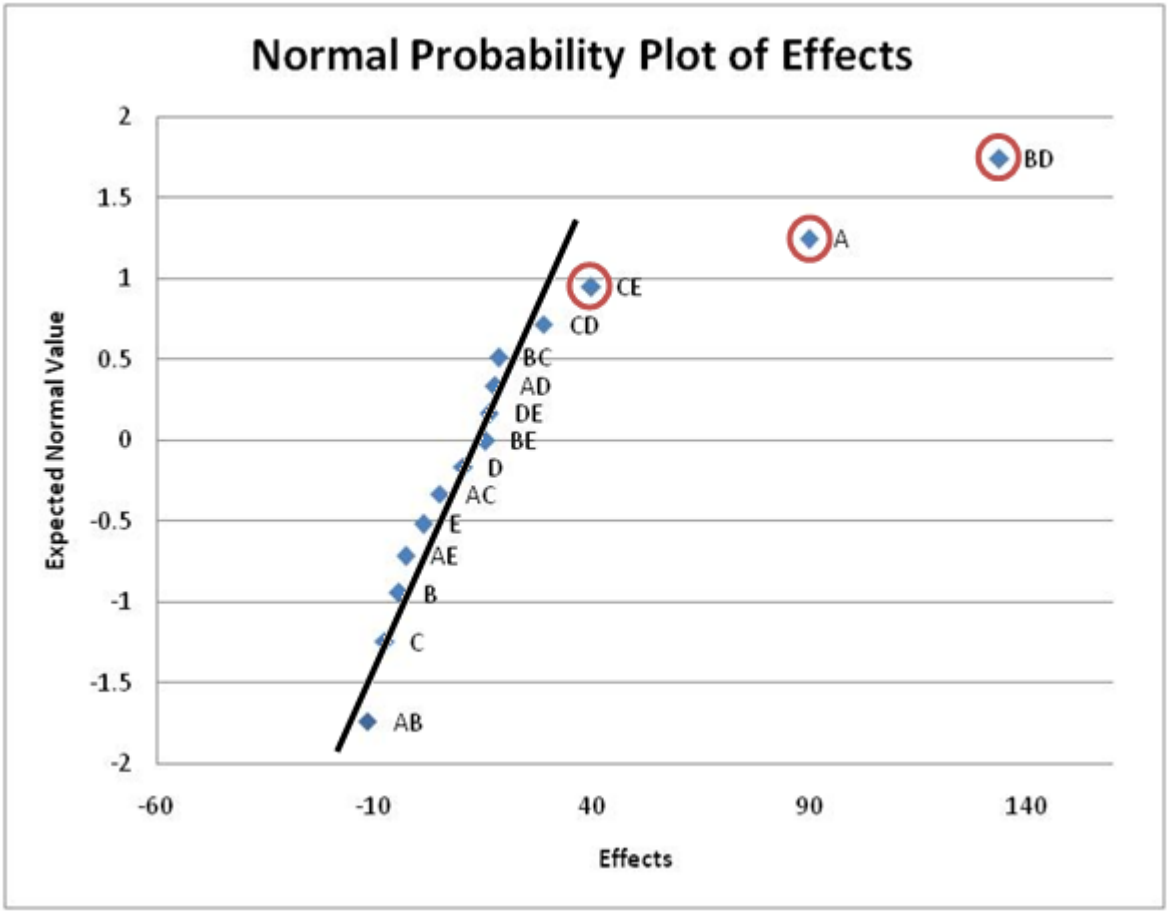

Figure 56: Normal Probability Plot of Effects

A normal distribution can be converted to a normal probability by adjusting the vertical scale so that the values represent various percentages of the cumulative distribution. This method was used to determine significant effects since a random sample (with roughly normal variation) about a fixed mean will be distributed about zero and would produce a straight line on a normal probability plot, with any significant effects deviating from this straight line [104].

Starting with effects that had a magnitude close to zero, a straight line was constructed through the most points (Figure 56). Based on this plot, the significant effects were density (A); the interaction between the damping factor and the scale factor for the stress-strain curve (BD); and

to a lesser extent, the interaction between Young's Modulus and the hysteretic unload factor (CE).

This type of study assumes that the differences between the + and – values for the variables were linear. To check for quadratic behavior, extra simulations were evaluated to create a Central Composite Design (CCD). Since the high and low values for the all variables were considered to be the absolute maxima and minima, an inscribed CCD approach was used to determine the values for the extra "star points". To determine the star point values, the coded values (-1, +1) were divided by α, a value calculated based on the number of factorial runs (Equation 8.2), to give the coded values for the star points.

$$\alpha = [2^k]^{1/4} \qquad \textbf{(Equation 8.2)}$$

Since the fractional factorial used was a 2^{5-1} design, the value of α was 2. This resulted in coded values of -0.5 and +0.5 to be used for the star points; the center point was also calculated. The new coded variable values and extra trial configurations are shown below (Table 10 and Table 11).

Table 10: Values for extra CCI coded variables

	Variable	-1	-0.5	0	+0.5	+1
A	Density [kg/m^3]	40	270	500	730	960
B	σ-ε Scale Factor	0.1	2.575	5.05	7.525	10
C	Hysteretic Unload Factor	0	0.25	0.5	0.75	1
D	Damping Factor	0	0.225	0.45	0.675	0.9
E	Young's Modulus [Pa]	3.20E5	8.24E6	1.616E7	2.408E7	3.20E7

Table 11: Coded configurations for extra CCI trials

Trial	A	B	C	D	E	HIC_{15}	Max ε_1	Max Pressure [Pa]
17	-0.5	0	0	0	0	103.4	1.204	487558
18	+0.5	0	0	0	0	140.2	0.746	487849
19	0	-0.5	0	0	0	98.8	1.049	474839
20	0	+0.5	0	0	0	133.0	1.661	485418
21	0	0	-0.5	0	0	119.2	0.839	486898
22	0	0	+0.5	0	0	132.0	1.022	486129
23	0	0	0	-0.5	0	100.9	0.908	497684
24	0	0	0	+0.5	0	127.1	1.068	479955
25	0	0	0	0	-0.5	113.4	0.616	488546
26	0	0	0	0	+0.5	110.8	0.896	487185
27	0	0	0	0	0	133.1	1.171	488848

The additional trial runs allowed for the following model (Equation 8.3) to be fit to the data using a goodness of fit test (Equation 8.4) for the HIC_{15} values.

$$\hat{y} = \beta_0 + \beta_1 A + \beta_2 B + \beta_3 C + \beta_4 D + \beta_5 E + \beta_6 AB + \beta_7 AC + \beta_8 AD + \beta_9 AE + \beta_{10} BC + \beta_{11} BD + \beta_{12} BE + \beta_{13} CD + \beta_{14} CE + \beta_{15} DE + \beta_{16} A^2 + \beta_{17} B^2 + \beta_{18} C^2 + \beta_{19} D^2 + \beta_{20} E^2 \quad \textbf{(Equation 8.3)}$$

$$R^2 = 1 - \frac{\sum(y - \hat{y})^2}{\sum(y - \bar{y})^2} \quad \textbf{(Equation 8.4)}$$

Using an iterative approach, the value for each coefficient in the model was calculated such that the value for R^2 was maximized. For the values of the calculated coefficients below, the value of R^2 was 0.992.

β_0	115.437	β_{11}	5.472
β_1	42.603	β_{12}	10.695
β_2	2.133	β_{13}	17.215
β_3	0.284	β_{14}	5.527
β_4	9.478	β_{15}	30.062
β_5	3.204	β_{16}	5.103
β_6	-3.077	β_{17}	45.262
β_7	4.791	β_{18}	-36.148
β_8	11.103	β_{19}	44.708
β_9	6.014	β_{20}	3.558
β_{10}	63.502		

The values for the coefficients of the squared terms indicated that the scale factor for the stress-strain curve, the hysteretic unload factor and the young's modulus all displayed significant non-linear trends between the +1 and -1 values. These trends could be seen in surface plots of the significant two-way interactions calculated in the original fractional factorial experiment (Figure 57 and Figure 58); the plot of the effect of density (Figure 59) showed a very linear response as would be expected based on the coefficients.

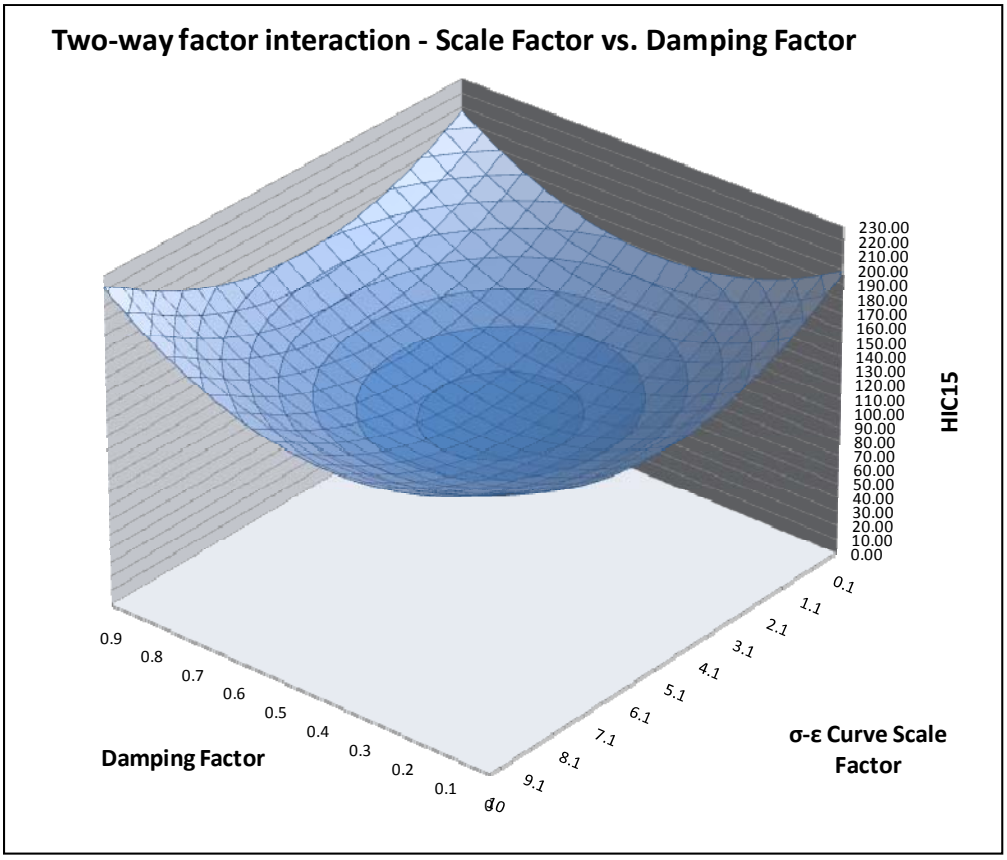

Figure 57: Surface plot of two-way interaction - Scale Factor vs. Damping Factor

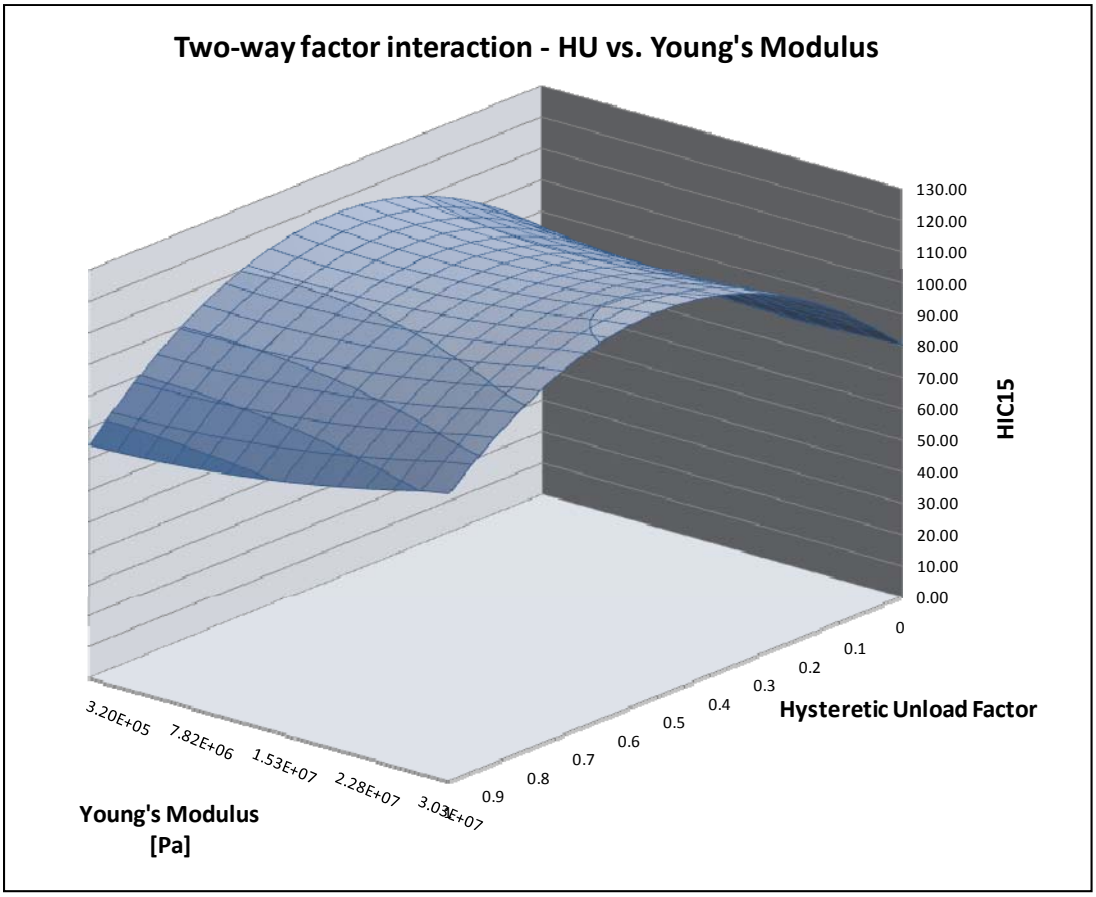

Figure 58: Surface plot of two-way interaction - Hysteretic Unload Factor vs. Young's Modulus

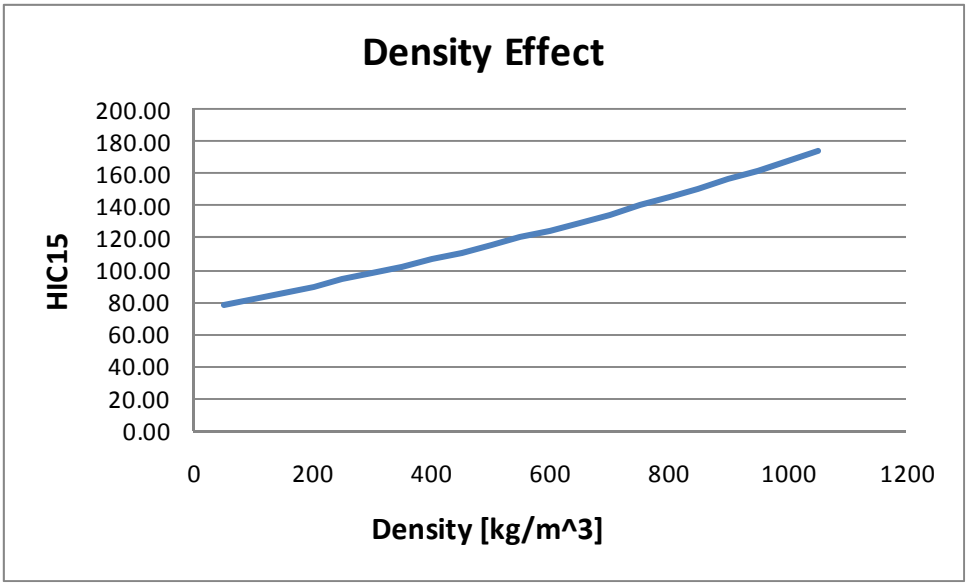

Figure 59: Plot of foam density effect

The best combination of parameters for the foam material model were found to be Density = 40 kg/m^3; Stress-Strain Curve Scale Factor = 5 (Figure 60); Hysteretic Unload Factor = 1; Damping Factor = 0.4; and Young's Modulus = 3.2E5 Pa. The plots for all of the trials as well as the optimal properties (dashed line) are shown below (Figure 61).

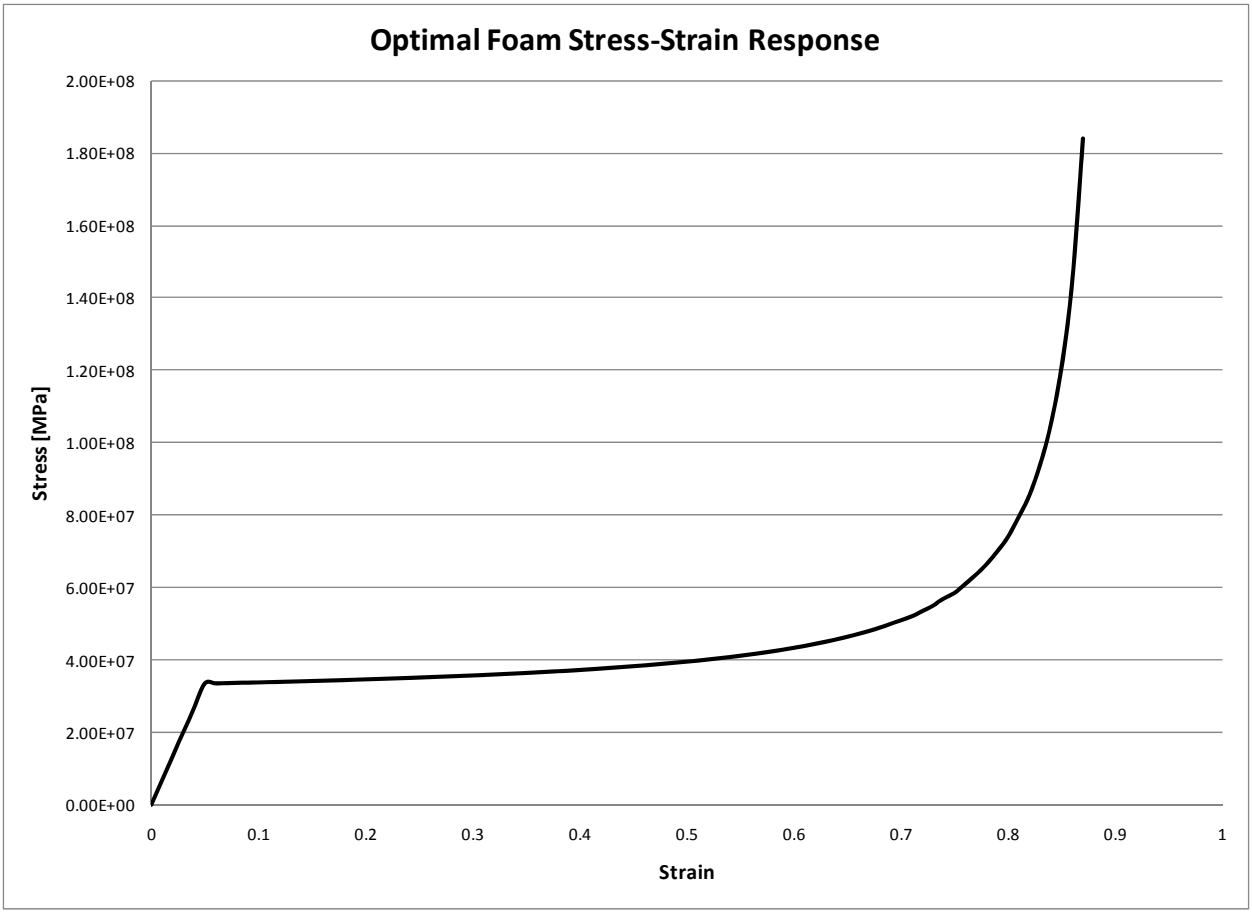

Figure 60: Optimized material stress-strain curve

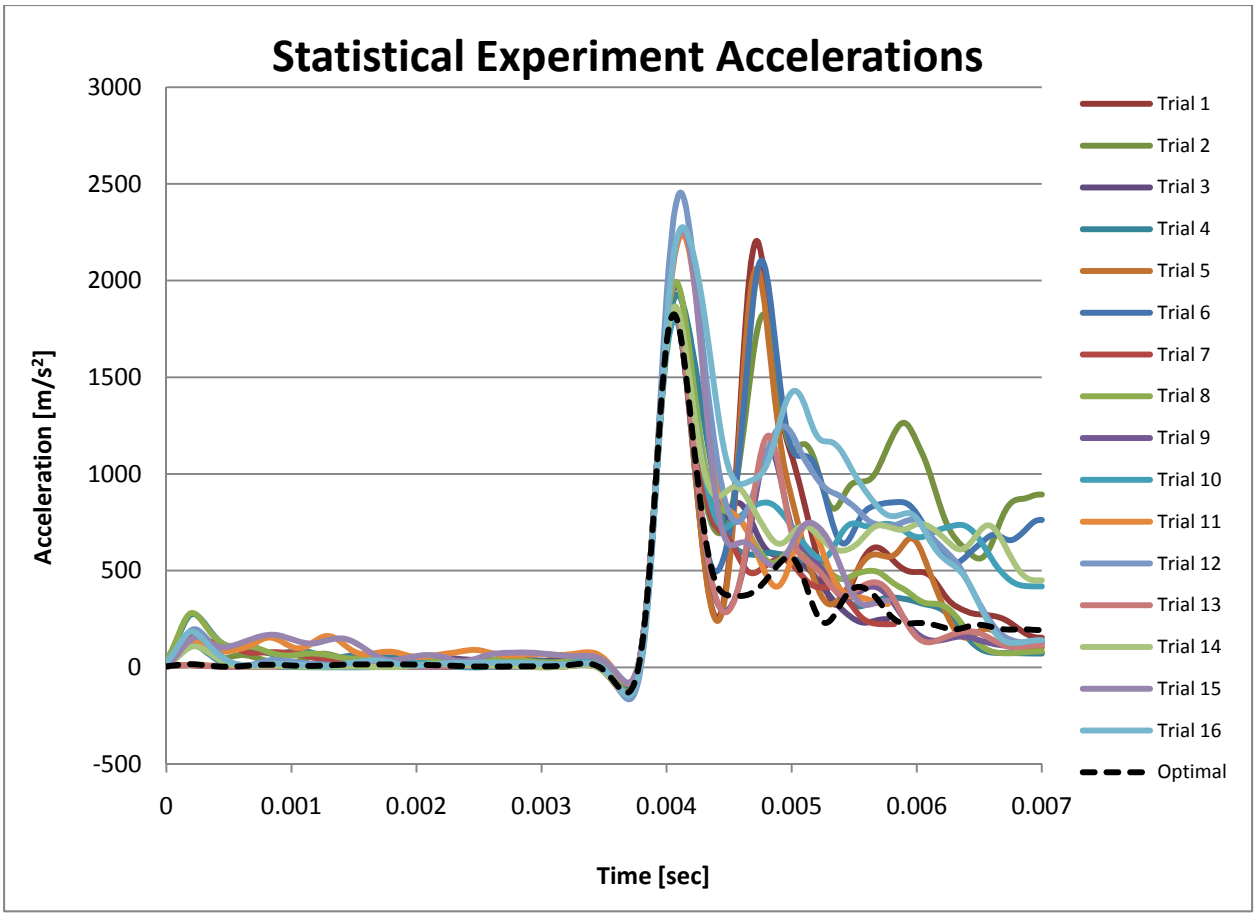

Figure 61: Statistical Experiment Trial Acceleration Plots

The optimal configuration resulted in a HIC_{15} value of 95.92, which was lower than all other values found during the study. It also reduced the peak acceleration seen by the CG of the head from 2986 m/s^2 to 1822 m/s^2, a reduction of 39%.

8.3 FOAM SELECTION

The stress-strain behavior of the optimal foam suggests that a metallic foam would be suitable for this application due to the high plateau stress. Typical polymeric foams have plateau stresses around 1 MPa, while metallic foams can have plateau stresses as high as 100 MPa [84].

The density and Young's Modulus of some common polymeric and metallic foams were compared against the optimal configuration (Figure 62). Based on only these two parameters, the best foam was found to be either a closed cell polypropylene or low density polyethylene foam (LD45).

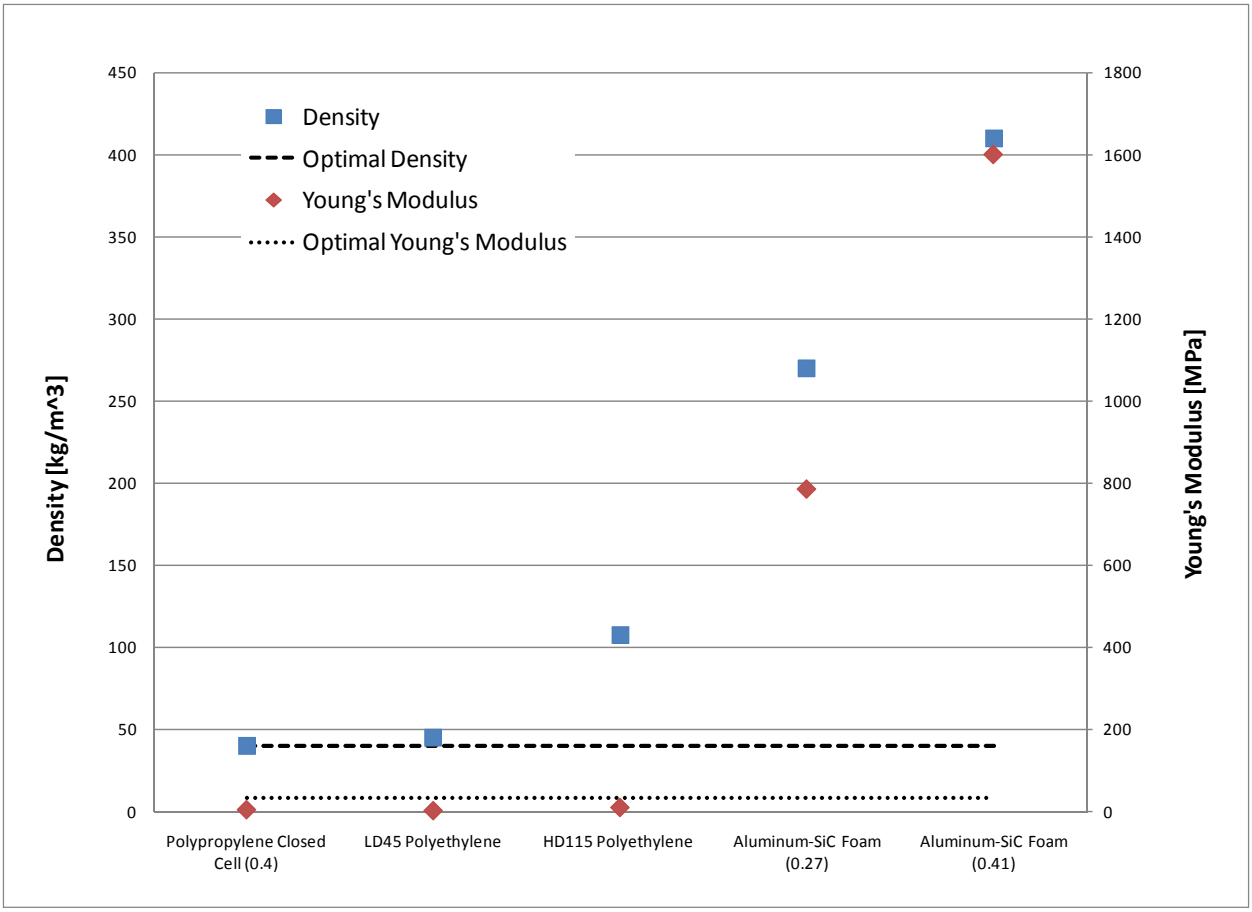

Figure 62: Density and Young's Modulus comparison for some common foams

The coefficients calculated in the factorial study indicated that the properties of the stress-strain curve (as modified by the scale factor) had a large effect on the model response in terms of the HIC_{15} value. By comparing key components of the stress-strain curves for the various materials

against the optimal values (Figure 63) it was found that the values for the aluminum foams were much closer to the optimal stress-strain curve values than those of the polymeric foams.

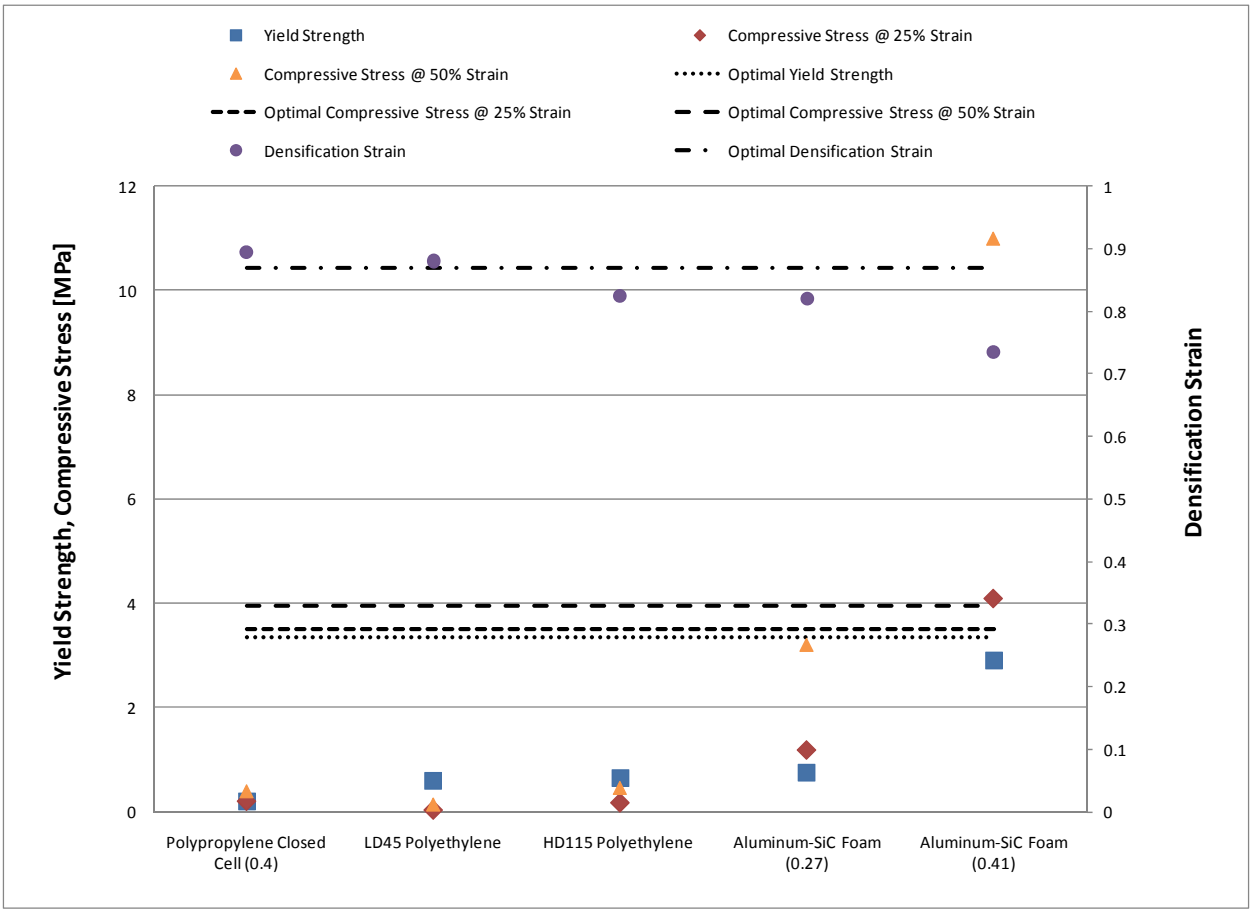

Figure 63: Stress-Strain Curve Component Comparison

The stress-strain response for the Al-SiC foam (0.41) with a density of 400 kg/m^3 was a very close match to the optimized foam response. One challenge with choosing a metallic foam is that the constitutive model used in the study was for a crushable foam which had almost complete recovery after loading. A metallic foam will densify and show almost no recovery due to plastic deformation. The benefit of the aluminum foams is that they are essentially strain rate independent [105] meaning they do not exhibit the viscoelastic behavior normally associated

with crushable foams. This non-viscoelastic behavior allowed for the use of a quasi-static stress-strain curve to be used to describe the material behavior for all strain rates.

The stress-strain curve for the aluminum foam was input into the foam material model [16] used in the statistical study for three standoff distances (3, 3.5 and 4 meters) with a 1.5m HOB. In all three cases, the foam reduced the accelerations and the HIC_{15} values seen at the CG of the head (Figure 64 and Figure 65) when compared to the unprotected head under the same conditions.

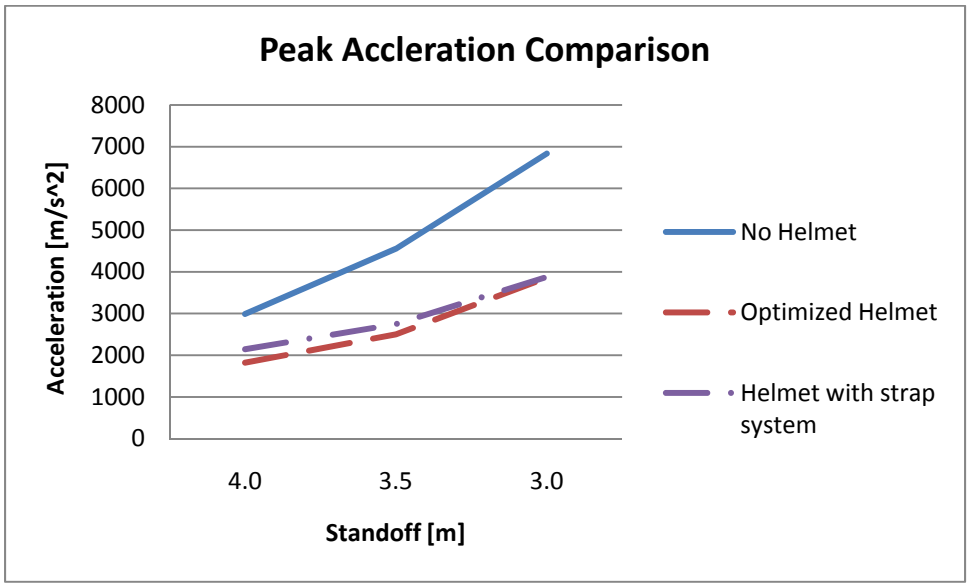

Figure 64: Accelerations of sagittal model CG with and without a helmet

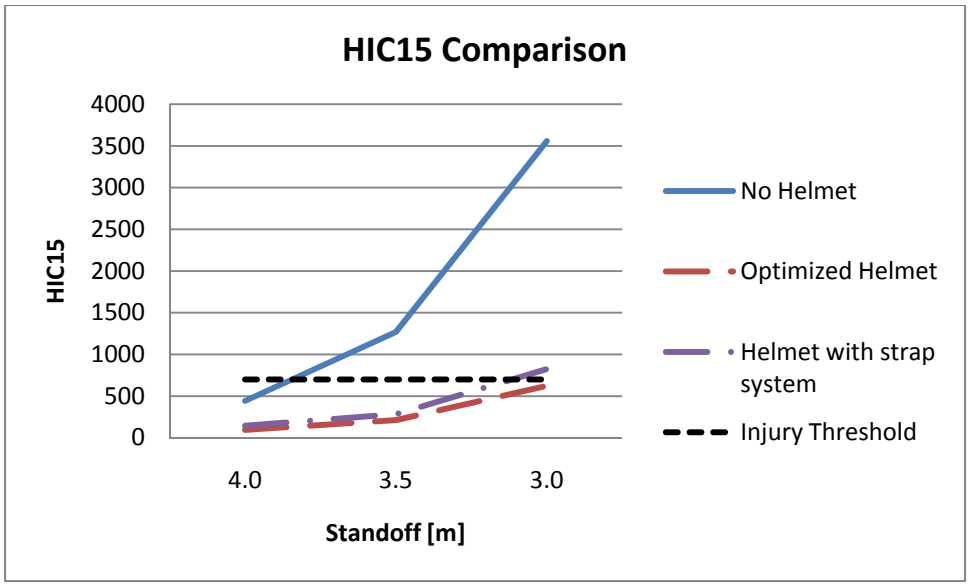

Figure 65: HIC_{15} values of sagittal model with and without a helmet

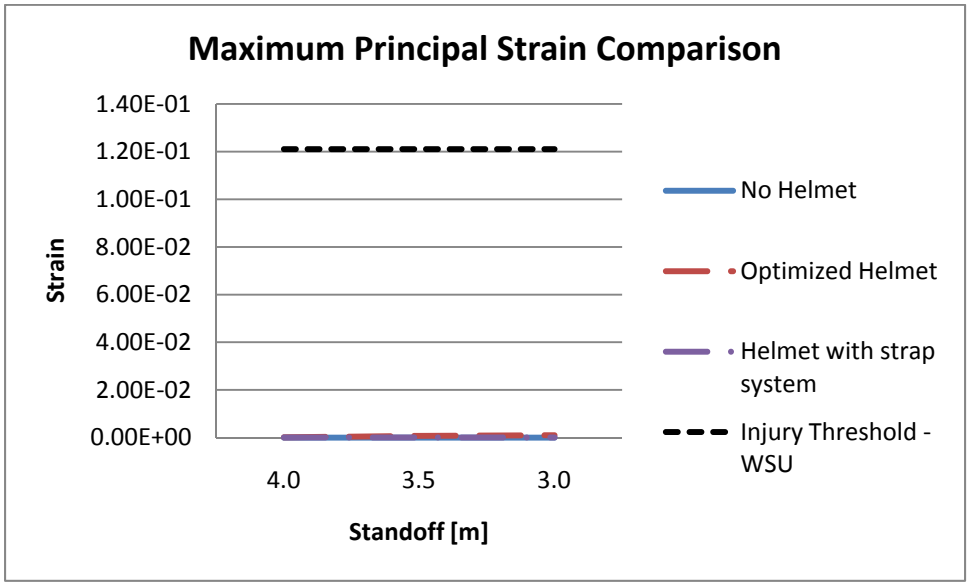

Figure 66: Maximum Principal Strain of sagittal model with and without a helmet

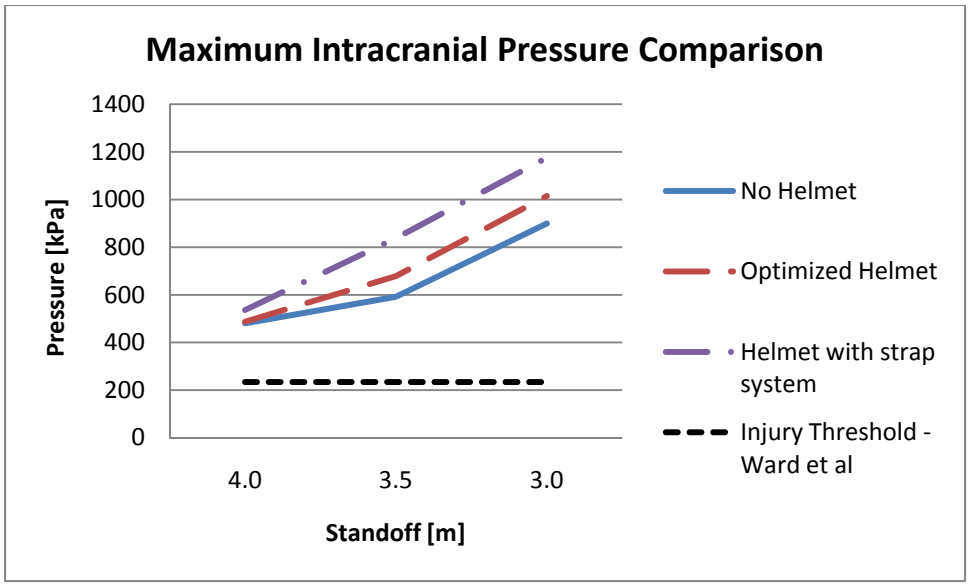

Figure 67: Maximum Intracranial Pressure of sagittal model with and without a helmet

The maximum principal strain (Figure 66) had values that were orders of magnitude lower than the proposed threshold of 0.121 postulated by Wayne State University. This is to be expected since the brain material is a nearly incompressible substance. The maximum intracranial pressure (Figure 67) increased for all three standoff distances when the helmet was added and all of the responses were above the injury threshold of 234.4 kPa, proposed by Ward et al. The pressure increase with the addition of the helmet is a result of the model geometry (Figure 68). For the optimized helmet, the small gap between the helmet and the head that is not covered by foam has a pressure that was double the magnitude of the pressure outside the gap (Figure 69).

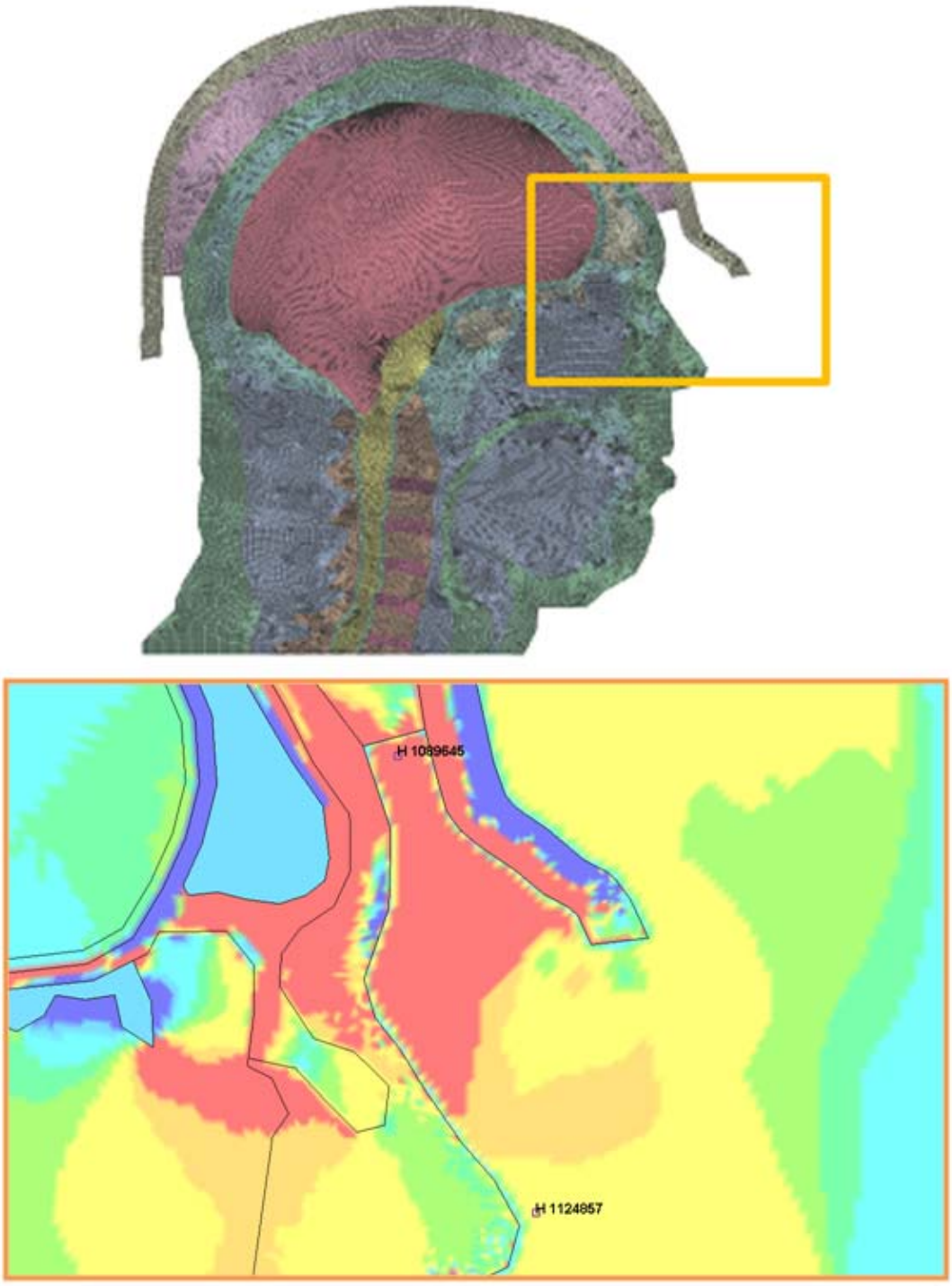

Figure 68: Pressure field in free field and beneath the lip of the helmet

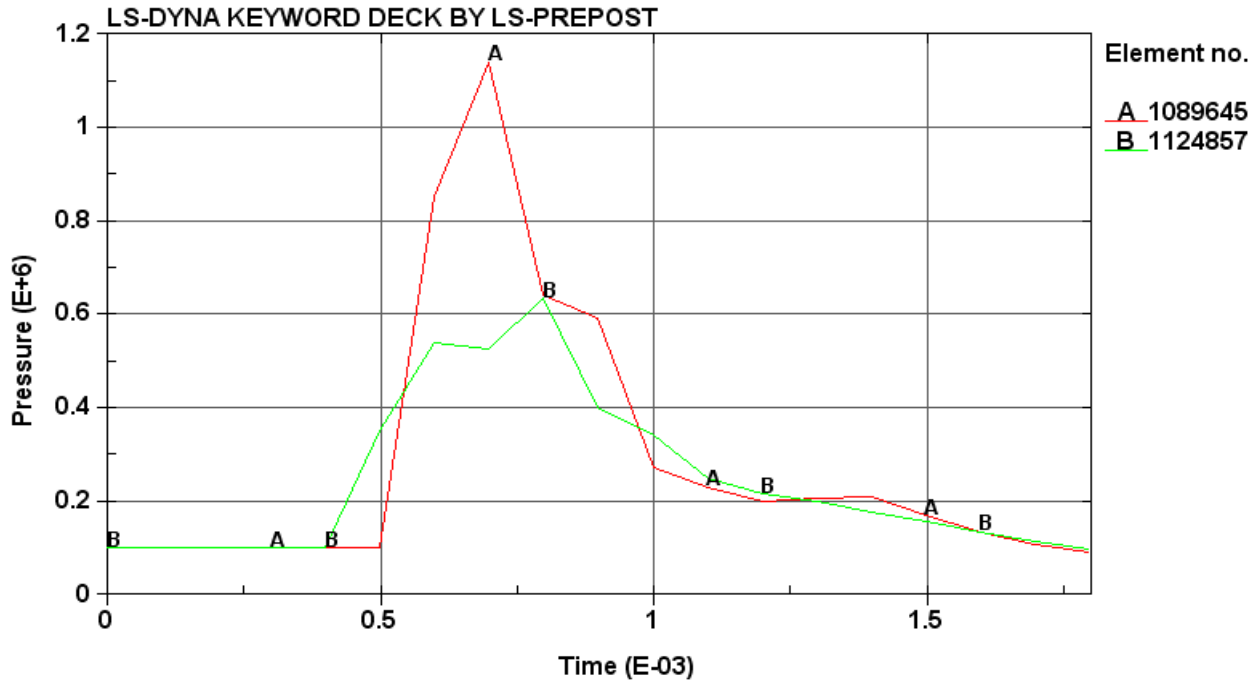

Figure 69: Plots of pressure in free field and beneath the lip of the helmet

The strap system helmet contains an air gap between the head and helmet. This air gap was shown previously (Figure 53) [102] to enhance the pressure field beneath which results in higher loading than the unprotected head.

9 DISCUSSION

The numerical methods of applying blast loading were invesitigated by comparing peak pressure, arrival time, and positive phase duration with the experimental data. The enhanced version of CONWEP which includes ground reflection and mach stem formation should be used whenever possible since it resulted in the closest response to the experimental data; however, the enhanced version was only valid for a scaled range of 0.136 ft/lbm$^{1/3}$ to 100 ft/lbm$^{1/3}$. For detonations with scaled HOBs below the lower bound of this range a mirrored blast approach, in which a second charge was placed at an equal distance below the ground, was found to be in good agreement with the experimentally measured blast data in terms of arrival time and positive phase duration; however, this approach did result in higher peak pressure values. Both the non-enhanced version of CONWEP and the hemispherical surface burst implementation were not in good agreement with the experimental data. In general, the non-enhanced version of CONWEP should only be used for charges with a scaled HOB greater than 100 ft/lbm$^{1/3}$ and the hemispherical burst formulation only for charges located on the ground.

By validating the kinematic response of a simple numerical model of the human body, the GEBOD, a parametric study was able to be conducted to determine the effect which charge location has on the HIC_{15}. The effects of standoff distance, lateral distance and HOB on the head response were investigated and the predicted accelerations and injury criteria values suggested that head injury may occur when the body is in close proximity to the blast origin (less than approximately 35 charge radii) but also can occur for larger standoff distances of approximately 40-60 charge radii (5 to 7 meters in the case of 12.5 kg of TNT) due to the formation of the mach stem. It should be noted that the influence of the mach stem will depend on the charge size,

HOB, standoff and height of subject. Increasing the lateral distance while keeping the total standoff between the explosive and head constant did not have a significant effect on the head response to the blast loading.

To further investigate the response to blast loading, a sagittal model of the head at the mid-sagittal plane was created that was representative of a 50^{th} percentile male. This model, which can be used to measure tissue-level response to blast loading, provides a more robust base with which to test the protective aspects of a helmet in a blast environment than the non-deformable GEBOD. While more computationally expensive, this model allows for comparison to newer proposed injury metrics that involve the brain and cranial cavity. Since the sagittal head model is not a full three-dimensional model of the head, it does not capture the wave interaction due to the overall shape of the head.

The optimal properties of a foam to for use in a helmet liner to reduce head injury, via minimizing the HIC_{15}, were found to corresponded quite closely to those of aluminum foam. When a layer of this foam was added to the helmet on the sagittal head model, the HIC_{15} value was reduced from 442.6 to 95.9 for a 5 kg C4 charge with a HOB of 1.5 meters and standoff distance of 4 meters. For standoff distances of 3 and 3.5 meters, there was also a reduction in the HIC_{15} and peak acceleration. This indicates that the addition of a layer of foam to the helmet liner could reduce head injury in a blast loading scenario. A couple polymeric foams compared quite closely for some of the optimal properties from the study, but more experiments are required to characterize their response to high strain-rate loading before they can be numerically implemented in this model.

In contrast to the acceleration and HIC, the maximum intracranial pressure increased when the helmet was added to the head, and exceeded the injury threshold for all standoff distances considered. This increase can be attributed to the model geometry concentrating the pressure beneath the lip of the helmet. This would indicate that small changes in the helmet geometry may have a large contribution to the pressure experienced by the head during blast loading. The maximum principal strains were all very low as was expected for the brain material which is nearly incompressible.

10 CONCLUSIONS

An investigation of the methods of applying blast loading numerically concluded that the most accurate methods were the new enhanced CONWEP formulation which incorporates ground interaction and reflection and a mirrored charge setup. The mirrored charge setup should be used when the scaled HOB is below the lower bound of the scaled range for the enhanced blast formulation. The non-enhanced version of CONWEP is generally under-predictive and should only be used when the scaled HOB is above the upper bound for the enhanced version.

A simplified model of the human body, the GEBOD, was validated against existing experimental data based on kinematics, using a Hybrid III dummy subjected to blast loading scenarios. The results of this study show that blast loading to the head can result in significant accelerations, and potentially injury to the head. The method of blast loading used for this study does have some limitations. The loading conditions included ground reflections and mach stem formation, but other complexities that can be encountered in real blast environments were not captured, such as wave interaction with surrounding objects. It should be noted that the head kinematics for this study were only considered for short term blast wave loading. The long term loading from a possible subsequent fall and impact with the ground was not considered, but has been found to be significant in some cases.

A study performed on the effects of standoff distance and HOB demonstrated that the formation of the mach stem has a large influence on the head response. The formation of the mach stem is highly dependant on the sclaed HOB, making a change in the charge size or HOB more influential than a change in height of the subject. For example, a 15 kg charge of TNT with a

HOB of 1.6 meters will have a mach stem height of 1.99 meters (6’ 6”) at a standoff of 7 meters. Raising the HOB by 20 cm (7.8”) to 1.8 meters will decrease the height of the mach stem by 30.5 cm (1’) to 1.685 meters (5’ 6”).

A sagittal head model was developed to represent a 50^{th} percentile male and provide a method of measuring tissue level response to blast loading. While the injury mechanisms associated with TBI due to the interaction of the blast pressure wave with the head are not well understood and there is currently no validated injury criterion, the numerical model was useful in determining how blast loading can affect the kinematic response of the head. In the future, should a criterion be developed, this model can be used to predict injury at the tissue level and help to develop methods of injury prevention.

The addition of a layer of aluminum foam to the helmet liner could potentially reduce the risk of primary blast injury to the head. The preliminary studies performed showed that it will provide a significant reduction in the acceleration experienced by the brain under blast loading. A concern with using aluminum foam is that it is quite sharp and an additional layer would be required to prevent it from cutting the head when loaded. Some polymeric foams have similar densities, and Young’s Moduli as the optimal configuration, but their stress-strain response is an order of magnitude lower. While not optimal, polymeric foams could be investigated for use in mitigating blast injury; however, the lower plateau stress will not provide as much protection as the metallic foams. In addition, polymeric foams are rate dependant, so more data would be required to implement them numerically and achieve appropriate response for high strain rate loading.

The optimization of the foam for use in a helmet liner was performed using the HIC_{15} as opposed to a more tissue specific injury criterion. Even though they have not been validated for short term blast loading, the maximum principal strain and maximum intracranial pressure were also compared for the protected and unprotected sagittal head model. All blast loading scenarios resulted in maximum intracranial pressure values for both the protected and unprotected head that were above the injury thresholds postulated by Ward et al due to the model geometry. The small gap at the front lip of the helmet resulted in a doubling of the pressure and consequently an increase in the intracranial pressure over the unprotected head. These results suggested that the geometry of the helmet plays a very significant role in the pressures experienced by the head. The maximum principal strain values were all very low and below the proposed injury threshold for both the protected and unprotected head.

This study has shown that blast loading to the head can result in significant accelerations which could result in injury. By using common materials in the existing form of head protection, the potential for injury as a result of acceleration can be reduced. Furthermore, the detailed two-dimensional sagittal head model can be used to predict the response to blast loading at the tissue level.

11 RECOMMENDATIONS

All studies up to this point have been using the criteria developed for the automotive industry to predict injury for crash scenarios. The duration and peak accelerations imparted by the crash loading are very different from those in a blast loading scenario. A fundamental understanding of the mechanisms by which traumatic brain injury occurs in a blast loading scenario need to be determined so that a validated injury criterion can be developed for short duration blast loading.

Further refinement of the sagittal head model should be done to yield a more accurate response while keeping in mind the computational expense. The material models used for the various tissues and organs should be improved by implementing more complex constitutive material models or adding more response data at various strain rates to more accurately capture the viscoelastic response that would be exhibited under the high strain rate blast loading.

The helmet investigation presented was a very preliminary and brief look into the protective properties of a single material. The statistical methods used in the study included quadratic aspects of the main effects but should be expanded to account for possible cubic effects in the response. In addition, experimental studies should be done to better define the response of the aluminum foam under blast loading. The constitutive model used in the variable analysis study may not accurately model the response of a metallic foam. For the simplest handling of plastic deformation of the foam, the MAT_CRUSHABLE_FOAM constitutive model may be a better option [103]. In addition, polymeric foams should be investigated as a substitute for the

aluminum foam. Response data at various strain rates would be required to better define the response and characterize the protective properties.

A full three dimensional model of the helmet should be developed that incorporates the foam padding and along with a three dimensional model of the head, be placed in an Eulerian fluid to examine the three dimensional wave effects in the fluid around the helmet and the stress wave propagation through the helmet. Physical testing of the foam liner should also be conducted to provide better validation data for the numerical model.

REFERENCES

1. **Bowen, I.G., et al.** *Estimate of man's tolerance to the direcct effects of air blast.* Department of Defense, Defense Atomic Support Agency. Washington, D.C. : s.n., 1968. Technical Progress Report no. DASA-2113.

2. **Bhattacharjee, Yudhijit.** Shell Shock Revisited: Solving the Puzzle of Blast Trauma. *Science Magazine.* January 25, 2008, Vol. 318, pp. 406-408.

3. *Blast Related Traumatic Brain Injury: What Is Known?* **Taber, K, Warden, D and Hurley, R.** Spring 2006, J Neuropsychiatry Clin Neurosci 18:2, pp. 141-145.

4. **U.S. Department of Defense.** *Casualty Summary by Reason.* DOD Personnel and Military Casualty Statistics, Center, Defense Manpower Data. available at [http://siadapp.dmdc.osd.mil/personnel/CASUALTY/gwot_reason.pdf].

5. **iCasualties.org.** Operation Enduring Freedom | Fatalities by Nationality. *iCasualties.org: Operation Enduring Freedom.* [Online] 2009. http://www.icasualties.org/OEF/Nationality.aspx?hndQry=Canada.

6. *Blast-Induced Neurotrauma: Surrogate Use, Loading Mechanisms, and Cellular Responses.* **Desmoulin, Geoffrey T. and Dionne, Jean-Philippe.** s.l. : Lippincott Williams & Wilkins, Inc., 2009, The Journal of Trauma: Injury, Infection, and Critical Care, Vol. 67(5), pp. 1113-1122.

7. *Suicide Bombing Attacks: Update and Modifications to the Protocol.* **Almogy, Gidon, et al.** 3, s.l. : Lippincott Williams & Wilkins, 2004, Ann Surg, Vol. 239, pp. 295-303.

8. *Terrorist Bombings: Lessons Learned from Belfast to Beirut.* **Frykberg, E. and Tepas, J.** 5, November 1988, Annals of Surgery, Vol. 208.

9. *Head Injury Criteria in Automotive Crash Testing.* **Newman, J.** s.l. : Society of Automotive Engineers, Inc, 1980. Proceedings, 24th Stapp Car Crash Conference. SAE Paper No. 801317.

10. *New Blast Weapons.* **Dearden, P.** 2001, J R Army Med Corps, Vol. 147, pp. 80-86.

11. **Hetherington, J. G. and Smith, P. D.** *Blast and Ballistic Loading of Structures.* Burlington, MA : Butterworth-Heinemann, 1994.

12. **Bulson, P.S.** *Explosive Loading of Engineering Structures.* New York : Taylor & Francis, 1997.

13. **Mazarak, Oleg, Martins, Claude and Amanatides, John.** Animating Exploding Objects. s.l. : York University Department of Computer Science.

14. *Toxicology of Blast Overpressure.* **Elsayed, Nabil M.** 1997, Toxicology 121, pp. 1-15.

15. **Richmond, Donald R., et al.** *Biologic Response to Complex Blast Waves.* Los Alamos, New Mexico : Los Alamos National Laboratory, 1985.

16. **LSTC.** *LS-DYNA Keyword User's Manual (Version 971).* Livermore, California : LSTC, 2007.

17. *Airblast Short Course.* **Needham, Charles.** Arlington, VA : s.n., August 2009. Advanced Technologies and New Frontiers in Injury Biomechanics with Military and Aerospace Applications.

18. **Meyers, Marc A.** *Dynamic Behavior of Materials.* s.l. : Wiley-IEEE, 1994.

19. *Blast Waves and How They Interact with Structures.* **Cullis, I.G.** 2001, J R Army Med. Corps, pp. 147: 16-26.

20. *Critical Distance for Blast-Resistant Design.* **Dharaneepathy, M.V., Keshava Rao, M.N. and Santhakumar, A.R.** 4, s.l. : Elsevier Science Ltd., 1995, Computers & Structures, Vol. 54, pp. 587-595. 0045-7949/95.

21. **Kingery, C. and Bulmarsh, G.** *Airblast Parameters from TNT Spherical Air Burst and Hemispherical Surface Burst [ARBRL-TR-02555].* Aberdeen Proving Ground, MD. : U.S. Army Ballistic Research Laboratory, 1984.

22. *Simulation of Blast-Head Interactions to Study Traumatic Brain Injury.* **Chafi, M., Karami, G. and Ziejewski, M.** Seattle, Washington, USA : ASME, 2007. Proceedings of IMECE2007. Vol. 2, pp. 211-220. IMECE2007-41629.

23. **LSTC.** *Enhanced Blast Loading in LS-DYNA.* [LS-Dyna Theory Manual] Livermore, CA : Livermore Software Technology Corporation, 2008.

24. *NUMERICAL MODELING OF BLAST LOADING TO THE HEAD.* **Cronin, Duane S. and Salisbury, Christopher, Binette, Jean-Sebastien, Williams, Kevin, Makris, Aris.** Brussels, Belgium : s.n., 2008. Personal Armour Systems Symposium. pp. 84-93.

25. **Hallquist, John O.** *LS-DYNA Theory Manual.* Livermore, CA : Livermore Software Technology Corperation, 2006. ISBN 0-9778540-0-0.

26. **Greer, A.** Numerical Modeling for the Prediction of Primary Blast Injury to the Lung. *MASc Thesis.* Waterloo, ON : s.n., 2006.

27. **ASME.** *Guide for Verification and Validation in Computational Solid Mechanics.* New York : The American Society of Mechanical Engineers, 2006. ASME V&V 10-2006.

28. **Roache, Patrick J.** *Verification and Validation in Computational Science and Engineering.* Albuquerque, New Mexico : hermosa publishers, 1998. ISBN 0-913478-08-3.

29. **Nahum, Alan M. and Melvin, John.** *Accidental Injury: Biomechanics and Prevention.* s.l. : Springer, 2001.

30. *Experimental and Numerical Modelling of a Mannequin for the Assessment of Blast Incapacitation and Lethality Under Blast Loading.* **Bouamoul, A., Williams, K. and Levesque, H.** Tarragona, Spain : s.n., 2007. 23rd International Symposium on Ballistics. pp. 1189-1196.

31. **Manseau, J., et al.** *Response of the Hybrid III Dummy Subjected to Free-Field Blasts - Focussing on Tertiary Blast Injuries.* s.l. : MABS, 2006.

32. **Cheng, H., Obergefell, L. and Rizer, A.** *Generator of Body (GEBOD) Manual.* Wright-Patterson Air Force Base, Ohio : Air Force Materiel Command, 1994.

33. **Williams, Kevin.** *Test Plan - MABIL Development Phase III.* Valcartier, Quebec, Canada : s.n., March 23, 2004.

34. **Moore, Keith L. and Dalley, Arthur F.** *Clinically Oriented Anatomy 4th Edition.* Baltimore : Lippincott Williams & Wilkins, 1999. ISBN 0-683-06141-0.

35. **McKinley, M. and O'Loughlin, V.** *Human Anatomy 2nd Edition.* New York, NY, USA : McGraw-Hill, 2008. ISBN 978-0-07-296549-0.

36. **Bridwell, K.** Anatomical Planes of the Body. *Spineuniverse.* [Online] Spineuniverse, August 7, 2007. [Cited: May 7, 2009.] http://www.spineuniverse.com/displayarticle.php/article1023.html.

37. **Cowles, Robert A.** MedlinePlus Medical Encyclopedia: Skull. *MedlinePlus.* [Online] U.S. National Library of Medicine and the National Institutes of Health, July 25, 2007. [Cited: May 5, 2009.] http://www.nlm.nih.gov/medlineplus/ency/images/ency/fullsize/9057.jpg.

38. *Mechanical Properties of Cranial Bone.* **McElhaney, J., et al.** Great Britain : Pergamon Press, 1970, Journal of Biomechanics, Vol. 3, pp. 495-511.

39. *Identification of Skull Behavior Laws Starting from Bending Tests.* **Delille, C., et al.** s.l. : Elsevier, 2003, Mécanique & Industries, Vol. 4, pp. 119-123.

40. **Hole, John W. Jr.** *Human Anatomy and Physiology.* 3rd Edition. Dubuque : Wm. C. Brown Publishers, 1984. ISBN 0-697-04790-3.

41. **Epilepsy Foundation of America.** Brain Functions and Makeup. *Epilepsy Foundation.* [Online] http://www.epilepsyfoundation.org/about/science/functions.cfm.

42. **American Health Assistance Foundation.** Anatomy of the Brain. *Alzheimer's Disease Research.* [Online] American Health Assistance Foundation, January 6, 2009. [Cited: May 5, 2009.] http://www.ahaf.org/alzheimers/about/understanding/anatomy-of-the-brain.html.

43. *A micromechanical hyperelastic modeling of brain white matter under large deformation.* **Karami, G., et al.** s.l. : Elsevier, 2009, Journal of the Mechanical Behavior of Biomedical Materials, Vol. 2, pp. 243-254.

44. **Neurosurgical Associates.** Cranial Anatomy. *Neurosurgical Associates, PSC.* [Online] Neurosurgical Associates, 2000. [Cited: May 5, 2009.] http://www.kyneurosurgeons.com/medtronic/anatomyandcauses/CranialAnatomy.htm.

45. *Hydrodynamic Modeling of Cerebrospinal Fluid Motion Within the Spinal Cavity.* **Loth, F., Yardimci, M. and Alperin, N.** s.l. : ASME, February 2001, Journal of Biomechanical Engineering, Vol. 123, pp. 71-79.

46. *A Correction for Primary Blast Injury Criteria.* **Gruss, Eyal.** 2006, The Journal of TRAUMA Injury, Infection, and Critical Care, pp. 1284 - 1289.

47. *Explosions and Blast Injuries.* **Wightman, John M. and Gladish, Sheri L.** June 2001, Annals of Emergency Medicine, pp. 664-678.

48. **Stuhmiller, J, Phillips, Y and Richmond, D.** The Physics and Mechanisms of Primary Blast Injury. [book auth.] R. F., Zajtchuk R. Bellamy. *Conventional Warfare: Ballistic, Blast and Burn Injuries.* Washington DC : Office of the Surgeon General of the US Army, 1991.

49. **Clemedson, Carl-Johan.** *Blast Injury.* Sundbyberg, Sweden : Research Institute of National Defence, 1956.

50. *The pathology of primary blast overpressure injury.* **Mayorga, M.A.** 121, s.l. : Elsevier, 1997, Toxicology, pp. 17-28.

51. **Popp, J and Deshaies, E.** *A Guide to the Primary Care of Neurological Disorders.* s.l. : Thieme Medical Publishers, 2007.

52. *Diffuse Axonal Injury and Degredation in Mechanical Characteristics of Brain White Matter.* **Abolfathi, N., et al.** Marco Island, Florida, USA : ASME, 2008. Proceedings of the ASME 2008 Summer Bioengineering Conference. SBC2008-192251.

53. *Finite Element Analysis of Brain Contusion: an Indirect Impact study.* **Huang, H., et al.** 2000, Medical & Biological Engineering & Computing, Vol. 38, pp. 253-259.

54. **Stuhmiller, J.H.** *Blast Injury - Translating Research into Operational Medicine.* Fort Detrick, Maryland : United States Army Medical Research and Material Command, 2008. BI-QP-JHS-CH10.

55. **SAE.** *J885: Human Tolerance to Impact Conditions as Related to Motor Vehicle Design.* s.l. : SAE International, 2003.

56. *Is Head Injury Caused by Linear or Angular Acceleration?* **King, A., et al.** Lisbon, Portugal : IRCOBI, 2003. IRCOBI Conference.

57. *The Head Injury Criterion (HIC) functional.* **Hutchinson, J., Kaiser, M. and Lankarani, H.** s.l. : Elsevier Science Inc., 1998, Applied Mathematics and Computation, Vol. 96. PII: S0096-3003(97) 10106-0.

58. *Modeling Head Motion During Explosive Events to Assess Brain Injury Severity in a Battlefield Environment.* **Connolly, Thomas J. and Clutter, Keith J.** Seattle, Washington, USA : ASME, 2007. ASME International Mechanical Engineering Congress and Exposition. Vol. 10A, pp. 571-580. IMECE2007-43391.

59. *Shell Shock and Mild Traumatic Brain Injury: A Historical Review.* **Jones, E., Fear, N. and Wessely, S.** 11, 2007, American Journal of Psychiatry, Vol. 164, pp. 1641-1645.

60. *The viscous criterion - bases and applications of an injury severity index for soft tissues.* **Lau, I. and Viano, D.** San Diego, CA : SAE International, 1986. Proceedings of the 30th Stapp Car Crash Conference. pp. 672-691.

61. *Classification of Traumatic Brain Injury for Targeted Therapies.* **Saatman, K., et al.** s.l. : Mary Ann Liebert, Inc., July 2008, Journal of Neruotrauma, Vol. 25, pp. 719-738.

62. **Makris, A., et al.** *Reduction of Blast Induced Head Acceleration in the Field of Anti-Personnel Mine Clearance.* s.l. : Med-Eng Systems Inc., 2000.

63. **Dionne, J.P., Nerenberg, J. and Makris, A.** *Reduction of Blast-Induced Concussive Injury Potential and Correlation with Predicted Blast Impulse.* Ottawa, Ontario, Canada : Med-Eng Systems Inc., 2002.

64. *A Proposed New Biomechanical Head Injury Assessment.* **Newman, James A, Shewchenko, Nicholas and Welbourne, Eric.** s.l. : The Stapp Association, 2000. 44th Stapp Car Crash Conference. Stapp Paper Number OOS-80.

65. *A Proposed Tolerance Criterion for Diffuse Axonal Injury in Man.* **Marguiles, S. and Thibault, L.** 8, Great Britain : Pergamon Press Ltd., 1992, Journal of Biomechanics, Vol. 25, pp. 917-923. 0021-9290/92.

66. *Intracranial Pressure - A Brain Injury Criterion.* **Ward, C., Chan, M. and Nahum, A.** 1980. Proceedings, 24th Stapp Car Crash Conference. SAE Paper No. 801304.

67. *Simulation of Blast-Head Interactions to Study Traumatic Brain Injury.* **Sotudeh Chafi, M., Karami, G. and Ziejewski, M.** Seattle, Washington, USA : ASME, 2007. ASME International Engineering Congress and Exposition. Vol. 2, pp. 211-220. IMECE2007-41629.

68. *A Proposed Injury Threshold for Mild Traumatic Brain Injury.* **Zhang, L., Yang, K. and King, A.** s.l. : ASME, April 2004, Journal of Biomechanical Engineering, Vol. 126, pp. 226-236.

69. *Separating brain motion into rigid body displacement and deformation under low-severity impacts.* **Zou, Hong, Schmiedeler, James P. and Hardy, Warren N.** 40, s.l. : Elsevier Ltd., 2007, Journal of Biomechanics, pp. 1183-1191.

70. *Mathematical Modeling of Cerebral Concussion: Correlations of Regional Brain Strain with Clinical Symptoms.* **Zhang, Liying, Yang, King and Gennarelli, Thomas A.** Bern, Switzerland : International Research Council on the Biomechanics of Injury, 2008. International IRCOBI Conference on the Biomechanics of Injury. pp. 123-132.

71. **McHenry, Brian G.** *Head Injury Criterion and the ATB.* s.l. : McHenry Software, Inc., 2004.

72. *Modeling of the Human Head Under Impact Conditions: A Parametric Study.* **Claessens, M., Sauren, F. and Wismans, J.** s.l. : Society of Automotive Engineers, 1997. Proceedings, 41st Stapp Car Crash Conference. SAE Paper No. 973338.

73. *Mechanisms of Axonal Injury: An Experimental and Numerical Study of a Sheep Model of Head Impact.* **Anderson, R., et al.** Sitges, Spain : IRCOBI, 1999. Proceedings of the International Research Council on the Biomechanics of Injury Conference. pp. 107-120.

74. **Mao, Haojie.** *Computational analysis of in vivo brain trauma.* Collection for Wayne State University. 2009. http://digitalcommons.wayne.edu/dissertations/AAI3365832 . Paper AAI3365832.

75. **Houff, Charles W. and Delaney, Joseph P.** *Historical Documentation of the Infantry Helmet Research and Development.* Aberdeen Proving Ground, Maryland : U.S. Army Human Engineering Laboratory, 1973. Technical Memorandum 4-73.

76. **Beyer, James C., Enos, William F. and Holmes, Robert H.** Chapter XI: Personnel Protective Armor. *U.S. Army Medical Department Office of Medical History.* [Online] June 18, 2009. [Cited: February 9, 2010.] http://history.amedd.army.mil/booksdocs/wwii/woundblstcs/chapter11.htm.

77. **Olive-Drab.com LLC.** PASGT Kevlar Helmet. *Olive-Drab.* [Online] 1998-2010. [Cited: February 12, 2010.] http://www.olive-drab.com/od_soldiers_gear_kevlar_helmet.php.

78. *Thermoplastic Matrix Combat Helmet with Graphite-Epoxy Skin.* **Folgar, Franciso, et al.** Tarragona, Spain : s.n., 2007. 23rd International Symposium on Ballistics. pp. 883-892.

79. **Ivins, Brian J., et al.** *How Satisfied are Soldiers with their Ballistic Helmets? A Comparison of Soldiers' Opinions about the Advanced Combat Helmet and the Personal Armor System for*

Ground Troops. Fort Rucker, AL : U.S. Army Aeromedical Research Laboratory, 2008. USAARL Report No. 2008-14.

80. **Thom, Chris.** Soft Materials Under Air Blast Loading and their Effect on Primary Blast Injury. *MASc Thesis.* Waterloo, ON : s.n., 2009.

81. **Yang, H. H.** *Kevlar Aramid Fiber.* Baffins Lane, Chichester : John Wiley & Sons Ltd., 1993. ISBN 0 471 93765 7.

82. *Ballistic Impact of KEVLAR Helmet: Experiment and Simulations.* **Tham, C. Y., Tan, V. B.C. and Lee, H. P.** 35, Singapore : Elsevier Ltd., 2008, International Journal of Impact Engineering, pp. 304-318.

83. *Ballistic Impact Response of Laminated Composite Panels.* **Gower, H. L., Cronin, D. S. and Plumtree, A.** 2007, Int J Impact Eng.

84. **Gibson, Lorna J. and Ashby, Michael F.** *Cellular Solids: Structure & Properties.* Toronto : Pergamon Press Canada Ltd., 1988. ISBN 0-08-035910-8.

85. *Deformation characteristics of metal foams.* **Banhart, J. and Baumeister, J.** 33, Bremen, Germany : Chapman & Hall, 1998, Journal of Materials Science, pp. 1431-1440.

86. **McEntire, Joseph B., Mason, Kevin T. and Austinhirst, Ruth A.** *Impact Protection Properties of Candidate Foam Inserts for the Personnel Armor System for Ground Troops (PASGT) Helmet System.* Aircrew Protection Devision, U.S. Army Aeromedical Research Laboratory. Fort Rucker, Alabama : s.n., 1996. USAARL Report No. 96-09.

87. **Reilly Foam Corperation.** Reilly Foam Corperation: Volara. *Reilly Foam Corperation.* [Online] 1998-2009. http://www.reillyfoam.com/volara.htm.

88. **Department of the Army.** *Explosives and Demolitions.* Washington D.C. : Headquarters Department of the Army, 1967. Field Manual 5-25.

89. **National Center for Health Statistics.** *Body Measurments.* Hyattsville, MD, United States of America : s.n., August 8, 2008.

90. **McConville, John T., Churchill, Thomas D., Kaleps, Ints, Clauser, Charles E., Cuzzi, Jaime.** *Anthropometric Relationships of Body and Body Segment Moments of Inertia.* Wright-Patterson Air Force Base, Ohio : Air Force Aerospace Medical Research Laboratory, 1980.

91. **First Technology Safety Systems.** FTSS Product Catalog | Products. *First Technology Innovative Solutions.* [Online] 2009. [Cited: February 24, 2009.] http://www.ftss.com/pcat/products.cfm?obr=NS&bm=1&pcat=h3-50m-2&class=1&x=500&y=1560.

92. **AGARD.** *Anthropomorphic Dummies for Crash and Escape System Testing.* Neuilly-Sur-Seine, France : Advisory Group for Aerospace Research & Development, 1996.

93. **U.S. National Library of Medicine.** AnatQuest Cut-Away Viewer. *AnatQuest Anatomic Images Online.* [Online] Lister Hill National Center for Biomedical Communications, August 23, 2004. http://anatquest.nlm.nih.gov/AnatQuest/AwtCsViewer/aq-cutaway.html.

94. *A stabilized nodally integrated tetrahedral.* **Puso, M. A. and Solberg, J.** 67, Livermore, CA : Wiley InterScience, 2006, Int. J. Numer. Meth. Engng, pp. 841-867.

95. **Clauser, Charles E. et al.** *Weight, Volume, and Center of Mass of Segments of the Human Body.* Wright-Patterson Air Force Base, Ohio : Air Force Systems Command, 1969. AD-710 622.

96. *Parametric Study of Effects on Brain-Skull Boundary Conditions and Brain Material Properties on Responses of Simplified Finite Element Brain Model under Angular Acceleration Impulse in Sagittal Plane.* **Wittek, Adam and Omori, Kiyoshi.** 4, 2003, JSME International Journal, Vol. 46, pp. 1388-1399.

97. *Coupling of Strasbourg University Head Model to THUMS Human Body FE Model: Validation and Application to Automotive Safety.* **Ipek, H., et al.** s.l. : University of Strasbourg.

98. *Application of finite element techniques to the study of cervical spine mechanics.* **Kleinberger, M.** San Antonio, TX : Society of Automotive Engineers, Inc., 1993. Proc 37th Stapp Car Crash Conf.

99. *A simplified approach to the simulation of rubber-like materials under dynamic loading.* **DuBois, PA.** May 2003. 4th European LS-DYNA Users Conference.

100. *High strain rate compressive properties of soft tissue.* **Van Sligtenhorst, C.R., Cronin, D.S. and Brodland, G.W.** s.l. : American Society of Mechanical Engineers, Bioengineering Division BED, 2003, Vol. 55.

101. *The Influence of Clothing on Human Intrathoracic Pressure During Air-Blast.* **Young, A., et al.** 1985, Aviat. Space Environ. Med., Vol. 56, pp. 49-53.

102. *Blast-Induced Pressure Fields Beneath a Military Helmet.* **Mott, David R., et al.** San Antonio, Texas : American Physical Society, 2008. 61st Annual Meeting of the APS Divison of Fluid Dynamics. Vol. 53.

103. *Selecting Material Models for the Simulation of Foams in LS-DYNA.* **Croop, Brian and Lobo, Hubert.** DatapointLabs, NY USA : DYNAmore GmbH, 2009. 7th European LS-DYNA Conference.

104. **Box, George E.P., Hunter, William G. and Hunter, J. Stuart.** *Statistics for Experimenters: An Introduction to Design, Data Analysis, and Model Building.* New York, USA : John Wiley & Sons, 1978. ISBN 0-471-09315-7.

105. **Yu, C.J., et al.** *Feasibility Study on Deformation Energy Absorption of Metal Foams at High Strain Rates.* Newark, DE : Fraunhofer USA Resource Center, 1999. ARO 38790.1-MS.